# Measurement of the Polarization of the Cosmic Microwave Background with the Bicep2 and *Keck Array* Telescopes

Thesis by

Grant Paul Teply

In Partial Fulfillment of the Requirements

for the Degree of

Doctor of Philosophy

California Institute of Technology

Pasadena, California

2015

(Defended May 8, 2015)

# Abstract

Precision polarimetry of the cosmic microwave background (CMB) has become a mainstay of observational cosmology. The $\Lambda$CDM model predicts a polarization of the CMB at the level of a few $\mu$K, with a characteristic $E$-mode pattern. On small angular scales, a $B$-mode pattern arises from the gravitational lensing of $E$-mode power by the large scale structure of the universe. Inflationary gravitational waves (IGW) may be a source of $B$-mode power on large angular scales, and their relative contribution to primordial fluctuations is parameterized by a tensor-to-scalar ratio $r$. BICEP2 and *Keck Array* are a pair of CMB polarimeters at the South Pole designed and built for optimal sensitivity to the primordial $B$-mode peak around multipole $\ell \sim 100$. The BICEP2/*Keck Array* program intends to achieve a sensitivity to $r \geq 0.02$. Auxiliary science goals include the study of gravitational lensing of $E$-mode into $B$-mode signal at medium angular scales and a high precision survey of Galactic polarization. These goals require low noise and tight control of systematics. We describe the design and calibration of the instrument. We also describe the analysis of the first three years of science data. BICEP2 observes a significant $B$-mode signal at 150 GHz in excess of the level predicted by the lensed-$\Lambda$CDM model, and *Keck Array* confirms the excess signal at $> 5\sigma$. We combine the maps from the two experiments to produce 150 GHz $Q$ and $U$ maps which have a depth of 57 nK deg (3.4 $\mu$K arcmin) over an effective area of 400 deg$^2$ for an equivalent survey weight of 248000 $\mu\mathrm{K}^{-2}$. We also show preliminary *Keck Array* 95 GHz maps. A joint analysis with the *Planck* collaboration reveals that much of BICEP2/*Keck Array*'s observed 150 GHz signal at low $\ell$ is more likely a Galactic dust foreground than a measurement of $r$. Marginalizing over dust and $r$, lensing $B$-modes are detected at $7.0\sigma$ significance.

# BICEP2/*Keck Array* collaboration

**California Institute of Technology** R. W. Aikin, J. J. Bock, J. A. Brevik, S. R. Golwala, V. V. Hristov, H. Hui, S. Kefeli, M. Lueker, P. Mason, Z. K. Staniszewski, G. P. Teply

**Cardiff University** P. A. R. Ade, R. V. Sudiwala

**CEA Grenoble** L. Duband

**Harvard-Smithsonian Center for Astrophysics** K. D. Alexander, D. Barkats, C. A. Bischoff, I. Buder, V. Buza, J. Connors, C. Dvorkin, K. S. Karkare, J. M. Kovac, S. Richter, C. L. Wong

**Jet Propulsion Laboratory** J. A. Bonetti, B. P. Crill, C. D. Dowell, S. R. Hildebrandt, K. G. Megerian, H. T. Nguyen, R. O'Brient, A. D. Turner, A. C. Weber, P. Wilson

**National Institute of Standards and Technology** G. C. Hilton, C. D. Reintsema

**Stanford University** Z. Ahmed, K. D. Irwin, S. A. Kernasovskiy, C. L. Kuo, R. W. Ogburn IV, K. L. Thompson, J. E. Tolan, K. W. Yoon

**University of British Columbia** M. Amiri, M. Halpern, M. Hasselfield

**University of California, San Diego** J. P. Kaufman, B. G. Keating

**University of Chicago** E. M. Leitch, C. D. Sheehy, A. G. Vieregg

**University of Illinois at Urbana–Champaign** J. P. Filippini

**University of Minnesota** E. Bullock, S. Fliescher, C. Pryke, R. Schwarz, J. Willmert

**University of Toronto** S. J. Benton, C. B. Netterfield

# Contents

# List of Figures

# List of Tables

# Chapter 1

# Introduction

Bicep2 and *Keck Array* are telescopes studying the cosmic microwave background (CMB) with the specific goal of testing cosmic inflation. The Bicep2/*Keck Array* Collaborations have released a series of papers including the Bicep2 primary results (BK–I) [9], instrument description (BK–II) [7], systematics (BK–III) [8], beams (BK–IV) [13], *Keck Array* primary results (BK–V) [12], description of the detector technology shared with Spider (Detectors Paper) [11], and a joint analysis with *Planck* (BKP) [10].

This thesis is a survey of the Bicep2/*Keck Array* results and includes many details beyond the main publications. I review the Bicep2/*Keck Array* instrument and design, calibrations, and analysis methods, including several details beyond what is included in the main papers. I call special attention to the Ph.D theses of the Bicep2/*Keck Array* graduate students before me: R. W. Aikin [2], J. A. Brevik [15], J. P. Kaufman [40], S. A. Kernasovskiy [43], C. D. Sheehy [80], J. E. Tolan [87], and C. L. Wong [91]. Anyone interested in the Bicep2/*Keck Array* results should consult their theses, for the results and their theses are inseparable.

I begin with a brief overview of the state of cosmology and the evidence for cosmic inflation. I include some introductory material that was prepared by me for BK–V [12]. This chapter is by no means exhaustive of the history or theoretical foundations of CMB cosmology. A recent, broad review of the cosmology from the CMB anisotropy has been written by M. Bucher [16] and is accessible at the graduate student level. Other helpful resources include *The Review of Particle Physics*[1] [54], many authoritative papers by the *Planck* collaboration[2], any of several popular textbooks, and references therein.

---

[1] `http://pdg.lbl.gov`

[2] `http://www.cosmos.esa.int/web/planck/publications`

## 1.1 Cosmic inflation

Precision measurement of the universe's continued expansion and large scale structure provide a rich picture of cosmology out to the farthest reaches of the cosmic distance ladder. The CMB, discovered by A. A. Penzias and R. W. Wilson in 1964, is an extragalactic black body of temperature 2.725 K, nearly uniform across the sky [56, 27, 62]. The slight anisotropy of the CMB acts as a standard ruler that traces primordial fluctuations. The acoustic peaks of its angular power spectrum signify the relative contributions of dark energy, dark matter, baryonic matter, and radiation in the primordial plasma. Observations of the acoustic peaks as well as other cosmological data sets generally support the ΛCDM model, a universe dominated by a cosmological constant and cold dark matter.

As the universe expands in the hot Big Bang, it undergoes radiation-dominated, matter-dominated, and dark energy-dominated epochs, in that order. For a radiation-dominated or matter-dominated universe, the comoving Hubble distance is always increasing. Distant, causally disconnected regions will gradually enter the horizon and come into causal contact, and once in contact will remain in contact. The features in the CMB angular power spectrum represent constructive and destructive interference of acoustic waves propagating through the primordial plasma. The peaks and troughs of the spectrum are resolved because the acoustic modes are in phase. The phase coherence persists even on scales larger than the horizon size at recombination. The coherence is most striking when accounting for the polarization of the CMB [82, 24]. Such uniformity seems to violate causality and is known as the horizon problem.

Cosmic inflation is a theory that attempts to explain the primordial fluctuations by proposing a period of ultra-rapid expansion of the primordial universe. According to inflationary theory, something like dark energy known as the inflaton dominates the expansion before the hot Big Bang's radiation-dominated epoch but decays away. Although this scenario may seem contrived, it turns out to be very easy to find an effective quantum field theory with this property because any scalar field in a suitably large and flat potential could act as the inflaton. The literature abounds with inflationary models, and many of them are referenced and discussed in, for example, the "Encyclopædia Inflationaris" [49] and the paper *Planck* 2015 XX [65]. Cosmic inflation makes specific predictions about the primordial fluctuations to resolve the horizon problem.

First, the primordial fluctuations themselves should arise from quantum mechanics. It is the rapid expansion of the universe that stretches these fluctuations out to superhorizon scales. The expansion is much faster than the evolution of any particular mode, so the phases of all the modes become close to zero. Thus at the end of inflation all of the modes begin evolving in phase with an initial phase of zero. Modes that begin with zero phase are the adiabatic modes, whereas modes that begin with 90° phase are the isocurvature modes. The locations of the peaks in the temperature angular power spectrum confirm that the modes are adiabatic [65]. Since the fluctuations are quantum, cosmic inflation predicts that the scalar fluctuations be very nearly Gaussian and nearly scale-invariant, although specific inflationary models predict slight deviations from these conditions. The CMB temperature anisotropy is highly Gaussian [64], and only a small deviation from scale invariance is observed [65].

Second, the scalar fluctuations that source the temperature anisotropy also source linear, parity-even polarization patterns on the sky, discussed further in Section 1.2. The parity-even polarization pattern is known as the $E$-mode polarization. The $E$-mode angular power spectrum has been measured as well and found to have a series of peaks consistent with the temperature measurements, discussed in Section 1.3. On scales larger than the horizon size, the temperature and $E$-mode patterns are anti-correlated. Such a degree of coherence is difficult to reconcile by any causal mechanism without inflation [82, 24].

Third, there may be tensor fluctuations, i.e., inflationary gravitational waves (IGW). The IGW can source $E$-mode polarization and an additional, parity-odd polarization pattern in the CMB known as the $B$-mode polarization. The $B$-mode angular power spectrum has a characteristic peak at degree angular scales. The tensor-to-scalar power ratio $r$ gives the energy scale of inflation, which depends on the inflationary model.

## 1.2 CMB polarization

Soon after the discovery of the CMB, M. J. Rees realized that anisotropic Thomson scattering in the primordial plasma can polarize the CMB [76]. Any confluence of waves introducing a local quadrupole anisotropy around an electron will cause the scattered light to be different along the two axes, i.e., polarized.

The polarization pattern across the sky, $E$-mode or $B$-mode, depends on the symmetries of the primordial fluctuations and can be used to distinguish scalar from tensor fluctuations. The importance of the symmetries and the $E$-mode/$B$-mode basis was fully appreciated in 1996 by M. Kamionkowski, A. Kosowsky, A. Stebbins, U. Seljak, and M. Zaldarriaga [78, 37, 79, 93, 38]. The transformation from Stokes $Q$ and $U$ to $E$ and $B$ is detailed in Section 3.4. Here we give only a brief intuition for the symmetries.

Primordial scalar fluctuations are of even parity. One way to understand this is to observe that a single mode is a longitudinal wave consisting of a stack of alternating overdense and underdense planes, which are rotationally invariant about the direction of propagation. In terms of spherical harmonics $Y_{\ell m}(\theta, \phi)$, the local quadrupole anisotropies are $m = 0$. In linear perturbation theory, the sum of all of the even-parity Fourier modes is also of even parity. Therefore, primordial scalar fluctuations induce $E$-mode patterns only.

Primordial tensor fluctuations are transverse, traceless perturbations of the metric. These possess an extra degree of freedom through the + and × polarization states of the gravitational waves, which translate to the $m = \pm 2$ quadrupoles. Because of this extra degree of freedom, primordial tensor fluctuations can produce a mixture of $E$-mode and $B$-mode patterns.

## 1.3 Observational status

Precision polarimetry of the CMB has become a mainstay of observational cosmology. The ΛCDM model predicts a polarization of the CMB at the level of a few $\mu$K, with a characteristic $E$-mode pattern. The $EE$ power spectrum has been detected over a wide range of angular scales by many experiments, including DASI [44], CAPMAP [3, 19], CBI [75, 81], BOOMERANG03 [52], WMAP [55, 4], MAXIPOL [92], QUAD [70, 71], BICEP1 [21, 6], QUIET [73, 72], POLARBEAR [66], BICEP2 [9], ACTPOL [53], SPTPOL [23], *Keck Array* [12], and *Planck*. These measurements have been in broad agreement with theoretical expectations and other cosmological data sets. Improved $EE$ power spectrum data are important because they may eventually constrain the ΛCDM model parameters better than cosmic variance limited CMB temperature data [77, 28].

Of greater interest is the $B$-mode component of the polarization pattern. Though the $EE$ power spectrum is higher, the $BB$ power spectrum is more sensitive to new physics because the linear density perturbations at the surface of last scattering, which are the main source of $TT$ and $EE$ power, cannot generate $B$-mode power. On small angular scales, $BB$ power instead arises from the gravitational lensing of $E$-mode power by the large scale structure of the universe [94]. The lensing $BB$ power thus cleanly traces the growth of structure, complementary to other methods, providing information about possible extensions to ΛCDM such as neutrino mass or a nontrivial dark energy equation of state. Measurements by SPTPOL [32, 42], POLARBEAR [67, 68, 66], BICEP2 [9], ACTPOL [90], *Keck Array* [12], and *Planck* [63] have provided the first evidence of $BB$ power from gravitational lensing.

On large angular scales, lensing contributes only a small amount of $BB$ power. However, the IGW may be a source of $BB$ power on these scales [69, 79, 37, 78]. The initial detection by BICEP2 of $B$-mode power on degree angular scales in excess above the lensing expectation is especially exciting because it could be evidence of primordial gravitational waves and cosmic inflation [9]. The contribution of foregrounds to the observed BICEP2 signal is uncertain, and data from *Planck* have suggested that polarized dust in the BICEP2 field may be brighter than models had predicted [61]. Regardless, a confirmation of the BICEP2 signal, whether cosmological or Galactic in origin, is a top priority of observational cosmology today[25, 18].

*Keck Array* confirms the 150 GHz BICEP2 $B$-mode signal at $> 5\sigma$ [12]. A joint analysis with the *Planck* collaboration reveals that much of BICEP2/*Keck Array*'s observed 150 GHz signal at low $\ell$ is likely a Galactic dust foreground, whereas much of the observed signal at high $\ell$ is lensed CMB [10]. These results are discussed in Chapter 5.

# Chapter 2

# Instrument

In this chapter, I describe the BICEP2 and *Keck Array* instrument design. I also pedagogically describe many of the primary calibration and performance optimization methods.

Several subsystems and calibrations are further detailed in other Ph.D theses and conference proceedings. All of the other Ph.D theses are great resources and in many ways are more complete than what I offer here. Cryogenic considerations, especially with regard to the redesign for *Keck Array*, are presented in C. D. Sheehy's thesis [80]. The design of the *Keck Array* focal plane unit (FPU) is in J. E. Tolan's thesis [87]. Characterization and optimization of the bolometers, SQUIDs, and readout are in J. A. Brevik's thesis [15] for BICEP2 and S. A. Kernasovskiy's thesis [43] for *Keck Array.* Optics and beams are thoroughly described in R. W. Aikin's thesis [2] for BICEP2 and C. L. Wong's thesis [91] for *Keck Array.* The BICEP2 spectral response measurement is in J. P. Kaufman's thesis [40], and the *Keck Array* spectral response is in conference proceedings presented by K. S. Karkare [39]. Other useful information may be found in the Ph.D theses of A. R. Trangsrud [88] and R. S. Tucker [89], which focus on the development of closely related instrumentation for SPIDER.

Sections 2.1 and 2.2 are a general overview of the BICEP2/*Keck Array* instrument design and their South Pole observing site. Section 2.3 briefly lists the readout electronics and software. Section 2.4 describes the cryogenic systems of the telescopes. For the remainder of the chapter, Sections 2.5–2.16, I describe many of the details of the detectors and the campaign for measuring their properties as they were screened and installed in the field, including detector electrical and thermal properties, beam mapping, absolute pointing

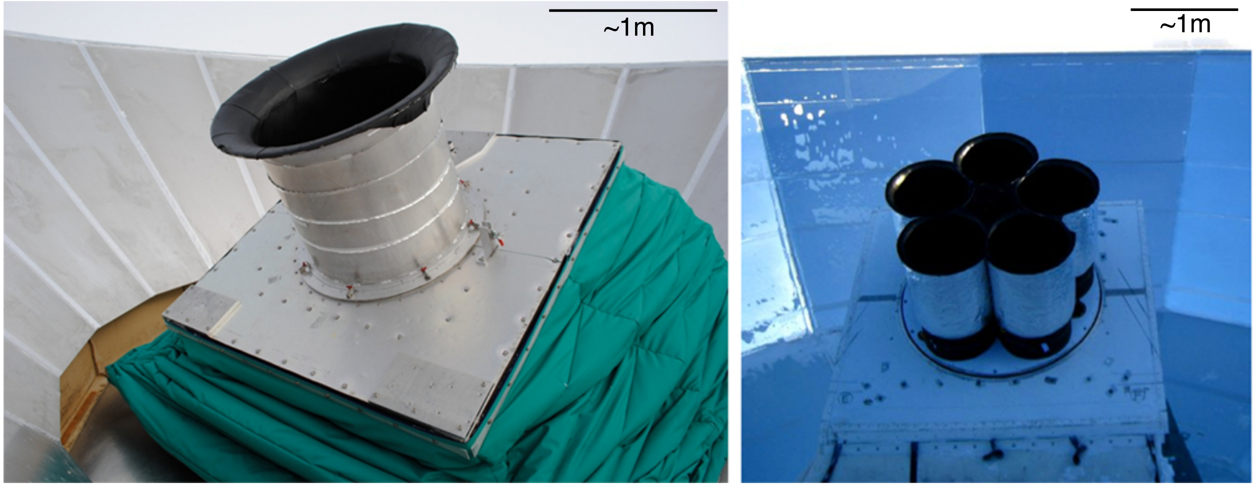

Figure 2.1: A picture of Bicep2 (left) and *Keck Array* (right) from the outside. The forebaffles and the reflective ground shield are visible.

and polarization angles, optical efficiency, spectral response, and more. The testing and deployment of the Bicep2/*Keck Array* detectors has occupied about half of my time in graduate school. Portions of the material below, including many of the figures, were prepared for the BK–II, BK–IV, BK–V, and the Detectors Paper.

## 2.1 General overview

Bicep2 and *Keck Array* are a pair of CMB polarimeters designed and built for optimal sensitivity to the primordial $B$-mode peak around multipole $\ell \sim 100$. The Bicep2/*Keck Array* program intends to achieve a sensitivity to $r \geq 0.02$. Auxiliary science goals include the study of gravitational lensing of $E$-mode into $B$-mode signal at medium angular scales and a high precision survey of galactic polarization. These goals require low noise and tight control of systematics. Bicep2 was installed at South Pole Station during the 2009-2010 austral summer and collected CMB data through 2012. *Keck Array*, which is essentially five copies of the Bicep2 instrument, was installed in a partial configuration during the 2010-2011 summer, upgraded to its full configuration the following summer, and is actively collecting CMB data as of 2015. The *Keck Array* receivers are labeled sequentially as rx0, rx1, rx2, rx3, and rx4. Related telescopes Bicep3 [1] and Spider [74] share much of their optical design and detector technology with the Bicep2/*Keck Array* program. Bicep3 began observing at the South Pole in 2015. Spider, which is a balloon-borne telescope, had its first flight in January 2015. Detailed discussion of Bicep3 and Spider is beyond the scope of this thesis.

The design of Bicep2/*Keck Array*, which are derivative of the Bicep1 instrument [85], is contrary to the usual design of most science quality telescopes in operation today, which boast very large mirrors and very fine angular resolution. Instead, the Bicep2/*Keck Array* strategy is to use small-aperture refractors for a deliberately coarse angular resolution, with beams as wide as $\sim 0.5^\circ$ FWHM at 150 GHz and $\sim 0.8^\circ$ FWHM at 95 GHz. Since an IGW $B$-mode signal would be expected to peak at degree angular scales, the required resolution need not be much finer than that. As a refractor, the optical chain can remain cylindrically symmetric, reducing any polarized systematic effects that could arise if there were an asymmetry. By keeping the telescope small, it is much easier to rotate the telescope around its boresight. The deck rotation modulates the antenna axis between Stokes $Q$ and $U$ and helps remove the effect of instrument polarization from the receivers.

Design changes between Bicep2 and *Keck Array* were kept to a minimum for rapid field-readiness and backward compatibility of the hardware. The focal plane units (FPUs) and lenses are all cross-compatible between Bicep2 and *Keck Array*. In fact, following the decommission of Bicep2 in 2012, the Bicep2 FPU was installed in one of the *Keck Array* receivers.

The modular design of *Keck Array* makes it possible to modify or repair any of the five receivers individually. Unlike Bicep1, each *Keck Array* receiver observes in only one spectral band. Anti-reflective coatings on optical elements within a receiver can thus be optimized for its particular band. Table 2.1 is a list of the actual frequency configuration of the telescopes. *Keck Array* data from 2011 are excluded from the analysis. The frequency configuration may change in the future based on relative sensitivities of the receivers, science goals, and availability of better replacement hardware.

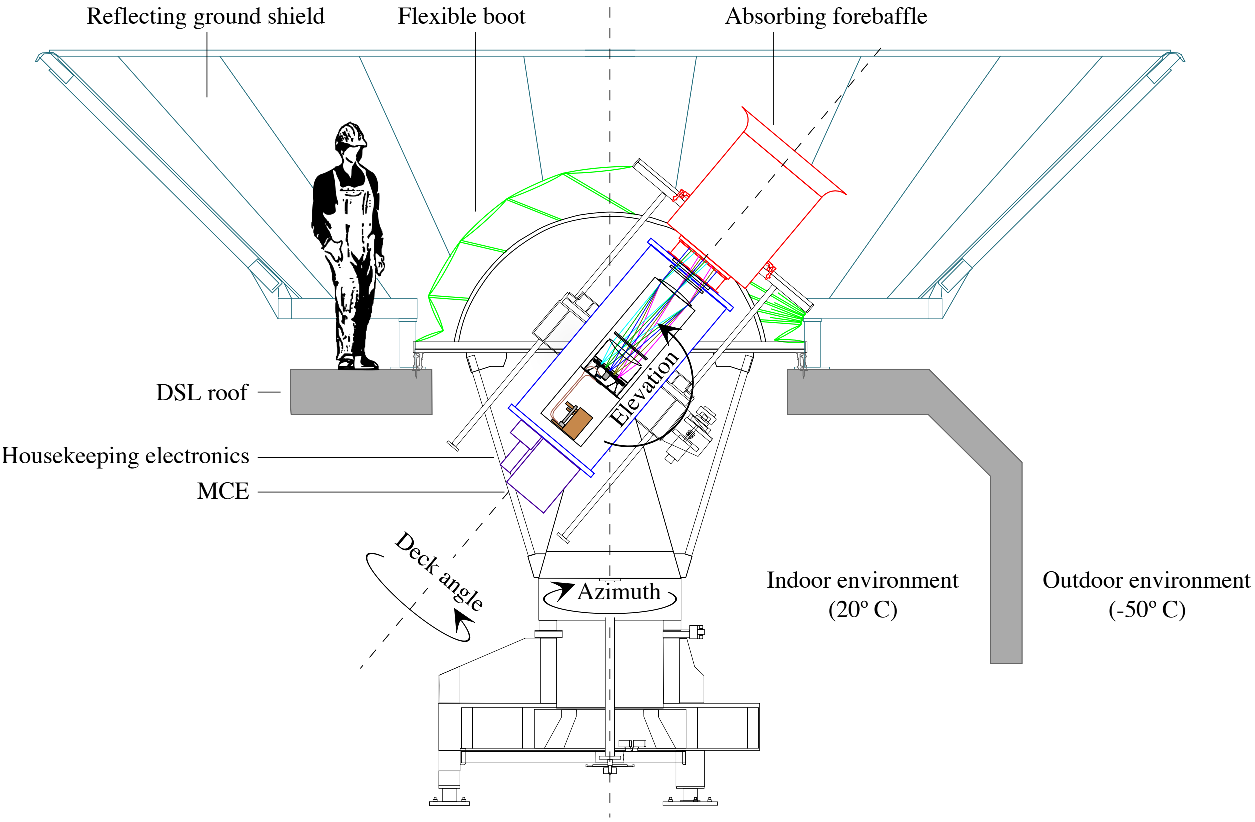

Figure 2.2: The Bicep2 telescope in the mount, looking out through the roof of the Dark Sector Laboratory (DSL) located 800 m from the geographic South Pole. The three-axis mount allows for motion in azimuth, elevation, and boresight rotation (also called "deck rotation"). An absorbing forebaffle and reflective ground screen prevent sidelobes from coupling to nearby objects on the ground. A flexible environmental seal or "boot" maintains a room temperature environment around the cryostat and mount. The telescope forms an insert within the liquid helium cryostat. The focal plane with polarization-sensitive TES bolometers is cooled to 270 mK by a $^4$He/$^3$He/$^3$He sorption refrigerator. The housekeeping electronics and Multi-Channel Electronics (MCE) attach to the lower bulkhead of the cryostat.

Table 2.1: The configuration and approximate observing band centers of the BICEP2/*Keck Array* receivers for each year to date.

| Receiver | | Configuration |
|---|---|---|
| BICEP2 2010-2012 | | 150 GHz, unchanged between observing seasons |
| *Keck Array* 2012 | rx0 | 150 GHz |
| | rx1 | 150 GHz |
| | rx2 | 150 GHz |
| | rx3 | 150 GHz |
| | rx4 | 150 GHz |
| *Keck Array* 2013 | rx0 | 150 GHz |
| | rx1 | 150 GHz, one of the four tiles replaced |
| | rx2 | 150 GHz |
| | rx3 | 150 GHz, FPU from BICEP2 installed |
| | rx4 | 150 GHz, new FPU installed |
| *Keck Array* 2014 | rx0 | 95 GHz |
| | rx1 | 150 GHz |
| | rx2 | 95 GHz |
| | rx3 | 150 GHz |
| | rx4 | 150 GHz |
| *Keck Array* 2015 | rx0 | 95 GHz |
| | rx1 | 230 GHz |
| | rx2 | 95 GHz |
| | rx3 | 230 GHz |
| | rx4 | 150 GHz |
| BICEP3 2015 | | 95 GHz, nine tiles |

## 2.2 Observing site

The South Pole is an excellent site for millimeter-wave observation from the ground, with a record of successful polarimetry experiments including Dasi, Bicep1, QUaD, and the South Pole Telescope. Situated on the Antarctic Plateau, it has exceptionally low precipitable water vapor [20], reducing atmospheric noise due to the absorption and emission of water near the 150 GHz observing band. The South Pole site also has very stable weather, especially during the dark winter months, so that the majority of the data are taken under clear-sky conditions of very low atmospheric $1/f$ noise and low loading [83]. The consistently low atmospheric loading is crucially important because the sensitivity of the experiment is limited by photon noise, so that low atmospheric emission is a key to high CMB mapping speed.

Finally, the Amundsen-Scott South Pole Station has hosted scientific research continuously since 1958. The station offers well-developed facilities with year-round staff and an established transportation infrastructure. Bicep1 and Bicep2 were housed in the Dark Sector Laboratory (DSL), which was built to support radio and millimeter-wave observatories in an area 1 km from the main station buildings and isolated from possible sources of electromagnetic interference. DSL currently houses Bicep3. *Keck Array* is housed in the Martin A. Pomerantz Observatory (MAPO) 200 m from DSL in the direction toward the main station. The *Keck Array* telescope mount was previously used for the Dasi [45] and QUaD [34] experiments. A new front end "drum" for the *Keck Array* cryostats was installed in 2010. The platform was leveled at that time to account for gradual shifts of the building on the snow relative to the horizon.

## 2.3 Readout and software

The primary detector data are read in a time-domain multiplexing scheme using SQUIDs (see Section 2.8). The power to the detectors and the SQUID readout is supplied by a Multi-Channel Electronics (MCE) crate[1] attached to the bottom of the cryostat. A custom housekeeping electronics backpack adjacent to the MCE connects to a BLASTbus crate [5], which reads out thermometers and powers resistive heaters. Bicep2 uses

---

[1] `http://e-mode.phas.ubc.ca/mcewiki/`

the first generation of BLASTbus, and *Keck Array* uses the second generation. The mount motion control and encoder readout is done by a Programmable Multi Axis Controller (PMAC)[2]. Bicep2 and *Keck Array* employ the Generic Control Program (GCP) [84] data acquisition and telescope control software, running on multiple Linux computers. GCP synchronizes and merges the data streams from the MCE, BLASTbus, and PMAC and records the data at 9 Hz (see Section 2.9).

## 2.4 Cryogenics

The Bicep2 cryostat was built by Redstone Aerospace[3]. The *Keck Array* cryostats were built by Atlas Technologies[4]. Inside each cryostat is a closed-cycle, three-stage ($^4$He/$^3$He/$^3$He) sorption refrigerator [26] that cools the FPU to approximately 270 mK. Other optical elements are held at cryogenic temperatures to minimize the thermal load on the FPUs.

The main difference between *Keck Array* and Bicep2 is the bulk refrigeration system. Bicep2 used a bath of liquid helium. *Keck Array* uses a set of Cryomech[5] PT-410 pulse tube refrigerators. Each *Keck Array* cryostat has its own pulse tube refrigerator aligned along the optical axis. The helium gas is pulsed at a common frequency of 1.2 Hz, and the pressure in each system is optimized to achieve the lowest base temperature. After optimization, the pulse tubes' copper mounting surfaces typically reach 40 K and 3 K with comparable performance in all five cryostats. These surfaces are thermally connected to the telescope insert by stacks of ultra high purity aluminum foil.

The FPU temperature is regulated in a manner similar to what was used in *Planck* [57]. A stainless steel block acts as a passive thermal filter between the sorption refrigerator and the FPU. A pair of temperature control modules are attached on opposite sides of the filter. The modules contain neutron transmutation doped (NTD) germanium thermometers and 1 M$\Omega$ resistive heaters, which GCP uses to stabilize the FPU temperature actively through a control loop. The NTD germanium thermometers are read out at AC by the BLASTbus using cryogenic JFETs similar to those used in the *Herschel*–SPIRE instrument [14].

---

[2] `http://www.deltatau.com/`

[3] `http://www.redstoneaerospace.com/`

[4] `http://www.atlasuhv.com/`

[5] `http://www.cryomech.com/`

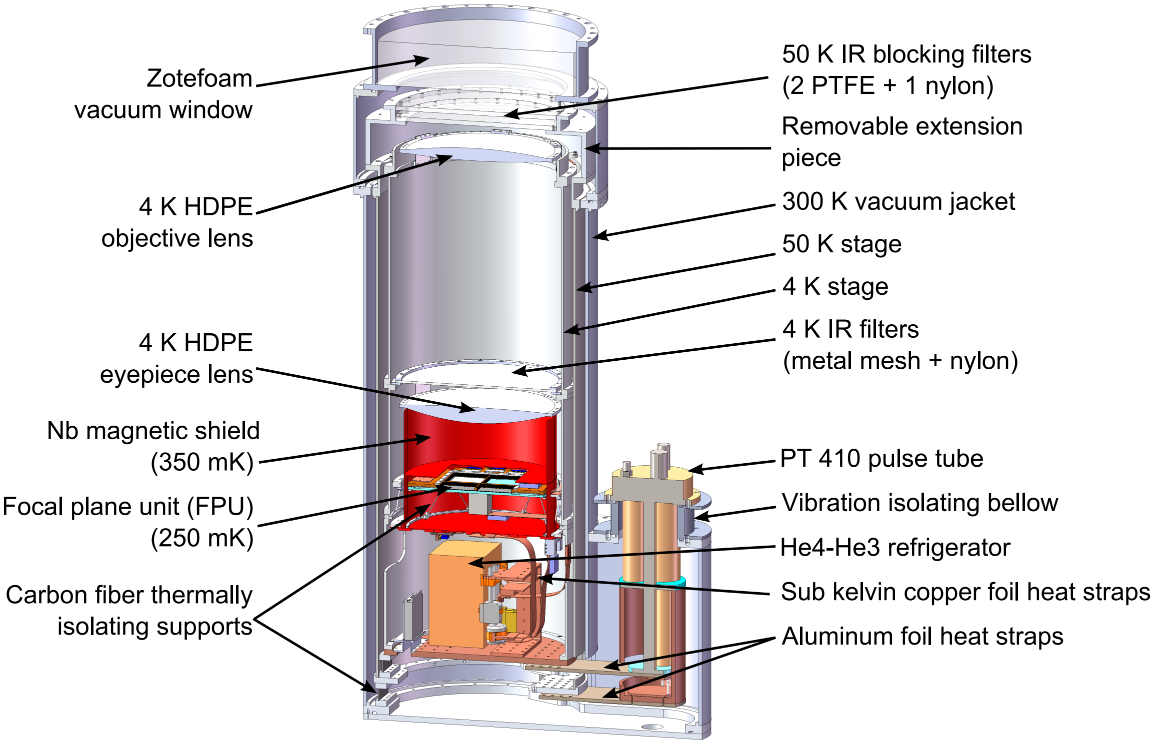

Figure 2.3: Individual receiver of *Keck Array*. Each receiver is cryogenic, with a pulse tube refrigerator cooling the optics to 4 K and a three-stage sorption refrigerator cooling the focal plane to 270 mK. *Keck Array* consists of five identical receivers on a single telescope mount at the South Pole.

## 2.5 Transition-edge sensors

BICEP2/*Keck Array*'s main innovation relevant for CMB polarimetry is the bolometric detector technology. Unlike previous generations of CMB experiments that used feedhorns to couple the detectors to the optics, BICEP2/*Keck Array* uses antenna-coupled transition-edge sensor (TES) arrays, printed photolithographically onto a silicon wafer. The device fabrication is done in the Microdevices Laboratory at JPL. The elimination of feedhorns allows the closer packing of and scalability to large numbers of detectors. Each focal plane unit prepared for BICEP2/*Keck Array* comfortably fits four of these ~ 7 x 7 cm detector tiles.

A pixel is a pair of devices measuring orthogonal polarization states. Each pixel contains two overlapping, orthogonally polarized arrays of slot antennas, one aligned vertically and one aligned horizontally. The pair of antennas couple the radiation onto a pair of TES bolometers. The length scale of the antennas themselves and band pass filters between the antennas and the bolometers (Figure 2.7) set the pass band of the pixel. The tiles at 95 GHz have 36 pixels each. The tiles at 150 and 230 GHz have 64 pixels each. It may be possible to increase the pixel density of the 230 GHz tiles in the future.

The TES is a voltage-biased resistor at its superconducting transition. It sits on an "island" of heat capacity $C$ weakly connected by thermal conductance $G$ across silicon nitride legs to a thermal bath, which is effectively the 270 mK bulk of the detector tile. Thermal contact between the tile and the copper frame is through clamping by the tile clips and a large number of gold wire bonds around the edge of the tile to the frame. The tile temperatures are monitored by NTD germanium thermometers epoxied directly to the tiles and read out in the same way as the temperature control modules (see section 2.4).

The rate that heat is added to the TES is optical power and electrical Joule power added minus the heat flow through the legs as

$$C\frac{dT}{dt} = P_{\mathrm{opt}} + P_{\mathrm{J}} - P_{\mathrm{bath}} \tag{2.1}$$

The operating temperature stays stable by electrothermal feedback. As $P_{\mathrm{opt}}$ increases, the temperature briefly rises. If the TES is on transition, then the rising temperature causes the TES resistance to increase by a large amount. For a voltage-biased TES, the increase in resistance gives a decrease in $P_{\mathrm{J}}$, which returns

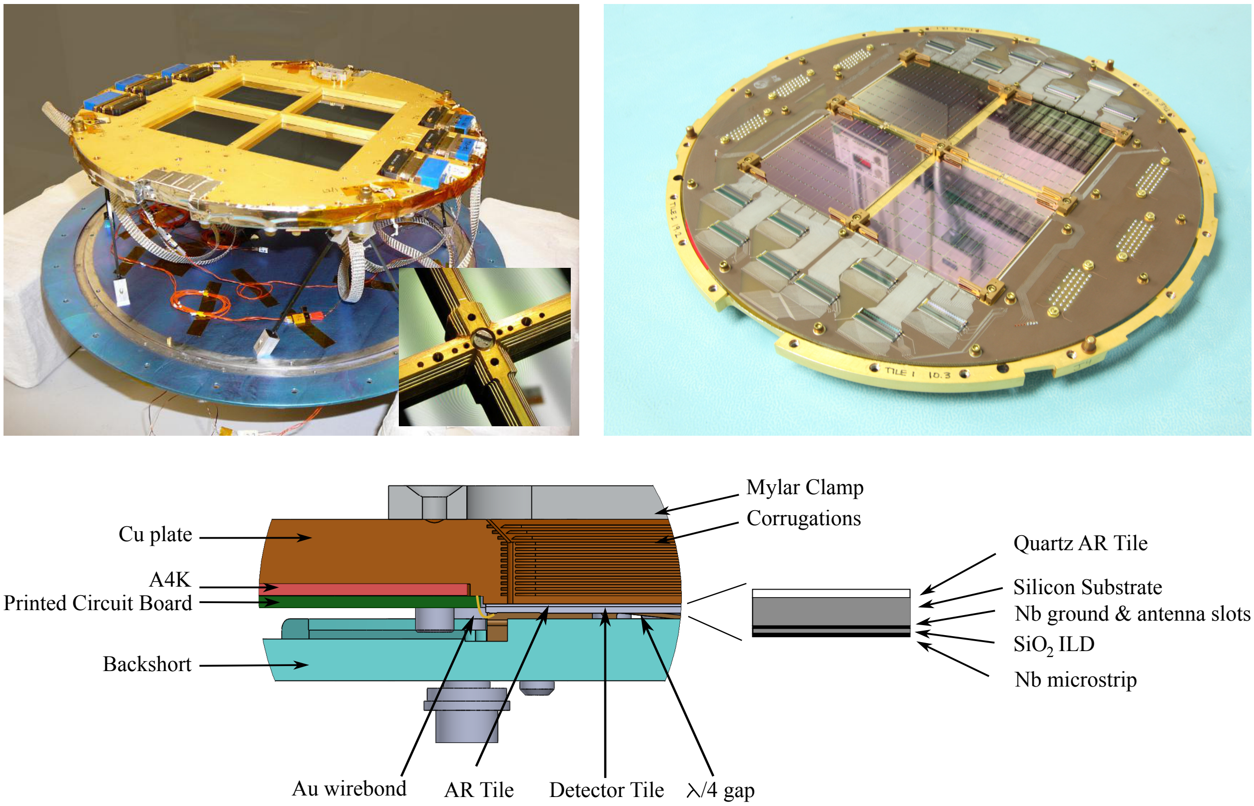

Figure 2.4: Focal plane pictures and cross-section. *Upper*: Top (left) of the BICEP2 focal plane and bottom with backshort removed (right). The arrays of 64 detector pairs per tile are visible at top right. *Lower*: Major component layers of the focal plane design, with an expanded view of the tile layers at right. Gold wire-bonds thermally sink the tiles to the frame and the frame bears corrugations to suppress coupling to the detectors. Only the detectors at the tile perimeter are at risk of frame coupling. Corrugations are visible in the inset photo in the upper left panel.

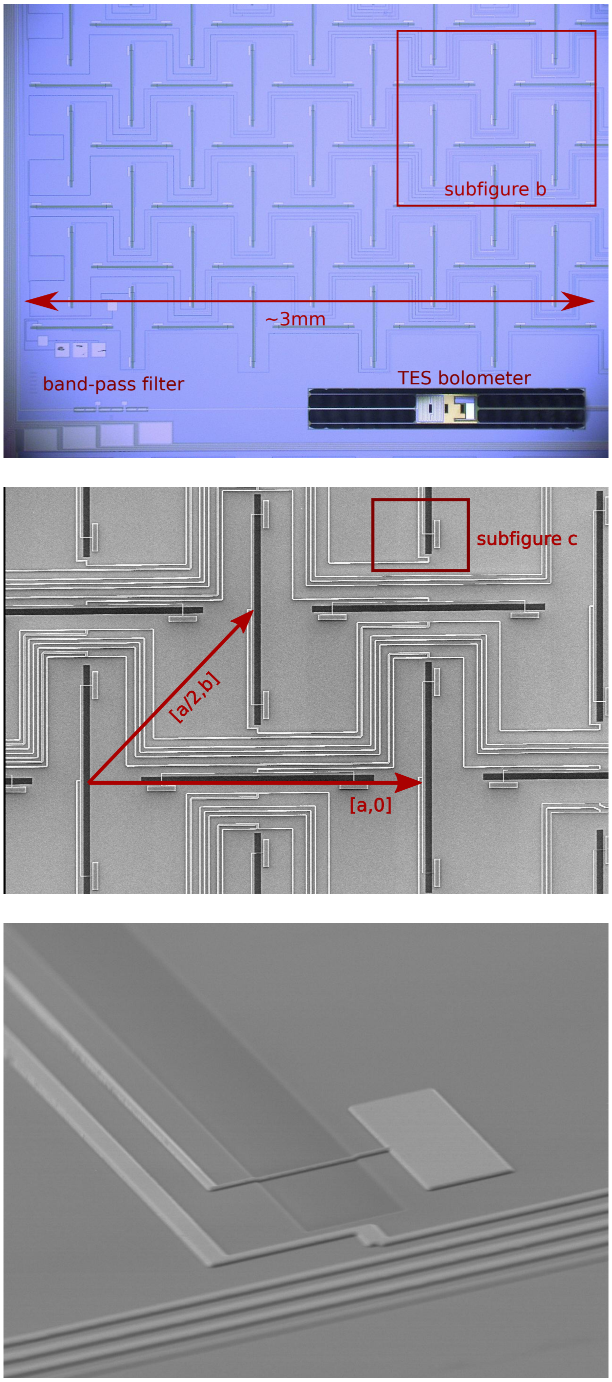

Figure 2.5: Optical and SEM photographs of major features of the antenna array. *Upper*: one quarter of a detector element. The antenna array, one filter, and one TES bolometer are visible, as well as DC readout lines for the detector. *Middle*: SEM micrograph of the slot array (dark rectangles) and oblique Bravais lattice (arrows). The thin white lines comprise the microstrip feed. For 150 GHz detectors, a$\sim$ 600 $\mu$m and $b = a/2 \sim 300$ $\mu$m; the slot dimensions and spacing in the 95 GHz are 63% larger and those in the 220 GHz detector elements are 47% smaller. *Lower*: SEM micrograph of microstrip crossover and shunt capacitor at a sub-antenna slot.

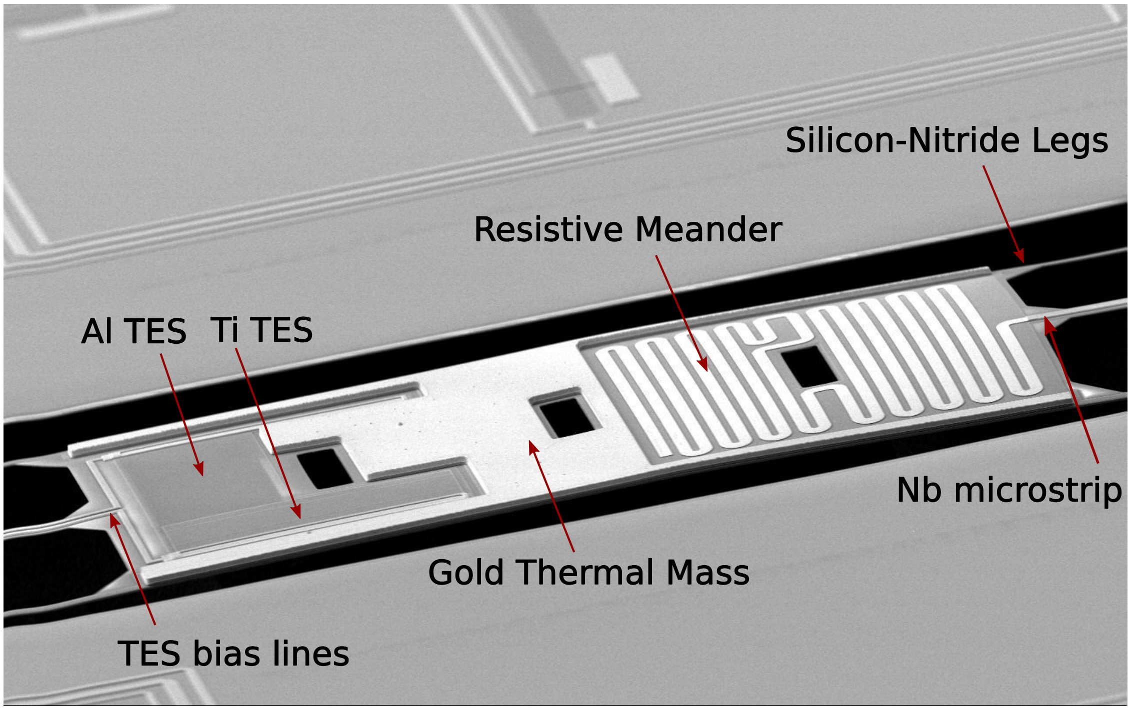

Figure 2.6: Electron micrograph of a released TES bolometer, illustrating its major components. The gold-meandered microstrip termination is at the right of the photograph and the TESs at left. The thicker gold film in the center of the island ensures thermal stability.

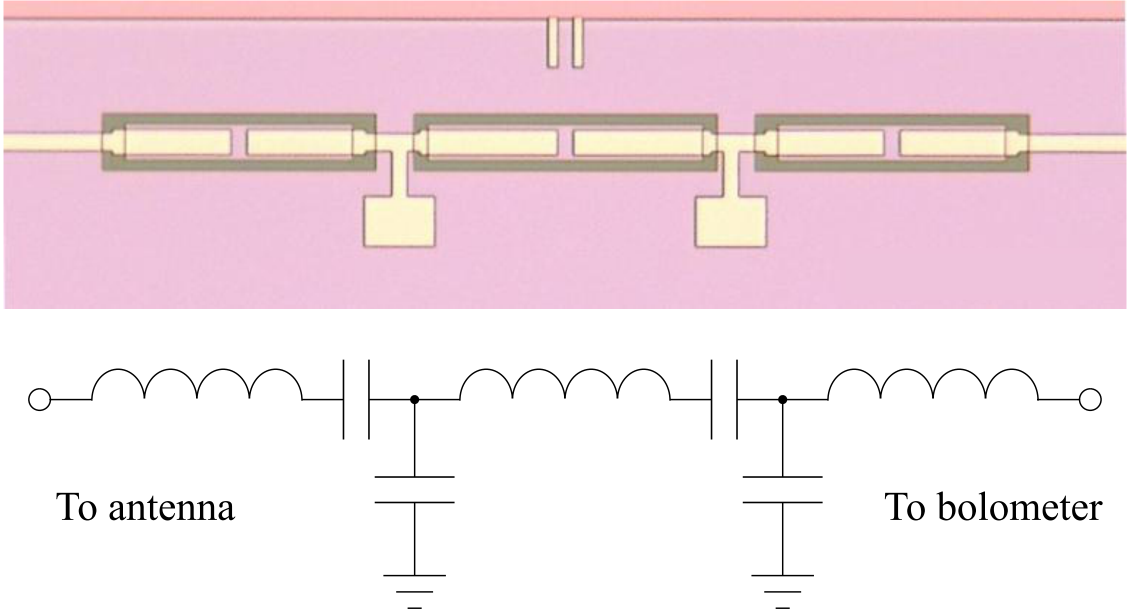

Figure 2.7: Microscope photograph of filter and equivalent circuit for 150 GHz.

the temperature back toward its original value.

BICEP2/*Keck Array* uses a titanium TES and an aluminum TES connected in series. Titanium has a lower superconducting critical temperature $T_c$ than aluminum. When the optical load is relatively low, such as when observing the sky, then the detectors can be biased onto the titanium superconducting transition while the aluminum is superconducting. When the optical load is relatively high, such as when testing in the indoor laboratory at room temperature or when pointed at a bright calibration source, then the titanium TES saturates to normal and instead the detectors use the aluminum TES. The titanium TES is preferred because it has lower noise, but the aluminum TES has the wider dynamic range.

## 2.6 Detector response

This section follows the useful review of the TES by K. D. Irwin and G. C. Hilton [36].

The electrical power to the TES comes from a fixed bias current $I_{\text{bias}}$ supplied by the MCE to a 3 m$\Omega$ shunt resistor in parallel to the TES. At very low bias, all of the current flows through the superconducting titanium. The normal resistance of the titanium $R_{N,\text{Ti}}$ is typically 50-80 m$\Omega$. The operating bias for CMB observation is typically about half of $R_{N,\text{Ti}}$, with values in the range 10-50 m$\Omega$, which is still much larger than the shunt resistance. Since the shunt resistance is small compared to the TES resistance at the titanium operating bias and above, the TES circuit is effectively biased by a voltage $V$ proportional to the MCE's supplied bias current. The TES circuit also has an inductor $L$ and possibly some small parasitic load resistance $R_L$ in series, which leads to the equation

$$V = I(R_{\text{TES}} + R_L) + L\frac{dI}{dt} \tag{2.2}$$

On the titanium transition, $R_L$ is negligible, with perhaps only a small correction due to the finite shunt resistance. On the aluminum transition, $R_L$ is the titanium normal resistance $R_{N,\text{Ti}}$.

In the steady state, the current flowing through the TES is $I = \frac{V}{R_{\text{TES}}+R_L}$. When the TES is either superconducting with $R_{\text{TES}} = 0$ or normally resistive with $R_{\text{TES}} = R_N$, then the current scales linearly with the bias voltage. By sweeping the bias voltage to measure an $I-V$ curve, the TES normal resistance can be inferred from the slope of the linear region.

Suppose that if the bolometer is held at constant bias voltage and optical load, it comes to equilibrium at $I = I_0$, $T = T_0$, and $R_{\text{TES}} = R_0$. We consider the response of the detector to small changes in temperature and current in response to small changes in bias voltage or optical load. The steep superconducting transition is approximately linear over a small enough range, so assume that the logarithmic derivatives $\alpha = \frac{T_0}{R_0} \frac{\partial R}{\partial T}\big|_{I_0}$ and $\beta = \frac{I_0}{R_0} \frac{\partial R}{\partial I}\big|_{T_0}$ are approximately constant. The TES resistance is

$$R_{\text{TES}} \approx R_0 \left(1 + \alpha \frac{\delta T}{T_0} + \beta \frac{\delta I}{I_0}\right) \tag{2.3}$$

The voltage across the TES and parasitic resistance changes as

$$\begin{aligned}\delta(IR_{\text{TES}}) &= R_0 \delta I + I_0 \delta R = R_0 \delta I + I_0 R_0 \left(\alpha \frac{\delta T}{T_0} + \beta \frac{\delta I}{I_0}\right) \\ &= (1+\beta) R_0 \delta I + \frac{\mathscr{L} G}{I_0} \delta T \end{aligned} \tag{2.4}$$

where we have defined the loop gain $\mathscr{L} = \frac{\alpha I_0^2 R_0}{G T_0}$. Similarly the Joule power changes as

$$\begin{aligned}\delta(I^2 R_{\text{TES}}) &= 2 I_0 R_0 \delta I + I_0^2 \delta R = 2 I_0 R_0 \delta I + I_0^2 R_0 \left(\alpha \frac{\delta T}{T_0} + \beta \frac{\delta I}{I_0}\right) \\ &= (2+\beta) I_0 R_0 \delta I + \mathscr{L} G \delta T \end{aligned} \tag{2.5}$$

The TES is thus described in the linear regime by the pair of linear differential equations

$$L \frac{d\delta I}{dt} = \delta V - ((1+\beta) R_0 + R_L) \delta I - \frac{\mathscr{L} G}{I_0} \delta T \tag{2.6}$$

$$C \frac{d\delta T}{dt} = \delta P_{\text{opt}} + (2+\beta) I_0 R_0 \delta I + (\mathscr{L} - 1) G \delta T \tag{2.7}$$

The above equations can be rewritten as a matrix equation

$$\frac{d}{dt}\begin{pmatrix}\delta I\\ \\ \delta T\end{pmatrix}=-\begin{pmatrix}\frac{(1+\beta)R_0+R_L}{L} & \frac{\mathscr{L}G}{I_0L}\\ \\ -\frac{I_0R_0(2+\beta)}{C} & \frac{(1-\mathscr{L})G}{C}\end{pmatrix}\begin{pmatrix}\delta T\\ \\ \delta I\end{pmatrix}+\begin{pmatrix}\frac{\delta V}{L}\\ \\ \frac{\delta P}{C}\end{pmatrix} \tag{2.8}$$

The system can be solved for a sinusoidally varying optical source by finding the eigenvalues of the matrix [36]. Below we consider the simpler solution of the long term response to step changes in $\delta P$ or $\delta V$. This is valid for low frequency signals if the time constants are fast relative to the sample rate. The inductors for BICEP2/*Keck Array* are 1.3-2.0 $\mu$H so that the electrical time constant is 30-200 $\mu$s, which corresponds to a cutoff of 5-33 kHz. A small amount of gold on the TES island gives them heat capacity 0.3-0.5 pJ/K. The optimal thermal conductance depends on the frequency band, and at 150 GHz is nominally about 80 pW/K. The large loop gain on transition greatly reduces the thermal time constant. For BICEP2, the time constants for most detectors was measured to be 0.9 ms and up to 3 ms for detectors biased very high in the transition, which corresponds to a cutoff of 0.3-1 kHz. This is fast relative to the 180 Hz sample rate used during calibrations or the 20 Hz sample rate used during CMB observation.

After the system comes to a new equilibrium, the derivatives are zero. The solution is therefore just a matrix inverse

$$\begin{pmatrix}\delta I\\ \\ \delta T\end{pmatrix}=\begin{pmatrix}\frac{(1+\beta)R_0+R_L}{L} & \frac{\mathscr{L}G}{I_0L}\\ \\ -\frac{I_0R_0(2+\beta)}{C} & \frac{(1-\mathscr{L})G}{C}\end{pmatrix}^{-1}\begin{pmatrix}\frac{\delta V}{L}\\ \\ \frac{\delta P}{G}\end{pmatrix} \tag{2.9}$$

In particular, the change in current is

$$\delta I=\frac{1}{(1-\mathscr{L})((1+\beta)R_0+R_L)+\mathscr{L}(2+\beta)R_0}\left((1-\mathscr{L})\delta V+\frac{\mathscr{L}\delta P}{I_0}\right) \tag{2.10}$$

The above simplifies in two important cases. First, if the TES is superconducting or normal with $\mathscr{L}=0$, then the detector is not optically responsive. Second, if the TES is at the very steep part of the transition with $\mathscr{L}\gg 1$, then the response is

$$\delta I=\frac{-1}{R_0-R_L}\left(\delta V+\frac{\delta P}{I_0}\right) \tag{2.11}$$

Note that this equation depends only on the bias circuit parameters and is independent of the intrinsic TES thermal parameters. A calibration of the electrical response can therefore be used to calibrate the optical response.

A partial load curve is a small voltage sweep near the operating bias with fixed optical power. In the high loop gain limit it can be rewritten as a differential equation valid near the operating bias

$$\frac{\partial V}{\partial I} = -R_0 + R_L = -\frac{V}{I} + 2R_L \tag{2.12}$$

Its solution is

$$V(I) = \frac{I_0^2 R_0}{I} + IR_L \tag{2.13}$$

The Joule power across the TES $P_{\mathrm{J}} = I_0^2 R_0$ stays approximately constant through the transition while $\beta = -2$. (Of course in practice the Joule power gradually increases, albeit slowly.) If $R_L = 0$ such as on the titanium transition, then it inverts to

$$I(V) = \frac{V_0^2}{R_0 V} \tag{2.14}$$

If $R_L > 0$ such as on the aluminum transition, then it inverts to

$$I(V) = \frac{V - \sqrt{V^2 - \frac{4R_0 R_L V_0^2}{(R_0+R_L)^2}}}{2R_L} \tag{2.15}$$

The partial load curve gives a calibration of the optical response near the operating point. On the titanium transition with $R_L = 0$, the optical response is

$$\frac{\partial I}{\partial P_{\mathrm{opt}}} = -\frac{1}{I_0 R_0} \tag{2.16}$$

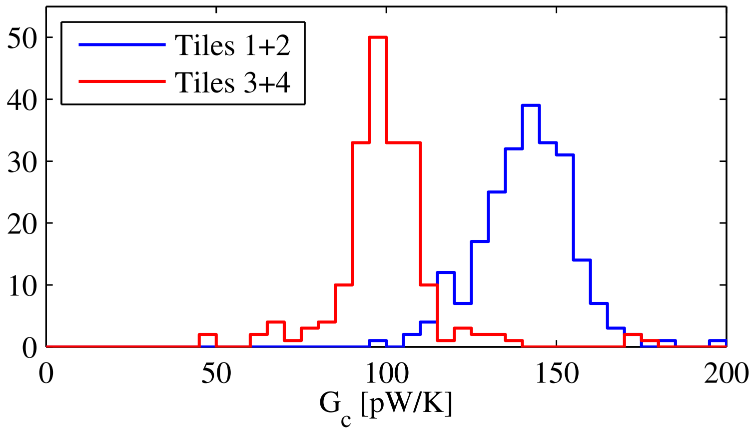

Figure 2.8: Thermal conductance of the Bicep2 detectors at $T_c$. This figure demonstrates repeatability within and between tiles.

## 2.7 Detector thermal conductance

The thermal conductance $G$ of the legs is modeled by a power law near the superconducting critical temperature $T_c$

$$G = \frac{dP_{\text{bath}}}{dT} = G_c \left(\frac{T}{T_c}\right)^n \tag{2.17}$$

The exponent indicates the type of particles dissipating the heat through the legs, with $n = 1$ for electrons and $n = 3$ for phonons. At operating temperature $T_0$, the amount of power that the detector can dissipate without saturating to normal conductivity is

$$P_{\text{sat}} = \int_{T_0}^{T_c} G dT = G_c T_c \frac{1 - (T_0/T_c)^n}{n+1} \tag{2.18}$$

The dark detectors, or the detectors on a shaded tile, see $P_{\text{opt}} = 0$. For $R_L = 0$, the titanium transition saturates at the lowest voltage satisfying the linear relation $I = \frac{V}{R_{N,\text{Ti}}}$, as they begin to be normally resistive. In order to measure $G_c$, $T_c$, and $n$, a heater is applied to the FPU to raise the bath temperature in several steps from 250 mK to 500 mK, and a load curve determines the saturation power $P_{\text{sat}} = \frac{V^2}{R_{N,\text{Ti}}}$ at each temperature step. The Bicep2/*Keck Array* detectors typically follow the power law model with $n = 2.5$.

## 2.8 SQUID readout

The current passing through the TES is read out with a series of time-domain multiplexed SQUID amplifiers, provided by NIST. The amplifiers are in three stages, denoted SQUID1, SQUID2, and SSA (SQUID series array). Within an individual cryostat, they are organized into 32 "rows" plus 1 dark row (not connected to any detector) and 16 "columns" of detectors. Each SQUID1 is assigned a row and column index for the total of 512 detectors and 16 dark SQUIDs. All of the SQUID1s within a row receive the same bias to reduce the amount of cryogenic wiring. Each SQUID2 and SSA is assigned a column. The MCE cycles through the 33 rows, biasing only one row of SQUID1s at a time. The active row of SQUID1s couple to the 16 SQUID2s, which in turn couple to the 16 SSAs.

The voltage across a SQUID is a periodic function of the magnetic flux through it. Feedback loops are needed to keep the three stages of SQUIDs near the steep linear response. A large discussion of the optimization of the SQUID servo is given in S. A. Kernasovskiy's thesis [43]. Another useful resource, particularly in relation to the MCE, is M. Hasselfield's thesis [33], which describes the same optimization for ACT. Ultimately the voltage across the SSA is used to determine the amount of feedback to apply to the SQUID1. The SQUID1 is inductively coupled to both the TES circuit and a feedback circuit. The magnetic flux through the SQUID1 is proportional to the sum of TES current and feedback current, up to constants. As the current increases through the TES circuit, the SQUID1 feedback must decrease to maintain the same amount of magnetic flux. Therefore the SQUID1 feedback is proportional to the TES current and is used as the raw signal.

As SQUIDs are magnetically sensitive devices, they are all enclosed behind magnetic shielding to prevent pickup of external magnetic fields. The design and simulations of the magnetic shielding are in R. W. Aikin's thesis [2]. Measurements of the magnetic pickup in *Keck Array* are in S. A. Kernasovskiy's thesis [43].

## 2.9 Noise performance and sample rate

The noise in the detectors in the signal band is dominated by photon noise from the incident optical power and, to a lesser extent, phonon noise from thermal fluctuations across the bolometer legs. The noise is customarily expressed as a noise-equivalent power (NEP). The photon noise is

$$\mathrm{NEP}^2_{\mathrm{photon}} = 2h\nu P_{\mathrm{opt}} + \frac{2P^2_{\mathrm{opt}}}{\Delta\nu} \tag{2.19}$$

The phonon noise is

$$\mathrm{NEP}^2_{\mathrm{phonon}} = 4k_{\mathrm{B}}T_c^2 G_c F(T_c, T_o) \tag{2.20}$$

where $F(T_c, T_o)$ is a factor of 0.5-1 to account for the thermal gradient across the legs [51]. Low values of $G_c$ keep the phonon noise low. On the other hand, if $G_c$ is too low, then the detectors may saturate.

The electrothermal feedback suppresses the Johnson noise in the TES circuit at low frequencies. At higher frequencies, the modeled Johnson noise increases, but not by as much as the measured high frequency noise. There is an excess high frequency component to the TES noise that becomes dominant over photon and phonon noise above about 100-200 Hz [29].

CMB features at $\ell = 20$ to 500 appear in the time-ordered data at 0.05-2.6 Hz. The sample rate must be at least as fast in order to measure these angular scales. Although only the low frequency TES response is important for CMB observation, the high frequency excess noise can alias down to lower frequencies. The MCE can sample up to a rate of 50 MHz. It must switch between the 33 rows, which causes a brief transient. The MCE allows 60 samples for the transient to settle and records the average of the last samples. The SQUID1 feedback is thus sampled at 25 kHz, which is above the cutoff imposed by the TES circuit's electrical time constant for most detectors. An anti-aliasing filter is applied to reduce the high frequency TES noise. The MCE then downsamples and reports the SQUID1 feedback at 180 Hz.

For partial load curves or other limited calibration data, the 180 Hz data are recorded. If left running continuously, however, this sample rate would produce a large volume of data, which could not be transmitted daily from the South Pole over the communications satellites. Therefore, during regular CMB observation, GCP applies another anti-aliasing filter and records the data at 9 Hz, which is adequate for the science goals. The known MCE and GCP filters are deconvolved in low-level analysis, and a 5 Hz low pass filter is applied during the deconvolution.

## 2.10 Beam mapping

The spectral intensity received by a polarization-sensitive antenna to an unpolarized source of spectral radiance $L_\nu(\theta, \phi)$

$$\frac{dP_\nu}{d\Omega} = \frac{1}{2} A_{\text{eff}}(\nu, \theta, \phi) L_\nu(\theta, \phi) \tag{2.21}$$

The effective area is

$$A_{\text{eff}}(\nu, \theta, \phi) = \frac{c^2}{4\pi\nu^2} \eta(\nu) D(\nu, \theta, \phi) \tag{2.22}$$

where $\eta(\nu)$ is the optical efficiency as a function of frequency and $D(\nu, \theta, \phi)$ is the directive gain, normalized by $\int D(\nu, \theta, \phi) d\Omega = 1$. The effective area for a lossless antenna averaged over all solid angle is

$$\langle A_{\text{eff}}(\nu, \theta, \phi) \rangle = \frac{c^2}{4\pi\nu^2} = \frac{\lambda^2}{4\pi} \tag{2.23}$$

The beams are mapped out by observing a small source with a known spectrum. If the source has a Rayleigh-Jeans spectrum, then its spectral radiance is

$$L_\nu = \frac{2k_{\text{B}} T_{\text{RJ}}}{c^2} \nu^2 \tag{2.24}$$

If it is a point source with support over only a small solid angle $\delta\Omega$ centered at $\theta = \theta_0$ and $\phi = \phi_0$, then the spectral flux is

$$P_\nu \approx \frac{k_{\text{B}} T_{\text{RJ}}}{4\pi} \eta(\nu) D(\nu, \theta_0, \phi_0) \delta\Omega \tag{2.25}$$

In this case the observed beam shape, which is the gain integrated over all frequencies, is also proportional

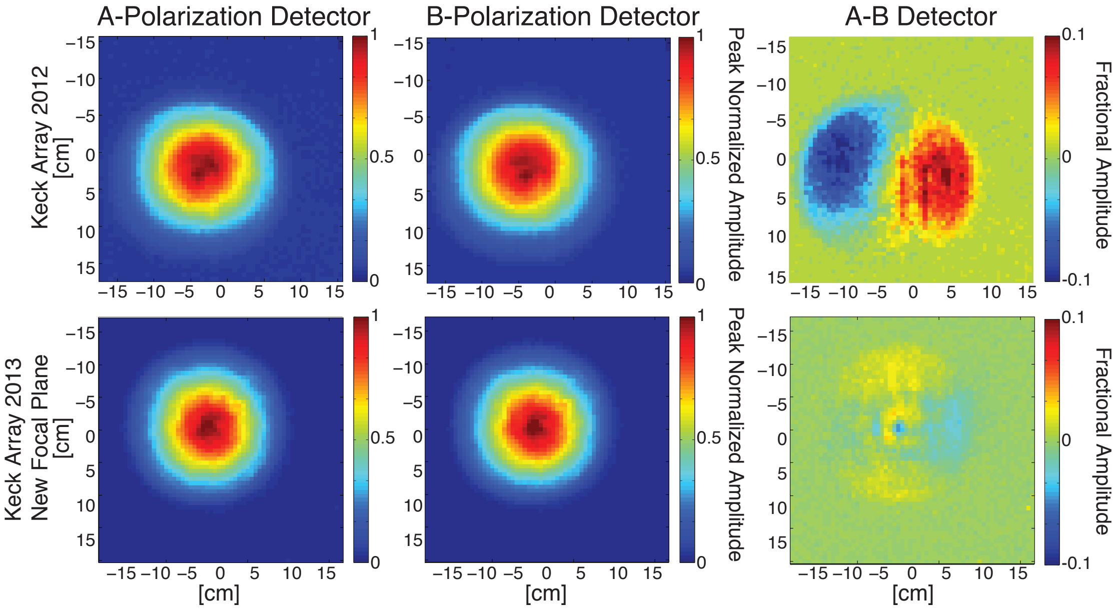

Figure 2.9: An example *Keck Array* detector pair that shows beam mismatch in the near field. *Left*: The optical response of an $A$ polarization detector in a typical detector pair. *Center*: The optical response of the co-located $B$ polarization detector. *Right*: The fractional difference between the $A$ and $B$ optical response. The top panels show a typical detector pair from a focal plane in 2012, and the bottom panels show a typical detector pair from the focal plane installed in 2013 with dramatically reduced differential pointing. See Section 2.16 for discussion.

to the total optical power

$$B(\theta_0, \phi_0) \propto \int \eta(\nu) D(\nu, \theta_0, \phi_0) d\nu \propto P_{\mathrm{opt}} \tag{2.26}$$

Thus the beam is mapped out by moving the source around relative to the receiver and measuring the relative signal.

The near field beam mapper is a chopped thermal source mounted to a two-axis translation stage that can attach directly in front of the cryostat window for performing this measurement in the near field. The near field source is a hot porcelain block behind a 7 mm aperture. Far field maps are taken by scanning the telescope across a chopped source mounted to a tall mast. BICEP2 points toward a source on a mast at MAPO (195 m away), and *Keck Array* points toward a source on a mast at DSL (211 m away). Neither mast is tall enough to be seen within the range of motion of the opposite building's telescope, so the signal is reflected off a flat mirror attached above the telescope. The far field source is either a reflection of the cold sky through 25 or 45 cm apertures or a rotating, polarized, broad-spectrum noise source (BSNS). The beam mapping equipment and results are described further in BK–IV and C. L. Wong's thesis [91].

## 2.11 Pointing

An optical camera is mounted collinear with the microwave receivers. The absolute pointing information of the mount as a whole is determined by pointing at bright stars. The camera has a 700 nm long-pass edge filter to improve the contrast when the sun is above the horizon. The raw mount position encoders are recorded when the stars are centered in the camera. The star observations are used to fit a seven-parameter pointing model to transform the raw encoder coordinates into azimuth and elevation of the telescope.

The far field beam maps give estimates of the relative pointing centers for each pixel. The absolute pointing is not determined by the far field beam maps because of the variation of the source position and the flat mirror alignment. There is also parallax, especially for *Keck Array*.

The final pointing information comes from comparing the data to the CMB temperature as measured externally by WMAP or *Planck*. Temperature maps are accumulated on a per-pixel basis to form "pairmaps" using the mapmaking procedure described in Section 3.3. The pairmaps are shifted near their nominal centers until their correlation with the template is maximized. The pointing centers derived from the CMB are $\sim 0.3$ arcmin away from those derived from the far field beam maps.

For *Keck Array*, the preferred pointing centers derived from pairmaps accumulated while the telescope used half of its azimuth track were found to disagree with the centers derived from the other half of the track by about $\sim 3$ arcmin. The residual between the starpointing model best fit and the data was at this level in 2013 and 2014 and comes from uneven wear to the azimuth track and an error in the execution of the starpointing schedule. This effect is corrected in the analysis by assuming pointing centers that are shifted by a four-parameter model relative to the common pointing center that depends on the deck angle and the half of azimuth track. The *Keck Array* temperature maps would fail an azimuth-split jackknife without this correction, but it is not very important for polarization on large angular scales.

## 2.12 Absolute polarization angle and efficiency

The ideal polarization angle is set by the square FPU geometry itself. The polarization axes should align with the detector rows and columns.

An external absolute polarization angle comes from a technique using a dielectric sheet as described in the Bicep1 instrument paper [85]. The dielectric sheet calibrator, shown in Figure 2.10, worked as a partially polarized beam splitter, directing one polarization mode to the cold sky and the orthogonal mode to a warm microwave absorber at ambient temperature [41]. Because of this temperature contrast, the arrangement acted as a polarized beam-filling source. By rotating Bicep2 about its boresight beneath this source, we obtained a precise measurement of the polarized response of each detector as a function of source angle. *Keck Array* has a similar system, but its calibrator rotates around each receiver's boresight. This technique is fast and precise but also sensitive to the exact alignment of the calibrator.

Another absolute measurement comes from beam maps of the rotating BSNS. The source is a highly linearly polarized signal. In front of the source is a wire grid, and the alignment of the grid can be compared under a microscope to a reference protractor. Beam maps are taken at multiple source angles $\psi_{\mathrm{source}}$. The amplitude of the beam maps are a function the relative polarization angle and the cross polar response $\epsilon$ as

$$A \propto \left(\cos\left(2(\psi_{\mathrm{source}} + \psi_{\mathrm{det}})\right) + \frac{1+\epsilon}{1-\epsilon}\right)\left(1 + C\cos\left(\psi_{\mathrm{source}} - \psi_0\right)\right) \tag{2.27}$$

where $C\cos\left(\psi_{\mathrm{source}} - \psi_0\right)$ is a source collimation term. Figure 2.12 shows a fit of this model to the beam map amplitude for 24 grid angles of the rotating BSNS. The cross polar response is found to be low, about 0.4%, consistent with the electrical crosstalk in the readout and the direct stimulation of the TES island (observed as residual optical power in the dark pixels). Figure 2.11 shows an estimate of the cross polar beams. For more information, see BK–IV [13].

An absolute angle offset is completely degenerate with a uniform cosmic birefringence signal. The final polarization angle used for the experiment minimized the $TB$ and $EB$ cross-spectra under the constraint of minimizing such a signal. Applying this method comes with the penalty that Bicep2/*Keck Array* has

Figure 2.10: A picture of the dielectric sheet calibrator installed on the Bicep1 telescope. We used this calibrator to measure the polarization angle and cross-polar response of Bicep2 as well.

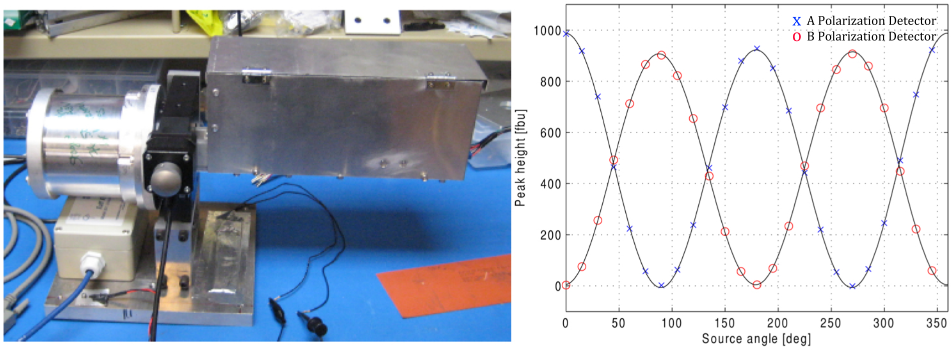

Figure 2.11: Left: The rotating polarized amplified thermal broad-spectrum noise source used for polarization characterization. Right: Polarization modulation vs. source angle of an example detector pair from Bicep2, measured using the rotating polarized source.

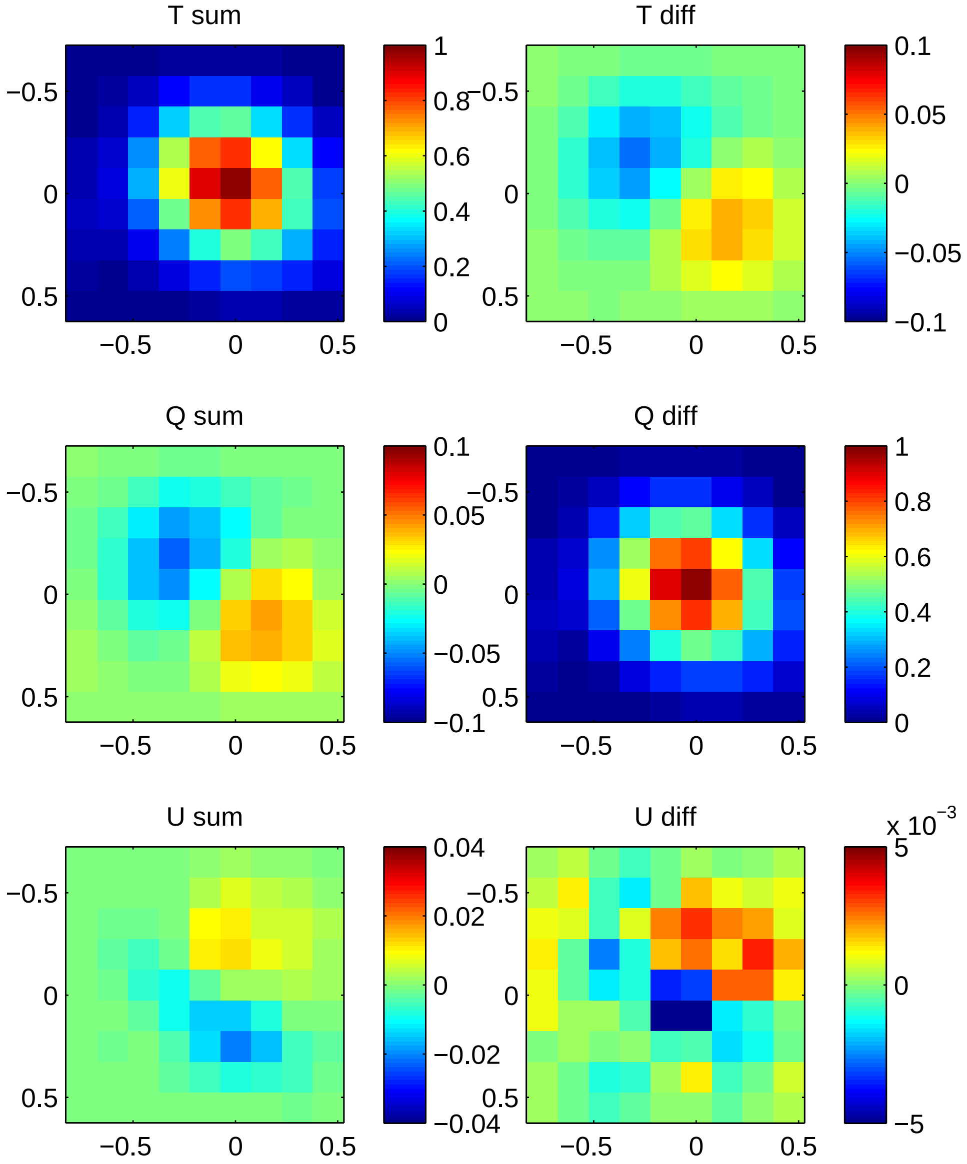

Figure 2.12: The Stokes $T$, $Q$, and $U$ beam maps ($B_T$, $B_Q$, and $B_U$) for a single typical pixel in BICEP2 from measurements of a rotating polarized source. The images have been smoothed with a 0.1° Gaussian kernel. The left column shows the response of the sum of the detectors in a pair; the right column shows the pair difference response. The pair difference $B_T$ and pair sum $B_Q$ both show the differential pointing present in BICEP2. An ideal instrument would have no $U$ response. Only the pair difference beams are relevant to BICEP2 polarization analysis. The small ($\lesssim 0.8\%$) features in the pair difference $B_U$ cause a negligible amount of $E$-to-$B$ leakage. The larger feature in the pair sum $B_U$ beam would cause polarization to temperature leakage, which is harmless. Note that the color scales are not uniform across panels.

no constraining power on cosmic birefringence. The angle needed to minimize cosmic birefringence is about −1.1° for BICEP2 and about −0.5° for *Keck Array*. The combined BICEP2 and *Keck Array* 150 GHz data collected through 2014 prefer a rotation of −0.6°. We do not believe these angles to be a physical birefringence because of the difficulty controlling the reference angle of the calibrators. Furthermore, the cross-spectra between the angle-corrected BK150 data and the *Planck* 143 GHz data (see Section 5.4) show neither evidence for significant decorrelation in $EE$ nor a significant leakage to $EB$ [10].

## 2.13 Optical efficiency and spectral response

We can write $\eta_\nu$ as the product of an effective, frequency-independent optical efficiency $\eta_{\mathrm{eff}}$ and a spectral response function $S(\nu)$

$$\eta_\nu = \eta_{\mathrm{eff}} S(\nu) \tag{2.28}$$

with effective bandwidth

$$\Delta\nu_{\mathrm{eff}} = \int S(\nu) d\nu \tag{2.29}$$

The relative normalization of the two components is arbitrary, subject only to the constraint $0 \leq \eta_\nu \leq 1$. A convenient choice is to let $\eta_{\mathrm{eff}}$ be the average value weighted by a power of itself

$$\eta_{\mathrm{eff}} = \frac{\int \eta_{\nu'}^{p+1} d\nu'}{\int \eta_{\nu'}^{p} d\nu'} \tag{2.30}$$

$$S(\nu) = \frac{\eta_\nu \int \eta_{\nu'}^{p} d\nu'}{\int \eta_{\nu'}^{p+1} d\nu'} \tag{2.31}$$

with $p > 0$ because, for a top hat spectrum, $\eta_{\mathrm{eff}}$ is the height of the top hat and $\Delta\nu_{\mathrm{eff}}$ is its width. For different shapes, the limit $p \to 0$ has a wide bandwidth at low optical efficiency, whereas the limit $p \to \infty$ has a narrow bandwidth at high optical efficiency. A compromise to approximate the original shape is $p = 1$.

In that case the spectral response has the property

$$\Delta\nu_{\mathrm{eff}} = \int S^2(\nu)d\nu \tag{2.32}$$

The bandwidth can just as easily be calculated from any unnormalized spectral response $s(\nu)$ by

$$\Delta\nu_{\mathrm{eff}} = \frac{\left(\int s(\nu)d\nu\right)^2}{\int s^2(\nu)d\nu} \tag{2.33}$$

If the source is uniformly beam-filling, then the integral over solid angle gives the spectral flux

$$P_\nu = \frac{1}{2}\eta_{\mathrm{eff}}S(\nu)\frac{c^2}{\nu^2}L_\nu \tag{2.34}$$

If the source has a Rayleigh-Jeans spectrum, then the spectral flux is

$$P_\nu = \eta_{\mathrm{eff}}S(\nu)k_{\mathrm{B}}T_{\mathrm{RJ}} \tag{2.35}$$

The radiant flux from a beam-filling, Rayleigh-Jeans source is therefore

$$P_{\mathrm{opt}} = \eta_{\mathrm{eff}}k_{\mathrm{B}}T_{\mathrm{RJ}}\Delta\nu_{\mathrm{eff}} \tag{2.36}$$

and an unnormalized spectral response is

$$s(\nu) \propto P_\nu \tag{2.37}$$

## 2.14 Optical efficiency measurement

An increase in optical load decreases the Joule power in the TES circuit. A cone blackened with Eccosorb AN[6] is placed over the cryostat window to act as a beam-filling, Rayleigh-Jeans source. The cone can

---

[6] `http://www.eccosorb.com/`

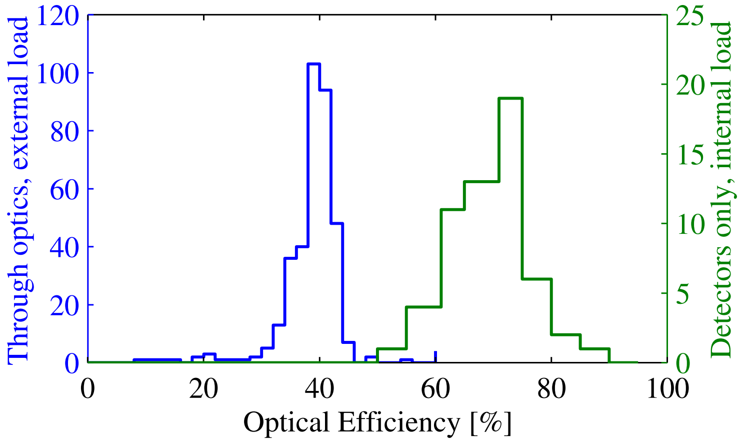

Figure 2.13: Optical efficiencies of Bicep2 detectors. Blue curves (left-axis) are end-to-end receiver efficiency through all optics; green curves (right-axis) are raw detector efficiencies for a single test-tile from an engineering-grad test focal plane, in response to an internal cold-load.

be left at room temperature or cooled with liquid nitrogen. On the aluminum transition, with the FPU temperature stable, a load curve determines the Joule power with room temperature optical loading and another determines it at liquid nitrogen temperature optical loading

$$P_{\text{opt,room}} + P_{\text{J,room}} = P_{\text{opt,LN}} + P_{\text{J,LN}} \tag{2.38}$$

The effective optical efficiency is therefore

$$\eta_{\text{eff}} = \frac{P_{\text{J,LN}} - P_{\text{J,room}}}{k_{\text{B}}(T_{\text{RJ,room}} - T_{\text{RJ,LN}})\Delta\nu_{\text{eff}}} \tag{2.39}$$

## 2.15 Spectral response measurement

The spectral response is needed to determine the optical power from source with a general spectral radiance that may not necessarily have a Rayleigh-Jeans spectrum, including the CMB. If the spectral response of the two detectors within a pixel are slightly different, then the differential response to general sources may induce a false polarization signal. Matching the spectral response between the detectors is important to

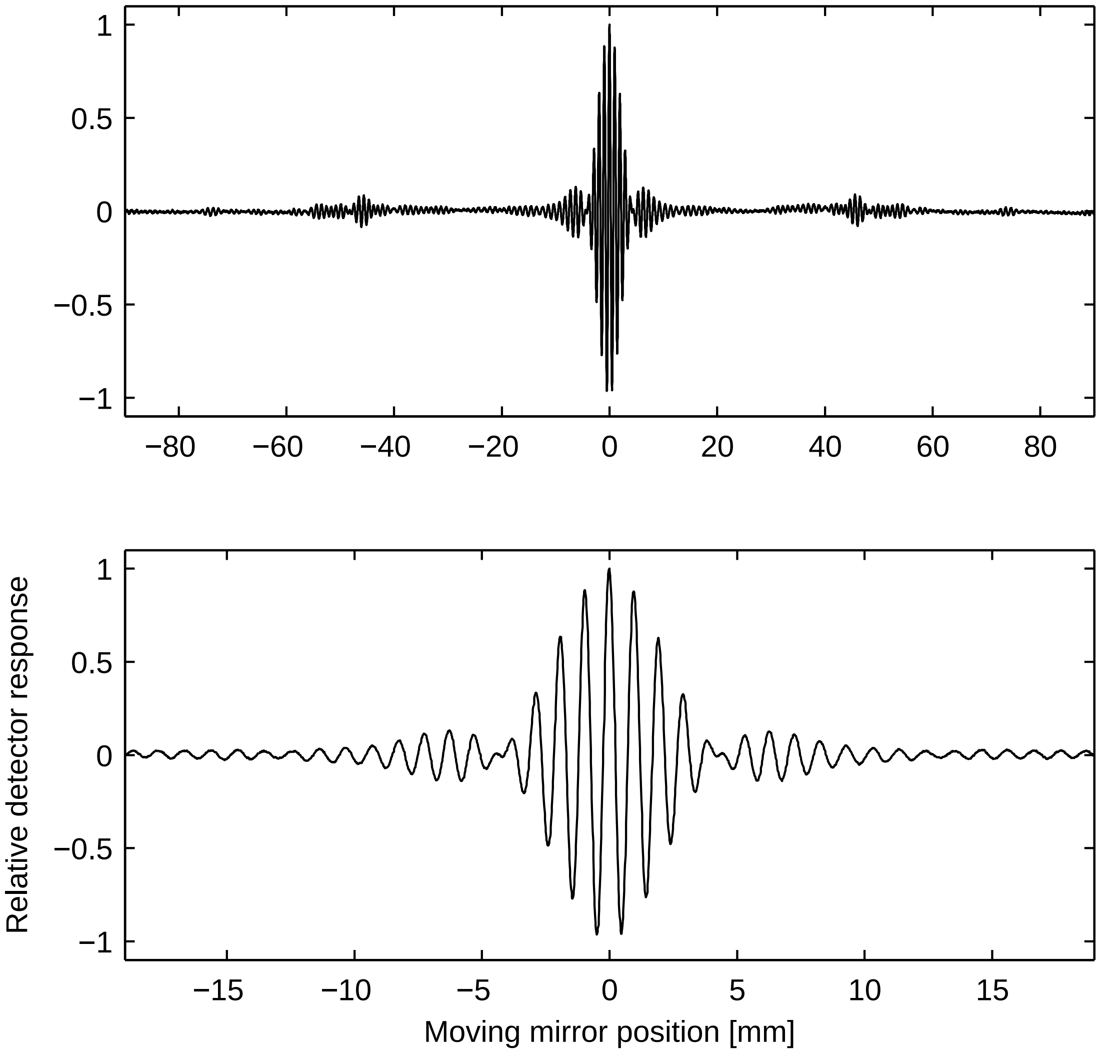

Figure 2.14: Interferogram of a 150 GHz detector. The data are of a detector on tile 1 of rx4. The FTS was placed over the cryostat window while the receiver was in the telescope mount at the South Pole. The signal is the difference in optical power relative to the background with no source spectrum or aperture corrections. The ∼1 mm spacing between the fringes agrees with the 150 GHz band center. Note that the top and bottom plots are of the same data but with different axis limits.

prevent such a systematic error. The band centers are the expectation values

$$\nu_0 = \frac{\int \nu s(\nu) d\nu}{\int s(\nu) d\nu} \tag{2.40}$$

The spectral response also needs to be reduced to the effective bandwidth $\nu_{\mathrm{eff}}$ to determine the effective optical efficiency above.

The Fourier transform spectrometer (FTS) is a Martin–Puplett interferometer [48] that can be mounted directly to the front of the cryostat. It contrasts the room temperature to a bath of liquid nitrogen. One mirror is at a fixed distance from the beam splitter and the other mirrors is on a translation stage that can adjust the path length to the beam splitter. When the two mirrors are the same distance from the beam splitter, then radiation of all wavelengths constructively interfere. When the moveable mirror is translated by a distance $x$ relative to the zero differential path position, then wavelengths $2nx$ constructively interfere whereas wavelengths $(2n-1)x$ destructively interfere. More generally the mirror is swept through the length of the translation stage at a fixed speed to produce an interferogram. The spectral response of the detectors is the cosine transform of the interferogram.

Figure 2.14 is an example interferogram of actual data of a 150 GHz detector. Aggregate spectra derived from interferograms of multiple detectors are shown in Figure 2.15. More photos and data are available in conference proceedings [39].

A complication arises in that the FTS, which has a 126 mm aperture, does not fill the beams. The spectral flux is proportional to the spectral response times the integral of $D(\nu, \theta, \phi)$ over the FTS aperture. The directive gain can be estimated from the near field beam maps or calculated from the theoretical antenna pattern of the uniformly illuminated, square pixels, truncated by the cold aperture stop. The fraction of the beam filled by the FTS is approximated by a power law over a narrow range of frequencies about the central frequency $\nu_0$

$$\int_{\mathrm{FTS}} D(\nu, \theta, \phi) d\Omega \propto \nu^n \tag{2.41}$$

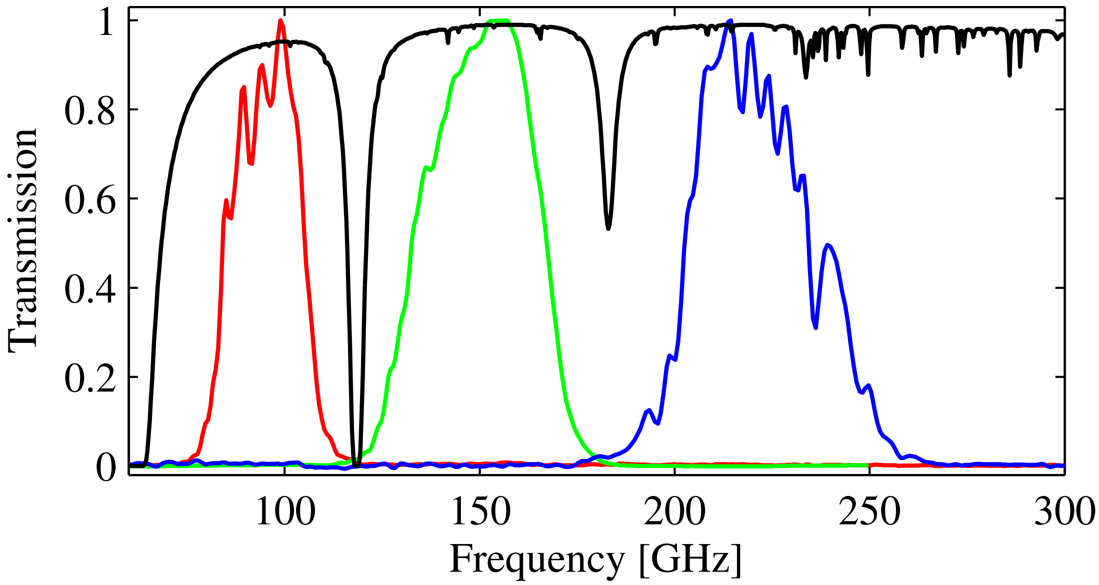

Figure 2.15: Measured detector spectral response for devices designed for 95 GHz (red), 150 GHz (green), and 230 GHz (blue). The data for 150 GHz are from BICEP2 while the others are from *Short Keck*. The spectra are normalized by their maximum values. Source spectrum and aperture corrections are not applied. Typical winter atmospheric transmission at the South Pole is overlaid in black.

An unnormalized spectral response is then

$$s(\nu) \propto \frac{P_\nu}{\nu^n} \tag{2.42}$$

Values for $n$ are in table 2.2.

The `am` software by S. Paine[7] is a free, open source program that rapidly provides a model for the radiative characteristics of the atmosphere across the observing band. Using models for the South Pole atmosphere, we find that the variation in absolute calibration among detectors is consistent with the measured variation in detector pass band. These models also show steadier conditions at 100 GHz compared to 150 GHz because of the reduced influence of water vapor. *Keck Array* data with simultaneous observation at 100 and 150 GHz support this. Preliminary data from 2015 with simultaneous observation at 230 GHz as well show the increased effect of water in the higher frequency band.

---

[7] `https://www.cfa.harvard.edu/~spaine/am/`

Table 2.2: Frequency scaling exponent of spectral response

| Band center | $n$ |
|---|---|
| 95 GHz | 0.95 |
| 150 GHz | 1.1 |
| 230 GHz | 1.2 |

## 2.16 Detector screening program

*Short Keck* is a cryostat with similar design specifications as a *Keck Array* cryostat except without the optics tube. This allows for easier FPU installation and reduced cooling time for test runs for screening device properties or defects. Since 2010, *Short Keck* has tested numerous detector tiles for *Keck Array*, BICEP3, and SPIDER as well as specially made tiles used to help characterize the tile properties for improved iterations of fabrication. Many of the results of device testing in *Short Keck* are reported in the Detectors Paper [11].

Once science-grade detector tiles pass screening in *Short Keck*, they are installed and retested in their intended *Keck Array* cryostat at the South Pole. There may be small differences between the performance in *Short Keck* versus in *Keck Array* because of the reduced incidental laboratory activity at the South Pole and the additional optical elements. Detector characterization is performed using test equipment similar to what is used on *Short Keck*, including a beam mapper, an absorptive cone, and an FTS. The FTS used at South Pole also features a two-axis translation stage that allows the FTS to repoint the system through the optics toward specific detectors in the FPU for more optimal coupling. Every *Keck Array* cryostat has its optical efficiency and near field beams remeasured to check for assembly errors before being hoisted into the telescope mount.

*Short Keck* has its own near field beam mapper. On *Short Keck*, the source is in the far field of the antennas without the lenses of a full *Keck Array* receiver. Beam measurements in *Short Keck* have been able to show the side lobes of the antenna pattern, such as in Figure 2.16, which in the full *Keck Array* are normally terminated by the cold aperture stop. Early versions of the detectors showed a pointing mismatch between polarization pairs. Repeated beam measurements of tiles with various corrections to the summing tree of the antennas and the fabrication step that defines the niobium microstrip lines culminated in an

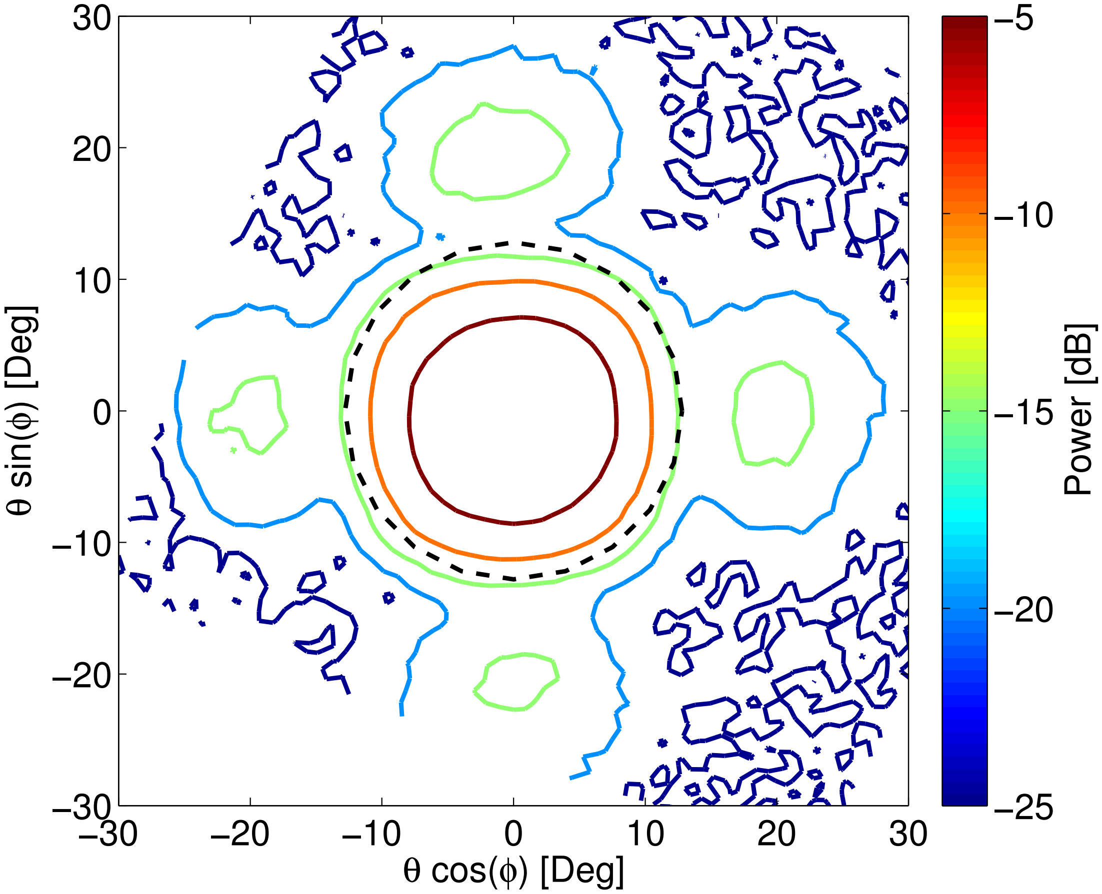

Figure 2.16: Sample far-field detector pattern measured in *Short Keck*, a test cryostat without an optical stop. Power is normalized to peak on boresight and the dashed line indicates where the f/2.2 camera stop would lie.

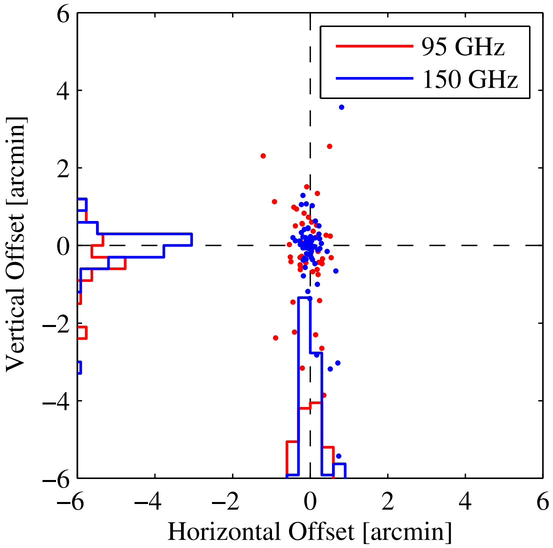

Figure 2.17: Far field beam centroid displacements between detector pairs for two different colors after the niobium microstrip line etch recipe was fixed. See Section 2.16 for discussion.

improved design. We defined our microstrip lines in early tiles with the lift-off technique that we use for the niobium ground plane. Several devices have shown discoloration in this step, leading us to speculate that the niobium leaches organic materials from the resist during lift-off. These observations and modeling inspired a switch to an etch-based means of defining the niobium microstrip lines. This simple fix reduced the scatter in centroid location to $\sim 1\%$ of Gaussian width. Figure 2.17 shows the centroid alignment between polarization pairs for 95 GHz and 150 GHz, with a pointing mismatch of $\lesssim 1$ arcmin for most pixels.

# Chapter 3

# Map making

We briefly review the construction of temperature and polarization maps from raw data. The main purpose of this chapter is to document the Bicep2/*Keck Array* map making analysis pipeline used to build the maps, which are the first science data products of the experiment and are presented in Section 5.1. The formalism is described elsewhere, especially in J. E. Tolan's thesis [87] for the matrix analysis pipeline of Sections 3.6 and 3.7. The second important purpose is to introduce the accumulation quantities that are important for understanding the sign-flip noise simulations of Section 4.4 and for accumulating the deviations and noise covariance matrix as in Sections 4.5 and 4.6.

The chapter begins with a summary of the Bicep2/*Keck Array* scan strategy in Section 3.1. The binning of the raw data time streams from those scans produces accumulation quantities, which are the foundation of the temperature and Stokes $Q/U$ maps. The accumulation of the maps according to the standard pipeline is the subject of Sections 3.2 and 3.3. The transformation from $Q/U$ to $E/B$ is given in Section 3.4 for the full sky and the flat sky approximation. Issues of mode mixing and ambiguity are brought up in Section 3.5, and the observation matrix and purification matrix that correct for these issues are defined in Sections 3.6 and 3.7. Section 3.8 ends the chapter with a simple method for plotting a map that synthetically represents the cross of two maps, although this is unused in the analysis. A small amount of material below was written for BK–I [9] and BK–II [7].

## 3.1 Scan strategy

In regular CMB observation, BICEP2/*Keck Array* scans in azimuth at 2.8°/s while tipped to an elevation centered near 57.5°. A scanset is about 50 consecutive left and right scans across a 56.4° fixed azimuth range at this constant angular speed. A small amount of additional azimuth range is swept as the telescope turns around, but it is excluded from analysis. Partial load curves and el nods are performed before and after each scanset for calibration. The center of the azimuth range is adjusted by 12.5° between scansets to account for the rotation of the sky and is stepped by 0.25° in elevation to vary the detector coverage pattern and increase survey area. In a typical observing schedule, the telescope performs ten consecutive scansets at a similar azimuth and elevation range in what is called a phase. Between phases, the telescope may rotate in deck, point to different fields (CMB or galactic plane), or cycle its helium sorption refrigerator. The phases are listed in Table 3.1. The three-day BICEP2 schedule scheme of Phases A-I is shown in Figure 3.1. *Keck Array* ran two-day schedules of Phases A-F to synchronize the fridge cycles of the five receivers.

Ground subtraction filters out scan-synchronous signals that correlate in azimuth (as opposed to right ascension) over the length of the scanset. At low $\ell$, there is partial degeneracy between an azimuthally-fixed signal and a right ascension-fixed signal. The degeneracy is reduced by increasing the duration of the scanset. For longer scansets, ground subtraction removes fewer modes, and the sensitivity to the CMB at low $\ell$ may improve. In November 2014, *Keck Array* doubled the duration of a scanset to approximately 100 scans. The partial load curve and el nod calibrations are performed in the middle of each double-length scanset so that there is the option of treating it as two scansets of the original 50 scan duration.

## 3.2 T/Q/U maps

Polarization of a light source is in general specified by Stokes parameters $Q$, $U$, and $V$. Since BICEP2/*Keck Array* is not sensitive to circular polarization and most theories generally do not allow circular polarization to be produced in the early universe, the remainder of this thesis assumes $V = 0$. The average values of map pixel $i$ over the full data set are denoted $\overline{T}_i$, $\overline{Q}_i$, and $\overline{U}_i$.

Table 3.1: Phases in a schedule

| Phase | LST | Field |
|---|---|---|
| A | Day 0 23:00 | Cryo service |
| B | Day 1 05:30 | CMB (high el) |
| C | Day 1 14:30 | CMB (low el) |
| D | Day 1 23:00 | Galactic |
| E | Day 2 05:30 | CMB (low el) |
| F | Day 2 14:30 | CMB (high el) |
| G | Day 2 23:00 | CMB (variable el) |
| H | Day 3 05:30 | CMB (high / low el) |
| I | Day 3 14:30 | CMB (low / high el) |

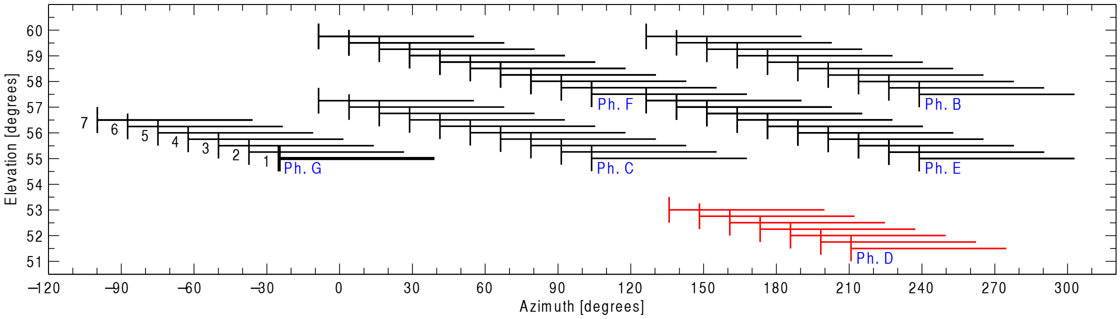

Figure 3.1: Observing pattern of a typical three-day observing schedule for BICEP2. Phase letters are as in Table 3.1. The scansets of Phase G are numbered, with the first scanset at the lowest elevation. The first scanset of Phase G is shown in bold, showing the throw of the field scans (horizontal line) and the bracketing elevation nods (vertical line). The two six-hour phases can vary in elevation: the Galactic D phase is shown at the lowest of four elevation steps, and the CMB G phase is shown at the lowest of three elevation steps. The H and I phases on the third LST day alternate between the B/C pattern and the E/F pattern.

Consider a linear polarization-sensitive detector with gain $g$ and polarization efficiency $\gamma = \frac{1-\epsilon}{1+\epsilon}$. When the detector observes the sky at orientation $\psi$, it sees data

$$d = g(\gamma(Q\cos 2\psi + U\sin 2\psi) + T) \tag{3.1}$$

The calibrated sum and difference between a pair of detectors $a$ and $b$ is

$$d_{\text{sum}} = \frac{1}{2}\left(\frac{d_a}{g_a} + \frac{d_b}{g_b}\right) = \frac{1}{2}(\gamma_a\cos 2\psi_a + \gamma_b\cos 2\psi_b)Q + \frac{1}{2}(\gamma_a\sin 2\psi_a + \gamma_b\sin 2\psi_b)U + T \tag{3.2}$$

$$d_{\text{diff}} = \frac{1}{2}\left(\frac{d_a}{g_a} - \frac{d_b}{g_b}\right) = \frac{1}{2}(\gamma_a\cos 2\psi_a - \gamma_b\cos 2\psi_b)Q + \frac{1}{2}(\gamma_a\sin 2\psi_a - \gamma_b\sin 2\psi_b)U \tag{3.3}$$

The $a$ and $b$ antennas in a BICEP2/*Keck Array* pixel are oriented 90° with respect to each other and have excellent polarization efficiency. BK–III [8] and BK–IV [13] find the cross-polar response to be very low (see Section 2.12), so it is a very good approximation to take $\gamma_a = \gamma_b = 1$. In this limit we have more simply

$$d_{\text{sum}} = T \tag{3.4}$$

$$d_{\text{diff}} = \cos(2\psi_a)Q + \sin(2\psi_a)U \tag{3.5}$$

If the source polarization fraction is small, which is true of the CMB, then $d_{\text{sum}} = T$ is a good approximation regardless. Let $x_{ik} = w_{ik}d_{\text{sum},ik}$ be the measurement of the pair sum while the detectors are pointed at a certain map pixel indexed by $i$ for its $k$th observation, weighted by $w_{ik}$. The weight is typically the inverse variance of the time-ordered data over the duration of the scanset. The temperature map is a weighted average of the measured temperature in all of the scansets

$$\overline{T}_i = \frac{\sum_k x_{ik}}{\sum_k w_{ik}} \tag{3.6}$$

Returning to the general case, we define the polarization orientation information

$$\alpha = \gamma_a \cos 2\psi_a - \gamma_b \cos 2\psi_b \tag{3.7}$$

$$\beta = \gamma_a \sin 2\psi_a - \gamma_b \sin 2\psi_b \tag{3.8}$$

This simplifies the pair difference to $d_{\mathrm{diff}} = \frac{1}{2}(\alpha Q + \beta U)$. We rewrite this as a linear equation

$$\frac{1}{2}\begin{pmatrix} \alpha d_{\mathrm{diff}} \\ \beta d_{\mathrm{diff}} \end{pmatrix} = \frac{1}{4}\begin{pmatrix} \alpha^2 & \alpha\beta \\ \alpha\beta & \beta^2 \end{pmatrix}\begin{pmatrix} Q \\ U \end{pmatrix} \tag{3.9}$$

For a single polarization orientation, the matrix on the right is singular. In order to recover $Q$ and $U$, multiple deck angles are required. Let $\alpha_{ik}$ and $\beta_{ik}$ be the orientation of a detector pair while pointed at a certain map pixel $i$ for its $k$th observation. The accumulated data for that map pixel is a weighted sum of pair differences

$$\sum_k \begin{pmatrix} y_{ik} \\ z_{ik} \end{pmatrix} = \frac{1}{2}\sum_k w_{ik}\begin{pmatrix} \alpha_{ik} d_{\mathrm{diff},ik} \\ \beta_{ik} d_{\mathrm{diff},ik} \end{pmatrix} = \frac{1}{4}\sum_k w_{ik}\begin{pmatrix} \alpha_{ik}^2 & \alpha_{ik}\beta_{ik} \\ \alpha_{ik}\beta_{ik} & \beta_{ik}^2 \end{pmatrix}\begin{pmatrix} Q_i \\ U_i \end{pmatrix} \tag{3.10}$$

Once accumulated over the entire data set, the matrix is inverted. The Stokes parameters become

$$\begin{pmatrix} \overline{Q}_i \\ \overline{U}_i \end{pmatrix} = \frac{1}{\sum_k w_{ik}}\begin{pmatrix} e_i & f_i \\ f_i & g_i \end{pmatrix}\sum_k \begin{pmatrix} y_{ik} \\ z_{ik} \end{pmatrix} \tag{3.11}$$

where the inverse elements are

$$e_i = \frac{4\left(\sum_k w_{ik}\right)\left(\sum_k w_{ik}\beta_{ik}^2\right)}{\left(\sum_k w_{ik}\alpha_{ik}^2\right)\left(\sum_k w_{ik}\beta_{ik}^2\right) - \left(\sum_k w_{ik}\alpha_{ik}\beta_{ik}\right)^2} \tag{3.12}$$

$$f_i = \frac{-4\left(\sum_k w_{ik}\right)\left(\sum_k w_{ik}\alpha\beta\right)}{\left(\sum_k w_{ik}\alpha_{ik}^2\right)\left(\sum_k w_{ik}\beta_{ik}^2\right) - \left(\sum_k w_{ik}\alpha_{ik}\beta_{ik}\right)^2} \tag{3.13}$$

$$g_i = \frac{4\left(\sum_k w_{ik}\right)\left(\sum_k w_{ik}\alpha_{ik}^2\right)}{\left(\sum_k w_{ik}\alpha_{ik}^2\right)\left(\sum_k w_{ik}\beta_{ik}^2\right) - \left(\sum_k w_{ik}\alpha_{ik}\beta_{ik}\right)^2} \tag{3.14}$$

## 3.3 Parallel accumulation

The weighted data quantities $x_{ik}$, $y_{ik}$, and $z_{ik}$ are accumulated over the data set along with their weighted polarization orientation information $w_{ik}$, $\frac{1}{4}w_{ik}\alpha_{ik}^2$, $\frac{1}{4}w_{ik}\beta_{ik}^2$, and $\frac{1}{4}w_{ik}\alpha_{ik}\beta_{ik}$. The accumulation is performed using an analysis pipeline written in Matlab [1] originally used for QUaD [70] and also used for Bicep1 [6]. Table A.1 is a key for the data accumulation quantities in the Matlab analysis pipeline. As long as these accumulation quantities are not inverted into $\overline{T}_i$, $\overline{Q}_i$, and $\overline{U}_i$, their addition is amenable to parallel addition. Therefore it is the accumulation quantities themselves — not $\overline{T}_i$, $\overline{Q}_i$, and $\overline{U}_i$ — which are saved.

The accumulation of the data using only a single detector pair is called a pairmap. Pairmaps are accumulated over the duration of a scanset and saved without any inversion. The scanset pairmaps are accumulated over all detector pairs over the duration of a phase and also saved without any inversion. The deprojection operation, described very briefly in Section 3.6 and at length in R. W. Aikin's thesis [2] and C. D. Sheehy's thesis [80], is applied to the per-phase accumulation quantities. There are no other filters or cuts applied on timescales intermediate between the per-phase accumulation and the full data set. The phases are therefore added together in parallel for reduced computing time. For example, the phases can be accumulated into weekly or monthly accumulation quantities on separate processors and stored in temporary memory. The weeks or months are then accumulated into the full accumulation quantities and saved. The inversion into $\overline{T}_i$, $\overline{Q}_i$, and $\overline{U}_i$ is only done in the last step.

## 3.4 E/B maps

There are two popular conventions for the local coordinate system used to define the polarization axes. The IAU convention is to measure $\psi$ from north to east. The `HEALPix` [30] convention measures $\psi$ from south to east. The effect is that $\psi$ and $U$ have opposite signs in the two conventions. In this section only, except

---

[1] `http://www.mathworks.com/`

where noted, we use the `HEALPix` convention because it is more common in the mathematical literature.

Here we follow primarily the formalism of E. F. Bunn *et al.* [17]. The two linear polarization states $Q$ and $U$ measured across a two-dimensional surface transform under a change of coordinates as spin-2. The expansion in spin-weighted spherical harmonics is

$$Q(\theta,\phi) + iU(\theta,\phi) = \sum_{\ell m} a^{(2)}_{\ell m} \, {}_2Y_{\ell m}(\theta,\phi) \tag{3.15}$$

$$Q(\theta,\phi) - iU(\theta,\phi) = \sum_{\ell m} a^{(-2)}_{\ell m} \, {}_{-2}Y_{\ell m}(\theta,\phi) \tag{3.16}$$

This is inconvenient for relating observables to the symmetries of the primordial universe. It is possible instead to specify linear polarization across the surface as a scalar $E$-mode and a pseudoscalar $B$-mode [78, 37, 79, 93, 38]. The transform is nonlocal, performed in the Fourier domain, with the Fourier coefficients related by

$$a^E_{\ell m} = -\frac{1}{2}\left(a^{(2)}_{\ell m} + a^{(-2)}_{\ell m}\right) \tag{3.17}$$

$$a^B_{\ell m} = \frac{i}{2}\left(a^{(2)}_{\ell m} - a^{(-2)}_{\ell m}\right) \tag{3.18}$$

$E$-mode and $B$-mode maps can optionally be reconstructed via these coefficients using the usual spherical harmonics for spin-0:

$$E(\theta,\phi) = \sum_{\ell m} a^E_{\ell m} \, {}_0Y_{\ell m}(\theta,\phi) \tag{3.19}$$

$$B(\theta,\phi) = \sum_{\ell m} a^B_{\ell m} \, {}_0Y_{\ell m}(\theta,\phi) \tag{3.20}$$

These are invertible to

$$a^{(2)}_{\ell m} = -\left(a^E_{\ell m} + i a^B_{\ell m}\right) \tag{3.21}$$

$$a^{(-2)}_{\ell m} = -\left(a^E_{\ell m} - i a^B_{\ell m}\right) \tag{3.22}$$

$$Q(\theta,\phi) = -\frac{1}{2}\sum_{\ell m}\left(a^E_{\ell m}\left({}_2Y_{\ell m}(\theta,\phi) + {}_{-2}Y_{\ell m}(\theta,\phi)\right) + i a^B_{\ell m}\left({}_2Y_{\ell m}(\theta,\phi) - {}_{-2}Y_{\ell m}(\theta,\phi)\right)\right) \tag{3.23}$$

$$U(\theta,\phi) = -\frac{1}{2}\sum_{\ell m}\left(a^B_{\ell m}\left({}_2Y_{\ell m}(\theta,\phi) + {}_{-2}Y_{\ell m}(\theta,\phi)\right) - ia^E_{\ell m}\left({}_2Y_{\ell m}(\theta,\phi) - {}_{-2}Y_{\ell m}(\theta,\phi)\right)\right) \tag{3.24}$$

This can be written as a vector equation

$$\mathbf{P}(\theta,\phi) = \begin{pmatrix} Q(\theta,\phi) \\ \\ U(\theta,\phi) \end{pmatrix} = -\sum_{\ell m}\left(a^E_{\ell m}\mathbf{Y}^E_{\ell m}(\theta,\phi) + a^B_{\ell m}\mathbf{Y}^B_{\ell m}(\theta,\phi)\right) \tag{3.25}$$

where we introduce the $E$-mode and $B$-mode spherical harmonics

$$\mathbf{Y}^E_{\ell m}(\theta,\phi) = \frac{1}{2}\begin{pmatrix} {}_2Y_{\ell m}(\theta,\phi) + {}_{-2}Y_{\ell m}(\theta,\phi) \\ \\ -i\left({}_2Y_{\ell m}(\theta,\phi) - {}_{-2}Y_{\ell m}(\theta,\phi)\right) \end{pmatrix} \tag{3.26}$$

$$\mathbf{Y}^B_{\ell m}(\theta,\phi) = \frac{1}{2}\begin{pmatrix} i\left({}_2Y_{\ell m}(\theta,\phi) - {}_{-2}Y_{\ell m}(\theta,\phi)\right) \\ \\ {}_2Y_{\ell m}(\theta,\phi) + {}_{-2}Y_{\ell m}(\theta,\phi) \end{pmatrix} \tag{3.27}$$

These functions are orthonormal on the sphere

$$\int \mathbf{Y}^{E\dagger}_{\ell m}(\theta,\phi)\mathbf{Y}^E_{\ell' m'}(\theta,\phi)d\Omega = \int \mathbf{Y}^{B\dagger}_{\ell m}(\theta,\phi)\mathbf{Y}^B_{\ell' m'}(\theta,\phi)d\Omega = \delta_{ll'}\delta_{mm'} \tag{3.28}$$

$$\int \mathbf{Y}^{E\dagger}_{\ell m}(\theta,\phi)\mathbf{Y}^B_{\ell' m'}(\theta,\phi)d\Omega = 0 \tag{3.29}$$

The Fourier coefficients suffice for computing 1D angular power spectra.

$$C^{EE}_\ell = \left\langle |a^E_{\ell m}|^2 \right\rangle = \frac{1}{2\ell+1}\sum_{m=-\ell}^{\ell}|a^E_{\ell m}|^2 \tag{3.30}$$

$$C^{BB}_\ell = \left\langle |a^B_{\ell m}|^2 \right\rangle = \frac{1}{2\ell+1}\sum_{m=-\ell}^{\ell}|a^B_{\ell m}|^2 \tag{3.31}$$

$$C^{EB}_\ell = \left\langle a^E_{\ell m}a^{B*}_{\ell m} \right\rangle = \frac{1}{2\ell+1}\sum_{m=-\ell}^{\ell}a^E_{\ell m}a^{B*}_{\ell m} \tag{3.32}$$

We also introduce the covariance matrices

$$\mathbf{C}_{\mathbf{E}}(\theta,\phi)=\sum_{\ell m} C_\ell^{EE}\mathbf{Y}_{\ell m}^{E}(\theta,\phi)\mathbf{Y}_{\ell m}^{E\dagger}(\theta,\phi) \tag{3.33}$$

$$\mathbf{C}_{\mathbf{B}}(\theta,\phi)=\sum_{\ell m} C_\ell^{BB}\mathbf{Y}_{\ell m}^{B}(\theta,\phi)\mathbf{Y}_{\ell m}^{B\dagger}(\theta,\phi) \tag{3.34}$$

A pure $E$-mode $\mathbf{e}(\theta,\phi)$ satisfies $\mathbf{e}^{\mathrm{T}}(\theta,\phi)\mathbf{Y}_{\ell m}^{B}(\theta,\phi)=0$ for all $\ell$ and $m$, and a pure $B$-mode $\mathbf{b}(\theta,\phi)$ satisfies $\mathbf{b}^{\mathrm{T}}(\theta,\phi)\mathbf{Y}_{\ell m}^{E}(\theta,\phi)=0$ for all $\ell$ and $m$. It follows that

$$\mathbf{e}^{\mathrm{T}}(\theta,\phi)\mathbf{C}_{\mathbf{B}}(\theta,\phi)\mathbf{e}(\theta,\phi)=0 \tag{3.35}$$

$$\mathbf{b}^{\mathrm{T}}(\theta,\phi)\mathbf{C}_{\mathbf{E}}(\theta,\phi)\mathbf{e}(\theta,\phi)=0 \tag{3.36}$$

for any choice of power spectrum.

In an alternative view, $E$-mode and $B$-mode can be related to the second derivatives of $Q$ and $U$. First, we define the spin-raising and spin-lowering derivative operators

$$ðf=-\sin^{s}\theta\left[\frac{\partial}{\partial\theta}+\frac{i}{\sin\theta}\frac{\partial}{\partial\phi}\right]\left(\sin^{-s}\theta\, f\right) \tag{3.37}$$

$$\bar{ð}f=-\sin^{-s}\theta\left[\frac{\partial}{\partial\theta}-\frac{i}{\sin\theta}\frac{\partial}{\partial\phi}\right]\left(\sin^{s}\theta\, f\right) \tag{3.38}$$

where $s$ is the spin weight of $f$. The operators generate the spin-weighted spherical harmonics from the ordinary spherical harmonics by

$$ð\left[{}_sY_{\ell m}(\theta,\phi)\right]=\sqrt{\ell(\ell+1)-s(s+1)}\,{}_{s+1}Y_{\ell m} \tag{3.39}$$

$$\bar{ð}\left[{}_sY_{\ell m}(\theta,\phi)\right]=-\sqrt{\ell(\ell+1)-s(s-1)}\,{}_{s-1}Y_{\ell m} \tag{3.40}$$

The $E$-mode and $B$-mode spherical harmonics are associated with a pair of second derivatives

$$\mathbf{D_E}\left[{}_0Y_{\ell m}(\theta,\phi)\right] = \frac{1}{2}\begin{pmatrix} \eth^2 + \bar{\eth}^2 \\ \\ -i(\eth^2 - \bar{\eth}^2) \end{pmatrix} {}_0Y_{\ell m}(\theta,\phi) = \sqrt{\frac{(\ell+2)!}{(\ell-2)!}}\,\mathbf{Y}^E_{\ell m}(\theta,\phi) \tag{3.41}$$

$$\mathbf{D_B}\left[{}_0Y_{\ell m}(\theta,\phi)\right] = \frac{1}{2}\begin{pmatrix} i(\eth^2 - \bar{\eth}^2) \\ \\ \eth^2 + \bar{\eth}^2 \end{pmatrix} {}_0Y_{\ell m}(\theta,\phi) = \sqrt{\frac{(\ell+2)!}{(\ell-2)!}}\,\mathbf{Y}^B_{\ell m}(\theta,\phi) \tag{3.42}$$

$$\mathbf{P}(\theta,\phi) = -\sum_{\ell m}\sqrt{\frac{(\ell-2)!}{(\ell+2)!}}\left(a^E_{\ell m}\,\mathbf{D_E}[{}_0Y_{\ell m}(\theta,\phi)] + a^B_{\ell m}\,\mathbf{D_B}[{}_0Y_{\ell m}(\theta,\phi)]\right) \tag{3.43}$$

The orthogonality relations are

$$\mathbf{D_E}^\dagger\mathbf{D_E}\left[{}_0Y_{\ell m}(\theta,\phi)\right] = \mathbf{D_B}^\dagger\mathbf{D_B}\left[{}_0Y_{\ell m}(\theta,\phi)\right] = \frac{(\ell+2)!}{(\ell-2)!}\,{}_0Y_{\ell m}(\theta,\phi) \tag{3.44}$$

$$\mathbf{D_E}^\dagger\mathbf{D_B}\left[{}_0Y_{\ell m}(\theta,\phi)\right] = 0 \tag{3.45}$$

Bluer versions of the $E$-mode and $B$-mode maps are extracted by differentiation

$$\mathbf{D_E}^\dagger\mathbf{P}(\theta,\phi) = \sum_{\ell m}\sqrt{\frac{(\ell+2)!}{(\ell-2)!}}a^E_{\ell m}\,{}_0Y_{\ell m}(\theta,\phi) \tag{3.46}$$

$$\mathbf{D_B}^\dagger\mathbf{P}(\theta,\phi) = \sum_{\ell m}\sqrt{\frac{(\ell+2)!}{(\ell-2)!}}a^B_{\ell m}\,{}_0Y_{\ell m}(\theta,\phi) \tag{3.47}$$

The above equations are exact on the whole sphere. In practice, a ground-based telescope typically targets a limited field, which may be approximated as flat. In the flat-sky approximation, the derivatives are

$$\eth f = -(\partial_x + i\partial_y)f \tag{3.48}$$

$$\bar{\eth} f = -(\partial_x - i\partial_y)f \tag{3.49}$$

$$\mathbf{D_E} = \begin{pmatrix} \partial_x^2 - \partial_y^2 \\ \\ 2\partial_x\partial_y \end{pmatrix} \tag{3.50}$$

$$\mathbf{D_E} = \begin{pmatrix} -2\partial_x\partial_y \\ \\ \partial_x^2 - \partial_y^2 \end{pmatrix} \tag{3.51}$$

Using the approximation $\sqrt{\frac{(\ell-2)!}{(\ell+2)!}} \approx \frac{1}{\ell^2}$, we find that the polarization vector in the Fourier domain is

$$\hat{\mathbf{P}}(\ell_x, \ell_y) = \frac{1}{\ell^2} \begin{pmatrix} \ell_x^2 - \ell_y^2 \\ \\ 2\ell_x\ell_y \end{pmatrix} \hat{E}(\ell_x, \ell_y) + \frac{1}{\ell^2} \begin{pmatrix} -2\ell_x\ell_y \\ \\ \ell_x^2 - \ell_y^2 \end{pmatrix} \hat{B}(\ell_x, \ell_y) \tag{3.52}$$

$$= \begin{pmatrix} \cos(2\chi) & -\sin(2\chi) \\ \\ \sin(2\chi) & \cos(2\chi) \end{pmatrix} \begin{pmatrix} \hat{E}(\ell_x, \ell_y) \\ \\ \hat{B}(\ell_x, \ell_y) \end{pmatrix} \tag{3.53}$$

where $\chi$ is an angle in the Fourier plane. Since the transformation depends only on $\chi$, it is more common to use a polar coordinate system with angle $\chi$ and modulus $\ell = \sqrt{\ell_x^2 + \ell_y^2}$. We also take $\chi \to -\chi$ and $U \to -U$ to convert to the IAU convention.

$$\hat{\mathbf{P}}_{\text{IAU}}(\ell, \chi) = \begin{pmatrix} \cos(2\chi) & \sin(2\chi) \\ \\ \sin(2\chi) & -\cos(2\chi) \end{pmatrix} \begin{pmatrix} \hat{E}(\ell, \chi) \\ \\ \hat{B}(\ell, \chi) \end{pmatrix} \tag{3.54}$$

Equivalently, the the matrix can be kept as a rotation, and the sign of $B$ reversed between the two conventions. Like the full sky case, it is possible to extract the components of $Q$ and $U$ coming only from $E$ or $B$ by setting them to zero in the above equation and returning to real space. In this form, it is easy to see that the transformation from $E$ and $B$ to $Q$ and $U$ is invertible, with

$$\begin{pmatrix} \hat{E}(\ell, \chi) \\ \\ \hat{B}(\ell, \chi) \end{pmatrix} = \begin{pmatrix} \cos(2\chi) & \sin(2\chi) \\ \\ \sin(2\chi) & -\cos(2\chi) \end{pmatrix} \hat{\mathbf{P}}_{\text{IAU}}(\ell, \chi) \tag{3.55}$$

The remainder of this thesis uses the IAU convention.

## 3.5 Mode mixing and ambiguity

The flat sky approximation is useful only when the survey is over a limited amount of sky. The cut relative the full sky is represented by the multiplication of the survey by a window function. In the Fourier domain, this is a convolution

$$\tilde{\mathbf{P}}(\ell,\chi) = \int \hat{W}(\boldsymbol{\ell}-\boldsymbol{\ell}')\hat{\mathbf{P}}(\ell',\chi')d^2\boldsymbol{\ell}' \tag{3.56}$$

If the observed polarization vector $\tilde{\mathbf{P}}(\ell,\chi)$ is inverted as if there were no window function applied, then the observed $E$-mode and $B$-mode are

$$\begin{pmatrix}\tilde{E}(\ell,\chi)\\ \tilde{B}(\ell,\chi)\end{pmatrix} = \int \hat{W}(\boldsymbol{\ell}-\boldsymbol{\ell}') \begin{pmatrix}\cos(2\chi) & \sin(2\chi)\\ \sin(2\chi) & -\cos(2\chi)\end{pmatrix} \begin{pmatrix}\cos(2\chi') & \sin(2\chi')\\ \sin(2\chi') & -\cos(2\chi')\end{pmatrix} \begin{pmatrix}\hat{E}(\ell',\chi')\\ \hat{B}(\ell',\chi')\end{pmatrix} d^2\boldsymbol{\ell}' \tag{3.57}$$

A realistic survey with apodization has $\hat{W}(\boldsymbol{\ell}-\boldsymbol{\ell}') \neq \delta(\boldsymbol{\ell}-\boldsymbol{\ell}')$, in which case the modes can mix. The off-diagonal terms are generally nonzero, and for an $E$-mode-dominated sky the $E$-to-$B$ leakage term

$$\tilde{B}_{\mathrm{leak}} = \int \hat{W}(\boldsymbol{\ell}-\boldsymbol{\ell}')\left[\sin(2\chi)\cos(2\chi') - \cos(2\chi)\sin(2\chi')\right]\hat{E}(\ell',\chi')d^2\boldsymbol{\ell}' \tag{3.58}$$

is a significant contributor to false $B$-mode signal. The window function is only one way to create ambiguous modes. Any linear operation to $\mathbf{P}(\theta,\phi)$ is a convolution in the Fourier domain with $\hat{\mathbf{P}}(\ell,\chi)$, which can further contribute to the off-diagonal terms.

## 3.6 Observation matrix

A more general vector accounts for the temperature maps and the pixelization. If the maps have $N$ pixels, then the three maps are represented by a total observed map vector of length $3N$.

$$\tilde{\mathbf{m}} = \begin{pmatrix}\overline{T}_1 & \dots & \overline{T}_N & \overline{Q}_1 & \dots & \overline{Q}_N & \overline{U}_1 & \dots & \overline{U}_N\end{pmatrix}^{\mathrm{T}} \tag{3.59}$$

The observed map vector is a filtered version of the true sky map vector $\mathbf{m}$. The finite angular resolution imposed by the BICEP2/*Keck Array* optics acts as a low pass filter. A pointing matrix takes the beam-smoothed sky and turns it into time-ordered data. The BICEP2/*Keck Array* time streams are high pass filtered by a third order polynomial over the length of a half scan to reduce atmospheric contamination. Ground subtraction filters signals that are azimuthally fixed over the duration of the scanset. Deprojection filters pair-differenced signals that correlate with the temperature signal as measured by *Planck* 143 GHz and its derivatives to prevent temperature to polarization leakage induced by beam effects. The filtered, weighted time streams are accumulated into maps by the linear procedure detailed above. Since all of these operations are linear, the entire observation is represented by a matrix operation.

In parallel with the construction of the detector pair maps and their accumulation we construct pixel-pixel matrices which track how every true sky pixel maps into the pixels of the final map due to the various filtering operations. We take "true sky pixel maps" to be Nside = 512 `HEALPix` maps, whose pixel size ($\sim 0.1°$ on a side) is smaller than our observed map pixels ($0.25°$). The act of simulating our various filtering operations becomes a simple matrix multiplication:

$$\tilde{\mathbf{m}} = \mathbf{R}\mathbf{m} \tag{3.60}$$

Next, we "observe" an Nside = 512 `HEALPix` theoretical covariance matrix (constructed following Appendix A of M. Tegmark and A. de Oliveira-Costa [86]), $\mathbf{C}$, with $\mathbf{R}$:

$$\tilde{\mathbf{C}} = \mathbf{R}\mathbf{C}\mathbf{R}^{\mathrm{T}} \tag{3.61}$$

The construction of $\mathbf{R}$ from all of the pointing and filtering operations is discussed at length in J. E. Tolan's thesis [87].

## 3.7 Purification matrix

We form $\tilde{\mathbf{C}}$ for both $E$-mode and $B$-mode covariances. These matrices provide the pixel-pixel covariance for $E$ modes and $B$ modes in the same observed space as the real data. However, the matrix $\mathbf{R}$ has made the two spaces nonorthogonal and introduced ambiguous modes, i.e., modes in the observed space which are superpositions of either $E$ modes or $B$ modes on the sky.

To isolate the pure $B$ modes we adapt the method described in E. F. Bunn *et al.* [17]. We solve a generalized eigenvalue problem:

$$(\tilde{\mathbf{C}}_{\mathbf{E}} + \sigma^2 \mathbf{I})\mathbf{e} = \lambda_{\mathbf{e}} (\tilde{\mathbf{C}}_{\mathbf{B}} + \sigma^2 \mathbf{I})\mathbf{e} \tag{3.62}$$

$$(\tilde{\mathbf{C}}_{\mathbf{B}} + \sigma^2 \mathbf{I})\mathbf{b} = \lambda_{\mathbf{b}} (\tilde{\mathbf{C}}_{\mathbf{E}} + \sigma^2 \mathbf{I})\mathbf{b} \tag{3.63}$$

where $\mathbf{e}$ and $\mathbf{b}$ are pure $E$-mode and pure $B$-mode eigenvectors and $\sigma^2$ is a small number introduced to regularize the problem. This system has the property that $\lambda_{\mathbf{e}} = \frac{1}{\lambda_{\mathbf{b}}}$. The eigenvectors with $\lambda_{\mathbf{e}} > 1$ are the most significant $E$-mode eigenvectors, and those with $\lambda_{\mathbf{b}} > 1$ are the most significant $B$-mode eigenvectors. The eigenvectors with $\lambda_{\mathbf{e}} = \lambda_{\mathbf{b}} = 1$ are the ambiguous modes. By selecting modes corresponding to the largest eigenvalues $\lambda_{\mathbf{e}} \gg 1$ or $\lambda_{\mathbf{b}} \gg 1$, we can find the orthogonal $E$-mode and $B$-mode subspaces that are also orthogonal to the ambiguous modes. The covariance matrices are calculated using steeply reddened input spectra ($\sim \ell^{-2}$) so that the eigenmodes are separated in angular scale, making it easy to select modes up to a cutoff $\ell$ set by the instrument resolution.

The matrix purification operators are a sum of outer products of the selected eigenmodes; it projects an input map onto the pure $E$-mode or pure $B$-mode subspace:

$$\mathbf{\Pi}_{\mathbf{e}} = \sum_i \mathbf{e}_i \mathbf{e}_i^{\mathrm{T}} \tag{3.64}$$

$$\mathbf{\Pi}_{\mathbf{b}} = \sum_i \mathbf{b}_i \mathbf{b}_i^{\mathrm{T}} \tag{3.65}$$

They can be applied to any real or simulated map vector and return purified vectors, which contain only signal coming unambiguously from $E$-mode or $B$-mode components on the true sky:

$$\tilde{\mathbf{m}}_{\mathbf{e}} = \mathbf{\Pi}_{\mathbf{b}}\tilde{\mathbf{m}} \tag{3.66}$$

$$\tilde{\mathbf{m}}_{\mathbf{b}} = \mathbf{\Pi}_{\mathbf{b}}\tilde{\mathbf{m}} \tag{3.67}$$

Additional information on the construction of the purification matrix and its comparison to other methods is given in J. E. Tolan's thesis [87].

## 3.8 Cross maps

Consider a pair of real-valued functions $f(x)$ and $g(x)$, which can be maps, with Fourier conjugates $\hat{f}(k)$ and $\hat{g}(k)$. Since $\hat{f}(-k) = \hat{f}^*(k)$ and $\hat{g}(-k) = \hat{g}^*(k)$, an average over positive and negative wavenumber retains only the real part

$$\frac{\hat{f}(k)\hat{g}^*(k) + \hat{f}(-k)\hat{g}^*(-k)}{2} = \mathrm{Re}\left[\hat{f}(k)\hat{g}^*(k)\right] \tag{3.68}$$

Unlike an autospectrum, the term $\mathrm{Re}\left[\hat{f}(k)\hat{g}^*(k)\right]$ can go negative if there are anticorrelated modes. So there does not in general exist a map with this autospectrum. We can, however, define a pair of functions representing the correlated and anticorrelated modes. The correlated part is

$$h_+(x) = \mathcal{F}^{-1}\left[\frac{\mathrm{sgn}\,(\hat{f}(k)) + \mathrm{sgn}\,(\hat{g}(k))}{2}\sqrt{|\hat{f}(k)\hat{g}^*(k)|}\right] \tag{3.69}$$

The anticorrelated part, analogous to a jackknife, is the correlated part of $f(x)$ with $-g(x)$, which is

$$h_-(x) = \mathcal{F}^{-1}\left[\frac{\mathrm{sgn}\,(\hat{f}(k)) - \mathrm{sgn}\,(\hat{g}(k))}{2}\sqrt{|\hat{f}(k)\hat{g}^*(k)|}\right] \tag{3.70}$$

Both $h_+(x)$ and $h_-(x)$ are real. They have power spectra

$$|\hat{h}_+(k)|^2 = \frac{1}{2}\left(|\hat{f}(k)\hat{g}^*(k)| + \mathrm{Re}\left[\hat{f}(k)\hat{g}^*(k)\right]\right) \tag{3.71}$$

$$|\hat{h}_-(k)|^2 = \frac{1}{2}\left(|\hat{f}(k)\hat{g}^*(k)| - \mathrm{Re}\left[\hat{f}(k)\hat{g}^*(k)\right]\right) \tag{3.72}$$

so that the cross-spectrum is recovered by

$$|\hat{h}_+(k)|^2 - |\hat{h}_-(k)|^2 = \mathrm{Re}\left[\hat{f}(k)\hat{g}^*(k)\right] \tag{3.73}$$

Compare the power spectrum of a simple map average:

$$\left|\frac{\hat{f}(k)+\hat{g}(k)}{2}\right|^2 = \frac{1}{2}\left(\frac{|\hat{f}(k)|^2+|\hat{g}(k)|^2}{2} + \mathrm{Re}\left[\hat{f}(k)\hat{g}^*(k)\right]\right) \geq |\hat{h}_+(k)|^2 \tag{3.74}$$

where the inequality asserts that the arithmetic mean is always greater than or equal to the geometric mean.

Unlike an arithmetic mean of maps, the cross map $h_+(x)$ is related nonlinearly to $f(x)$ and $g(x)$. For this reason, cross maps are for visual representation of the reduced-noise, correlated components of maps only and should generally be avoided in high level analysis. If $h_+(x)$ is to be low pass filtered, $f(x)$ and $g(x)$ should stay unfiltered during the combination to prevent aliasing. It is recommended that they also be weighted by a common mask $w(x)$. Cross maps should be computed for $E$ and $B$ directly instead of $Q$ and $U$ transformed to $E$ and $B$.

# Chapter 4

# Simulations and map noise

This chapter presents the formalism for the BICEP2/*Keck Array* signal and noise simulation. We briefly review the MASTER algorithm [35] commonly used to analyze CMB data sets in Section 4.1. The bandpower window functions derived from simulations of a single multipole are described in Section 4.2 with additional plots in Appendix B. The simulations of lensed-$\Lambda$CDM signal is mentioned in Section 4.3. The full description of the sign-flip noise model, complete with the accumulation of the noise covariance matrix, is presented in Sections 4.4–4.6, and an attempt at visualization of the noise correlation is given in Section 4.7. Technical details of how to model the noise distribution in cross-spectra is given in Sections 4.8 and 4.9.

## 4.1 Signal suppression and noise bias

The 1D power spectra "pseudo-$C_\ell$" are the averages of $|\hat{E}(\ell,\chi)|^2$, $|\hat{B}(\ell,\chi)|^2$, and $\hat{E}(\ell,\chi)\hat{B}(\ell,\chi)^*$ around the circles of constant $\ell$, or in practice the averages within annuli that are the width of a desired $\ell$ bin. It is more common to report $\mathcal{D}_\ell = \frac{\ell(\ell+1)C_\ell}{2\pi}$. If the bin centers are some fiducial, equispaced set $\ell'$, then the observed bandpowers are the annular averages $\mathcal{D}^{\text{obs}}_{\ell'}$.

Theoretical values of $\mathcal{D}_\ell$ on the sphere do not correspond directly to $\mathcal{D}^{\text{obs}}_{\ell'}$ for a realistic experiment. The linear filtering, summarized by the observation matrix, as well as the limited sky survey area and apodization, can mix and suppress modes. In order to compare the theoretical values to the observed ones, we need to find how the modes mix. For all of the bins there is a set of functions $F_{\ell,\ell'}$ that mix the modes and suppress the power as $\mathcal{D}^{\text{obs}}_{\ell'} = F_{\ell,\ell'}\mathcal{D}_\ell$. If $F_{\ell,\ell'}$ is normalized to have unit area, then it is called the bandpower window function. The normalization factor $S_{\ell'} = \sum_\ell F_{\ell,\ell'}$ is called the suppression factor. Note that the suppression factor is partially degenerate with the absolute calibration of the experiment.

A measured map contains additive noise, which in the Fourier domain can be expressed as $\hat{s}(k) + \hat{n}(k)$. If the signal and noise are uncorrelated, then the expectation value of its 2D autospectrum is

$$\left\langle |\hat{s} + \hat{n}|^2 \right\rangle = \left\langle |\hat{s}|^2 \right\rangle + \left\langle |\hat{n}|^2 \right\rangle \tag{4.1}$$

Since $\left\langle |\hat{n}|^2 \right\rangle > 0$ for any positive amount of noise, the autospectrum always has a positive bias. The signal and noise average over the annuli independently such that $\left\langle \mathcal{D}_{\ell'}^{s+n} \right\rangle = \langle \mathcal{D}_{\ell'}^{s} \rangle + \langle \mathcal{D}_{\ell'}^{n} \rangle$. An unbiased estimate of the signal autospectrum is therefore

$$\mathcal{D}_{\ell'} = \frac{\mathcal{D}_{\ell'}^{\mathrm{obs}} - \langle \mathcal{D}_{\ell'}^{n} \rangle}{S_{\ell'}} \tag{4.2}$$

Arbitrary theoretical $\mathcal{D}_\ell$ can be compared to the reported $\mathcal{D}_{\ell'}$ by taking a weighted sum of $\mathcal{D}_\ell$ with respect to the bandpower window functions. (Although the set of $\ell'$ is chosen to be the centers of the annuli, the functions $F_{\ell,\ell'}$ may be centered slightly away from the original $\ell'$. The reported band centers $\ell'_{\mathrm{eff}}$ are instead the average values of $\ell$ with respect to the bandpower window functions.)

BICEP2/*Keck Array* estimates its bandpowers using a variant of the MASTER algorithm [35]. The procedure is to calculate 499 noise simulations to determine the bias $\langle \mathcal{D}_{\ell'}^{n} \rangle$. If a good estimate of $S_{\ell'}$ is available, then $\mathcal{D}_{\ell'}$ can be estimated for all 499 noise simulations as well as for the real data. Since the real data lie outside the noise-only distribution, $\mathcal{D}_{\ell'}$ is also estimated for all of the 499 signal+noise simulations. The set of 499 simulations is called a “simset”.

## 4.2 Single multipole simulations

For Gaussian beams, the finite angular resolution isotropically suppresses the power, approximated as $e^{-\ell(\ell+1)\sigma^2}$. A more accurate beam window function than the Gaussian approximation is inferred from far field beam maps of the BSNS, as described in Section 2.10 and BK–IV. The polynomial filtering, ground

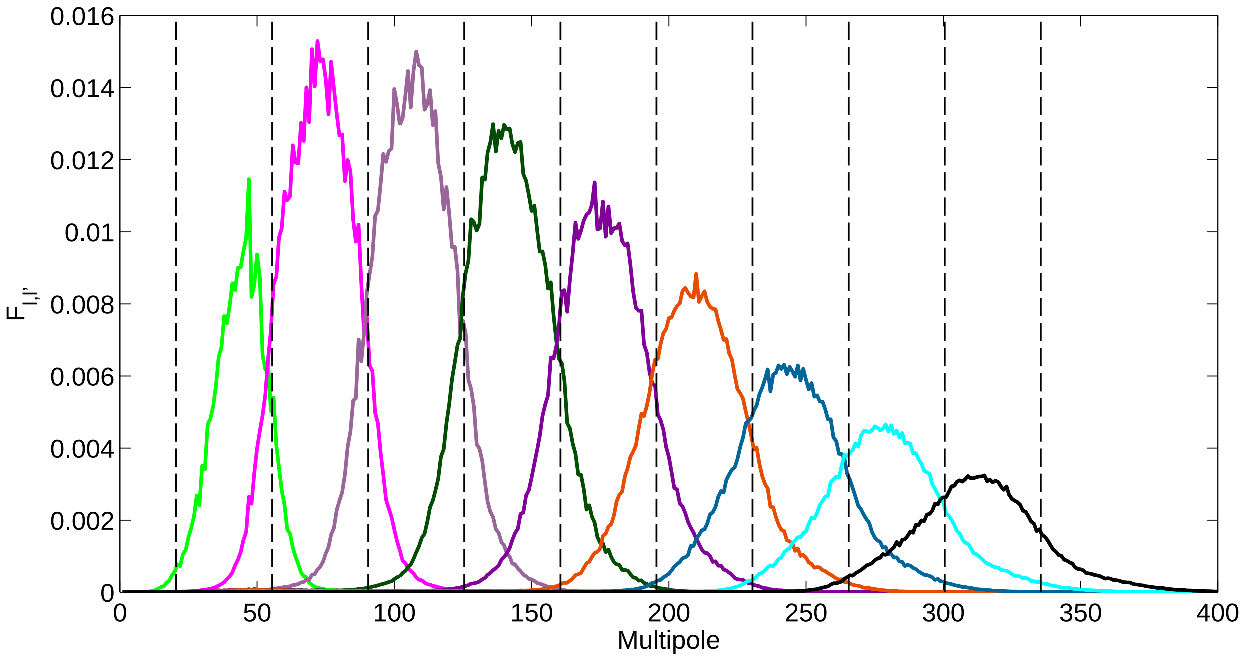

Figure 4.1: $F_{\ell,\ell'}$ for $\mathcal{D}_\ell^{BB}$ evaluated for Bicep2 using simulations at a single multipole containing no $E$-mode power and processed through the analysis pipeline, including matrix purification. The dashed, vertical lines are the $\ell$ bin edges. Suppression at low $\ell$ is dominated by the polynomial filtering and ground subtraction. Suppression at high $\ell$ is dominated by the $\sim 0.5°$ FWHM beams. The corresponding functions for the other power spectra look qualitatively similar.

subtraction and deprojection operations are applied to the azimuth scans, which results in anisotropic suppression. The main effect of the anisotropic filters is suppression along the $k_x = 0$ line in the 2D Fourier plane. The purification matrix is also a kind of filter applied to the maps.

Since the observation and purification matrices capture all of the effects of filtering, they can be used to determine $F_{\ell,\ell'}$. The calculation is done one $\ell$ at a time. Bicep2/*Keck Array* generates 50 simulations of sky maps with $\mathcal{D}_\ell = 1$ in a single $\ell$ from 2 to 700 and $\mathcal{D}_\ell = 0$ in all other multipoles. The simulations are processed with the observation and purification matrices to suppress the single mode. The response in each of the observed bins $\mathcal{D}_{\ell'}^{\mathrm{obs}}$ is averaged over the simulations, and the result is $F_{\ell,\ell'}$.

The functions $F_{\ell,\ell'}$ for $\mathcal{D}_\ell^{BB}$ are shown in Figure 4.1. Although $F_{\ell,\ell'}$ relates the theoretical 1D power spectra to the observed power spectra, a more general relation exists between the 2D angular power spectra prior to the annular averaging. The filtering of the azimuth scans suppresses modes preferentially along $|\ell_{\mathrm{ra}}| \lesssim 40$ in the Fourier plane. The 2D bandpower window functions of all nine $\ell$ bins are shown in

Appendix B and illustrate the effect of the anisotropic filtering.

## 4.3 Signal simulations

The CMB temperature power spectrum is simulated on the sphere by $a^T_{\ell m} = \sqrt{C^{TT}_\ell} n_{\ell m}$, where $C^{TT}_\ell$ are the best fit values from *Planck* and $n_{\ell m}$ are standard complex normal numbers, generated pseudorandomly. The condition $n_{\ell -m} = (-1)^m n^*_{\ell m}$ assures that the map is real-valued. It is clear that the $a^T_{\ell m}$ are Gaussian because the $n_{\ell m}$ are Gaussian, and the expectation of the simulations is the theoretical value $\left\langle |a^T_{\ell m}|^2 \right\rangle = C^{TT}_\ell$. The temperature signal within the Bicep2/*Keck Array* field is very well measured by other experiments, including *Planck*. The sample variance from observing only a small part of the sky is so large that Bicep2/*Keck Array* does not constrain cosmological parameters with temperature maps.

The deprojection templates are derived from the *Planck* temperature maps instead of Bicep2/*Keck Array*'s own temperature maps to preserve the linearity of the analysis pipeline. The effect of residual noise in the *Planck* templates is very small. Since the filtering derived from a known, external temperature map is applied to an unknown polarization map, it is important that the simulated polarization signal preserve any expected correlation with the temperature. In ΛCDM, temperature and $E$-mode signals are highly correlated. The constrained $E$-mode simulations are the maps coming from

$$a^E_{\ell m} = \frac{C^{TE}_\ell}{C^{TT}_\ell} a^T_{\ell m} + \sqrt{C^{EE}_\ell - \frac{(C^{TE}_\ell)^2}{C^{TT}_\ell}} n_{\ell m} \tag{4.3}$$

where all of $C^{TT}_\ell$, $C^{TE}_\ell$, and $C^{EE}_\ell$ are the best fit values from *Planck* and, importantly, $a^T_{\ell m}$ are the actual sky measurements from *Planck* as reported in the Needlet Internal Linear Combination (NILC) temperature map. It is again clear that the $a^E_{\ell m}$ are Gaussian to the extent that the NILC $a^T_{\ell m}$ are, and the expectation of the simulations is $\left\langle |a^E_{\ell m}|^2 \right\rangle = C^{EE}_\ell$.

The lensing potential is not as well constrained in the Bicep2/*Keck Array* field. Lensing is the dominant contribution to the $B$-mode power spectrum for $\ell > 200$. Its effect on temperature and $E$-mode maps is subdominant, however, to the rest of the unlensed ΛCDM model. Lensing introduces some non-Gaussianity in the observed NILC $a^T_{\ell m}$. The constrained $E$-mode simulations are treated as if the input temperature map were an unlensed field. Lensing $B$-mode maps are simulated by taking the $E$-mode simulations and deflecting them using the `LensPix` package [46]. J. E. Tolan's thesis [87] discusses when lensing is assumed present or absent through the steps of the simulation pipeline.

The $T/E/B$ maps are converted to $T/Q/U$ maps. They are convolved with the beam shape from the BSNS. They are then converted into simulated time streams that assume the pointing information and deck angle of the instrument and accumulated into maps, or they are simply multiplied by the observation matrix.

## 4.4 Noise models

The BICEP1 noise model as described in the BICEP1 instrument paper [85] involved generating noise at the time stream level. The detector-detector noise covariance matrix was estimated in twelve frequency bands over the duration of a scanset. The covariance matrices were factored by Cholesky decomposition. The factors were multiplied by normally distributed pseudorandom numbers and inverse Fourier transformed back to the time domain to generate simulated noise time streams. The noise time streams were filtered and processed through the analysis pipeline like real data. Owing to the large increase in the number of detectors for BICEP2/*Keck Array*, this method was found to be too computationally expensive.

The BICEP2/*Keck Array* noise model is instead based on fluctuations in the maps. This is done in two ways. The first is to accumulate a map pixel-pixel noise covariance matrix. If all of the noise in the maps is accurately described by a multivariate Gaussian distribution, then all of the information about the noise is contained in the noise covariance matrix. It compares in form to the signal covariance and is useful as a data product for public release. The data in the $k$th scanset are accumulated into map vectors $\tilde{\mathbf{m}}_k$, which are compared to the final map vector $\tilde{\mathbf{m}}$ to get deviations $\delta\tilde{\mathbf{m}}_k = \tilde{\mathbf{m}}_k - \tilde{\mathbf{m}}$. All of the filtering operations except matrix purification are already inherent in the deviations. The noise covariance between map pixel $i$ and map pixel $j$ is the weighted accumulation of $\delta\tilde{m}_{ik}\delta\tilde{m}_{jk}$ over the scansets. Like the time stream-based model, the map pixel-pixel noise covariance matrix is factored by Cholesky decomposition. Factoring the

BICEP2/*Keck Array* noise covariance matrix is computationally expensive but only needs to be done once. Multiplying the factor by normally distributed pseudorandom numbers quickly generates simulated final map vectors.

The second map-based noise model is sign-flip noise simulations. (Perhaps "pseudo-model" is a better name because the simulations are a linear combination of the real data.) BICEP2/*Keck Array* has opted for a standard noise simset containing 499 sign-flip noise simulations for the analysis in its first data release. The sign-flip procedure is to calculate the deviation maps for every scanset, then pseudorandomly choose either to leave $\delta\tilde{\mathbf{m}}_k$ alone or to flip its sign by $\delta\tilde{\mathbf{m}}_k \to -\delta\tilde{\mathbf{m}}_k$. Since the covariance matrix only depends on the products of pairs of deviations, it is insensitive to whether the sign has been flipped. A sign-flip noise simulation is the weighted accumulation of the $\varepsilon_k\delta\tilde{\mathbf{m}}_k$ where $\varepsilon_k$ is the assignment of either $+1$ or $-1$. The sign-flip noise simulations use less memory at any given step because the noise covariance is never computed. Although the number of possible sign-flip sequences is finite, it grows exponentially with the number of scansets. The sign-flip sequences are chosen to balance the weights to avoid artificially extreme values. The number of equal-weight sign-flip sequences is much larger than the benchmark of 499 simulations typically used for BICEP2/*Keck Array*.

In either the accumulation of the pixel-pixel noise covariance matrix or the assignment of sign-flip sequences to the scansets, it is assumed that correlated noise does not persist across timescales longer than a scanset. The main contributor to noise that is correlated over long timescales is the atmosphere. The atmosphere is largely unpolarized at these frequencies, and the typical coherence time for atmospheric noise is shorter than the $\sim 50$ minutes of a scanset. Moreover, any remaining noise correlation across long timescales is heavily suppressed by the time domain filtering.

Averaging together cross-spectra between equally weighted data splits is another way of eliminating noise bias from the power spectrum estimate. We show here that this method is mathematically equivalent to subtracting the average autospectrum of the sign-flip noise simset. Let $f(x)$ be a real-valued function that is the average of noisy data. Consider a data split $n$ to be a pair of real-valued functions $f_{n,\pm}(x)$ that are averages of separate halves of the underlying data, where each half receives equal weight when averaged into

$f(x)$. They can be maps consisting of the average of all scansets assigned +1 by the equal-weight sign-flip procedure and the average of the others assigned −1 (but before actually applying the sign flip). The map as averaged over the entire data set is recovered by $f(x) = (f_{n,+}(x) + f_{n,-}(x))/2$ for all splits because the halves are equally weighted. Likewise, the $n$th sign-flip noise simulation is $(f_{n,+}(x) - f_{n,-}(x))/2$. The average of the $N = 499$ autospectra of the noise simset is used as an estimate of the noise bias as in Equations 4.1 and 4.2. An estimate of the 2D power spectrum using the data splits is

$$\begin{aligned} |\hat{f}(k)|^2 - \frac{1}{N}\sum_{n=1}^{N}\left|\frac{\hat{f}_{n,+}(k) - \hat{f}_{n,-}(k)}{2}\right|^2 &= \frac{1}{N}\sum_{n=1}^{N}\left(\left|\frac{\hat{f}_{n,+}(k) + \hat{f}_{n,-}(k)}{2}\right|^2 - \left|\frac{\hat{f}_{n,+}(k) - \hat{f}_{n,-}(k)}{2}\right|^2\right) \\ &= \frac{1}{N}\sum_{n=1}^{N}\mathrm{Re}\,[\hat{f}_{n,+}(k)\hat{f}^*_{n,-}(k)] \end{aligned} \tag{4.4}$$

The term $\hat{f}_{n,+}(k)\hat{f}^*_{n,-}(k)$ is the 2D cross-spectrum between the two halves of the data split. As noted in Equation 3.68, only the real part of the 2D power spectrum contributes to the 1D power spectrum for a real-valued map. Thus the 1D power spectrum estimates are the same.

## 4.5 Deviations

The values taken by map pixel $i$ in the $k$th scanset or phase are denoted $T_{ik}$, $Q_{ik}$, and $U_{ik}$. The deviation of a pixel's value for a given scanset or phase is the difference of these values from the final, fully averaged maps. The sample noise covariance matrix is the weighted sum of the outer product of the deviations of all of the map pixels in the individual scanset or phase maps.

We wish to modify the detector pair sums and differences so that they accumulate the covariance matrix. In a given phase, the weighted deviation of the pair sum is

$$\delta x_{ik} = w_{ik}(T_{ik} - \overline{T}_i) = x_{ik} - w_{ik}\overline{T}_i \tag{4.5}$$

The weighted deviation of the pair difference involves rotating $\overline{Q}_i$ and $\overline{U}_i$ to a predicted pair difference signal at the specific deck angle of the scanset.

$$\begin{aligned}\begin{pmatrix}\delta y_{ik} \\ \delta z_{ik}\end{pmatrix} &= \frac{1}{4}w_{ik}\begin{pmatrix}\alpha_{ik}^2 & \alpha_{ik}\beta_{ik} \\ \alpha_{ik}\beta_{ik} & \beta_{ik}^2\end{pmatrix}\left[\begin{pmatrix}Q_{ik} \\ U_{ik}\end{pmatrix} - \begin{pmatrix}\overline{Q}_i \\ \overline{U}_i\end{pmatrix}\right] \\ &= \begin{pmatrix}y_{ik} \\ z_{ik}\end{pmatrix} - \frac{1}{4}w_{ik}\begin{pmatrix}\alpha_{ik}^2 & \alpha_{ik}\beta_{ik} \\ \alpha_{ik}\beta_{ik} & \beta_{ik}^2\end{pmatrix}\begin{pmatrix}\overline{Q}_i \\ \overline{U}_i\end{pmatrix}\end{aligned} \tag{4.6}$$

## 4.6 Noise covariance blocks

The noise covariance matrix **N** exhibits a block structure, shown below.

| | | |
|---|---|---|
| $N_{ij}^{TT}$ | $N_{ij}^{TQ}$ | $N_{ij}^{TU}$ |
| $N_{ij}^{QT}$ | $N_{ij}^{QQ}$ | $N_{ij}^{QU}$ |
| $N_{ij}^{UT}$ | $N_{ij}^{UQ}$ | $N_{ij}^{UU}$ |

Only the blocks in the upper right triangle need to be computed because the lower triangle is obtained by the symmetry $N_{ij}^{QT} = N_{ji}^{TQ}$, $N_{ij}^{UT} = N_{ji}^{TU}$, and $N_{ij}^{UQ} = N_{ji}^{QU}$. Table A.2 is a key for the noise accumulation quantities in the Matlab analysis pipeline. We allow the weights for temperature $w^T$ and weights for polarization $w^P$ to be possibly different. The blocks of the noise covariance matrix are to be calculated using the weighted deviations as follows:

$$N_{ij}^{TT} = \frac{\sum_k \delta x_{ik}\delta x_{jk}}{\sum_k w_{ik}^T \sum w_{jk}^T} \tag{4.7}$$

$$N_{ij}^{TQ} = \frac{e_j \sum_k \delta x_{ik}\delta y_{jk} + f_j \sum_k \delta x_{ik}\delta z_{jk}}{\sum_k w_{ik}^T \sum_k w_{jk}^P} \tag{4.8}$$

$$N_{ij}^{TU} = \frac{f_j \sum_k \delta x_{ik}\delta y_{jk} + g_j \sum_k \delta x_{ik}\delta y_{jk}}{\sum_k w_{ik}^T \sum_k w_{jk}^P} \tag{4.9}$$

$$N_{ij}^{QQ} = \frac{e_i e_j \sum_k \delta y_{ik}\delta y_{jk} + e_i f_j \sum_k \delta y_{ik}\delta z_{jk} + f_i e_j \sum_k \delta z_{ik}\delta y_{jk} + f_i f_j \sum_k \delta z_{ik}\delta z_{jk}}{\sum_k w_{ik}^P \sum_k w_{jk}^P} \tag{4.10}$$

$$N_{ij}^{QU} = \frac{e_i f_j \sum_k \delta y_{ik}\delta y_{jk} + e_i g_j \sum_k \delta y_{ik}\delta z_{jk} + f_i f_j \sum_k \delta z_{ik}\delta y_{jk} + f_i g_j \sum_k \delta z_{ik}\delta z_{jk}}{\sum_k w_{ik}^P \sum_k w_{jk}^P} \tag{4.11}$$

$$N_{ij}^{UU} = \frac{f_i f_j \sum_k \delta y_{ik} \delta y_{jk} + f_i g_j \sum_k \delta y_{ik} \delta z_{jk} + g_i f_j \sum_k \delta z_{ik} \delta y_{jk} + g_i g_j \sum_k \delta z_{ik} \delta z_{jk}}{\sum_k w_{ik}^P \sum_k w_{jk}^P} \tag{4.12}$$

Note that the sample noise covariance matrix as defined above is biased, but the bias is small if the number of scansets or phases is large. Evaluation of the covariance matrix is computationally expensive but manageable at the size of the BICEP2/*Keck Array* maps.

## 4.7 Noise covariance and correlation maps

Every row or column of the covariance matrix represents how $T$, $Q$, and $U$ noise of a map pixel covaries with the noise in the other map pixels. These rows are map vectors, and they may be displayed as maps themselves. An example row, representing the covariance with a map pixel $i$ near the center of the field, is displayed in Figure 4.2 for the on-diagonal blocks ($N_{ij}^{TT}$, $N_{ij}^{QQ}$, $N_{ij}^{UU}$), Figure 4.3 ($N_{ij}^{TQ}$, $N_{ij}^{TU}$, $N_{ij}^{QU}$) for the upper triangular blocks and Figure 4.4 for the lower triangular blocks ($N_{ij}^{QT}$, $N_{ij}^{UT}$, $N_{ij}^{UQ}$).

Alternatively, the rows of the correlation matrix with elements $N_{ij}^{XY}/\sqrt{N_{ii}^{XX} N_{jj}^{YY}}$ can be displayed as maps to normalize the color scale. Higher signal-to-noise of the overall correlation among map pixels is achieved by stacking the noise correlation maps. The maps are translated such that the element of the map vector that is the diagonal element of the noise correlation matrix is at the origin. The centered maps are stacked and averaged. Figures 4.5 and 4.6 show the noise correlation maps corresponding to the stacks of the block components of the BICEP2 noise correlation matrix.

In $TT$, $QQ$, and $UU$, a long stripe appears along the right ascension/azimuth direction, which is primarily the result of the polynomial filtering and ground subtraction. The stripe along $\Delta(\text{dec}) = 0°$ is shown in greater detail in Figure 4.7. A narrow feature is seen in $QQ$ and $UU$ along this stripe, which is dominated by the anti-aliasing filter applied during deconvolution. The correlation with map pixels that are separated in declination/elevation by the pixel size $\Delta(\text{dec}) = 0.25°$ is shown in Figure 4.8. A large correlation extends in the declination/elevation direction, especially in $TT$, which is dominated by atmospheric power correlated over the duration of a phase. The $TQ$, $TU$, and $QU$ noise correlations of Figure 4.6 are all very small.

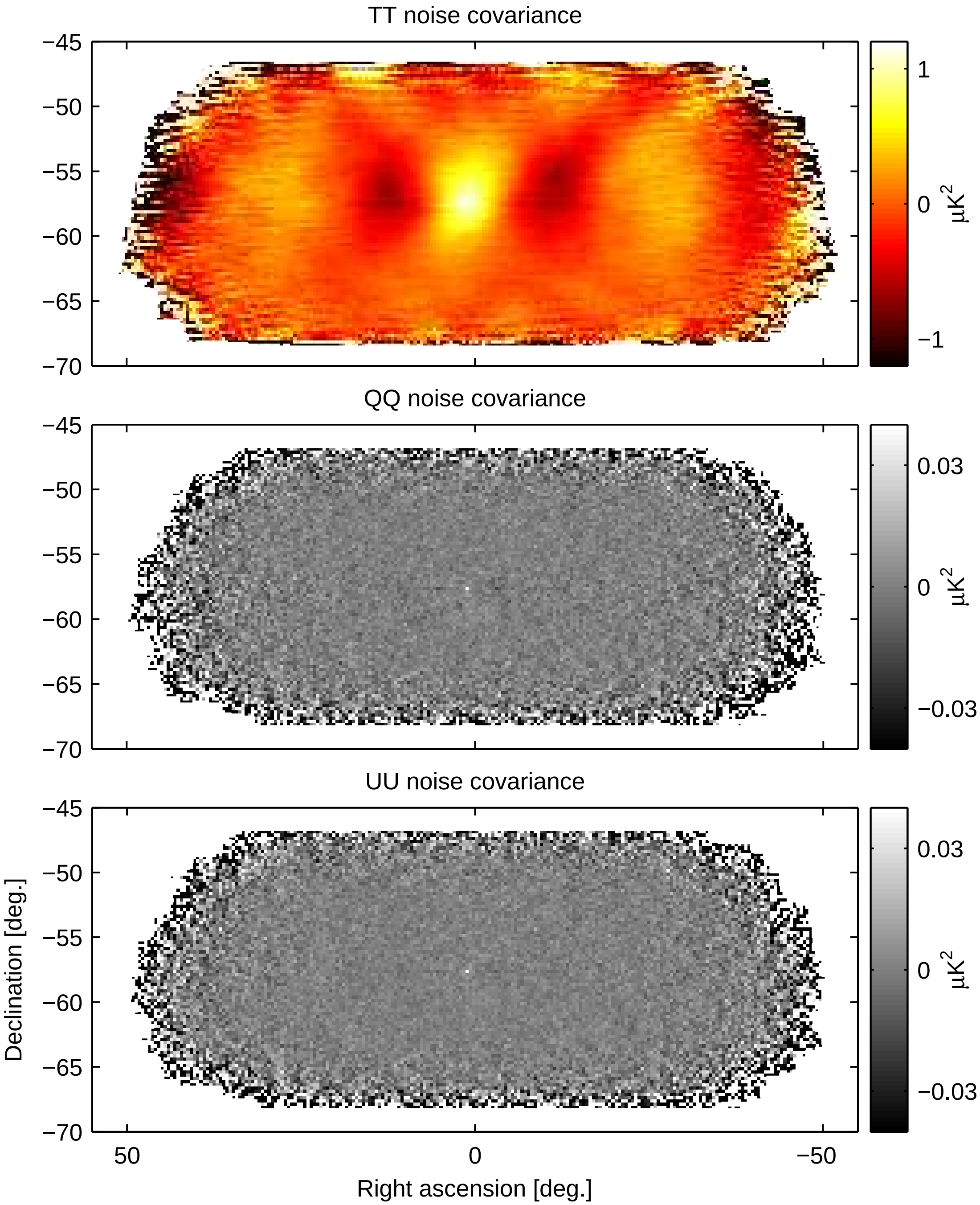

Figure 4.2: Noise covariance of a map pixel for $TT$, $QQ$, and $UU$. Each row of the covariance matrix is represented by a set of maps. The maps here are from a single row of the covariance matrix, representing the covariance with a reference pixel at (ra, dec)=(1.165°, -57.62°). Note the different color scales.

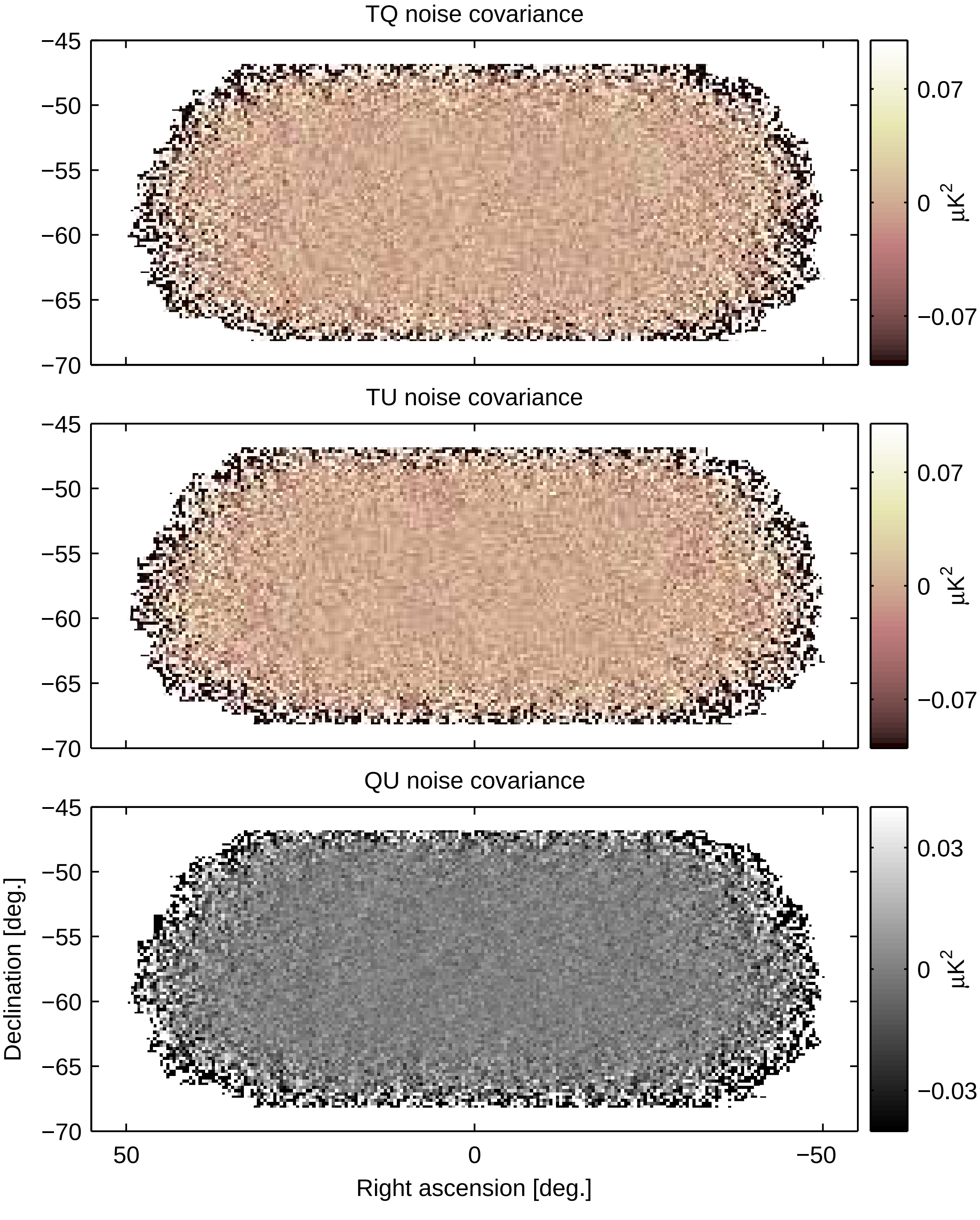

Figure 4.3: Noise covariance of a map pixel for $TQ$, $TU$, and $QU$. Each row of the covariance matrix is represented by a set of maps. The maps here are from a single row of the covariance matrix, representing the covariance with a reference pixel at (ra, dec)=(1.165°, -57.62°). For $TQ$ the plot shows how the $T$ noise of the selected pixel covaries with the $Q$ noise in all of the other pixels. Note the different color scales.

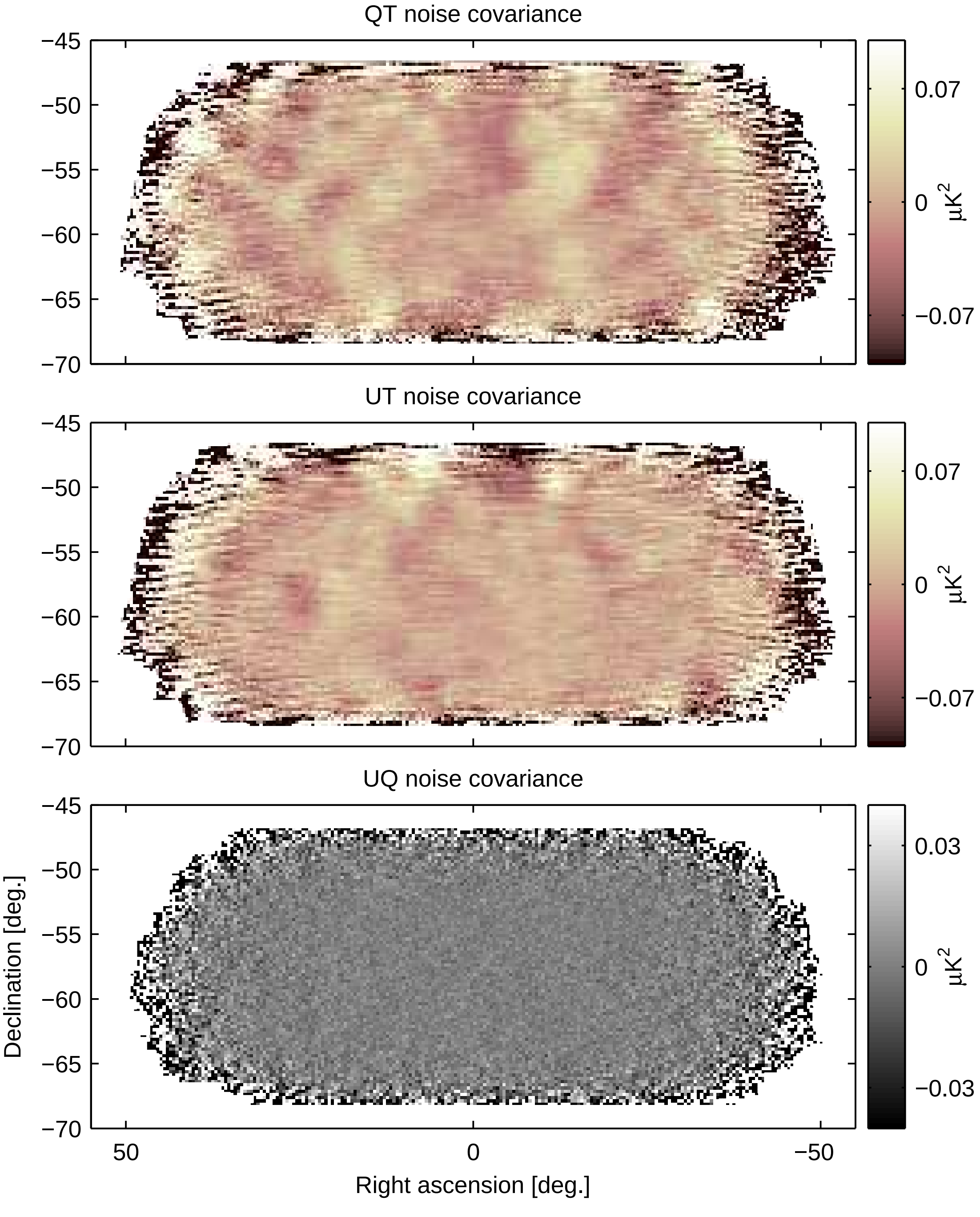

Figure 4.4: Noise covariance of a map pixel for $QT$, $UT$, and $UT$. Each row of the covariance matrix is represented by a set of maps. The maps here are from a single row of the covariance matrix, representing the covariance with a reference pixel at (ra, dec)=(1.165°, -57.62°). For $QT$ the plot shows how the $Q$ noise of the selected pixel covaries with the $T$ noise in all of the other pixels. Note the different color scales.

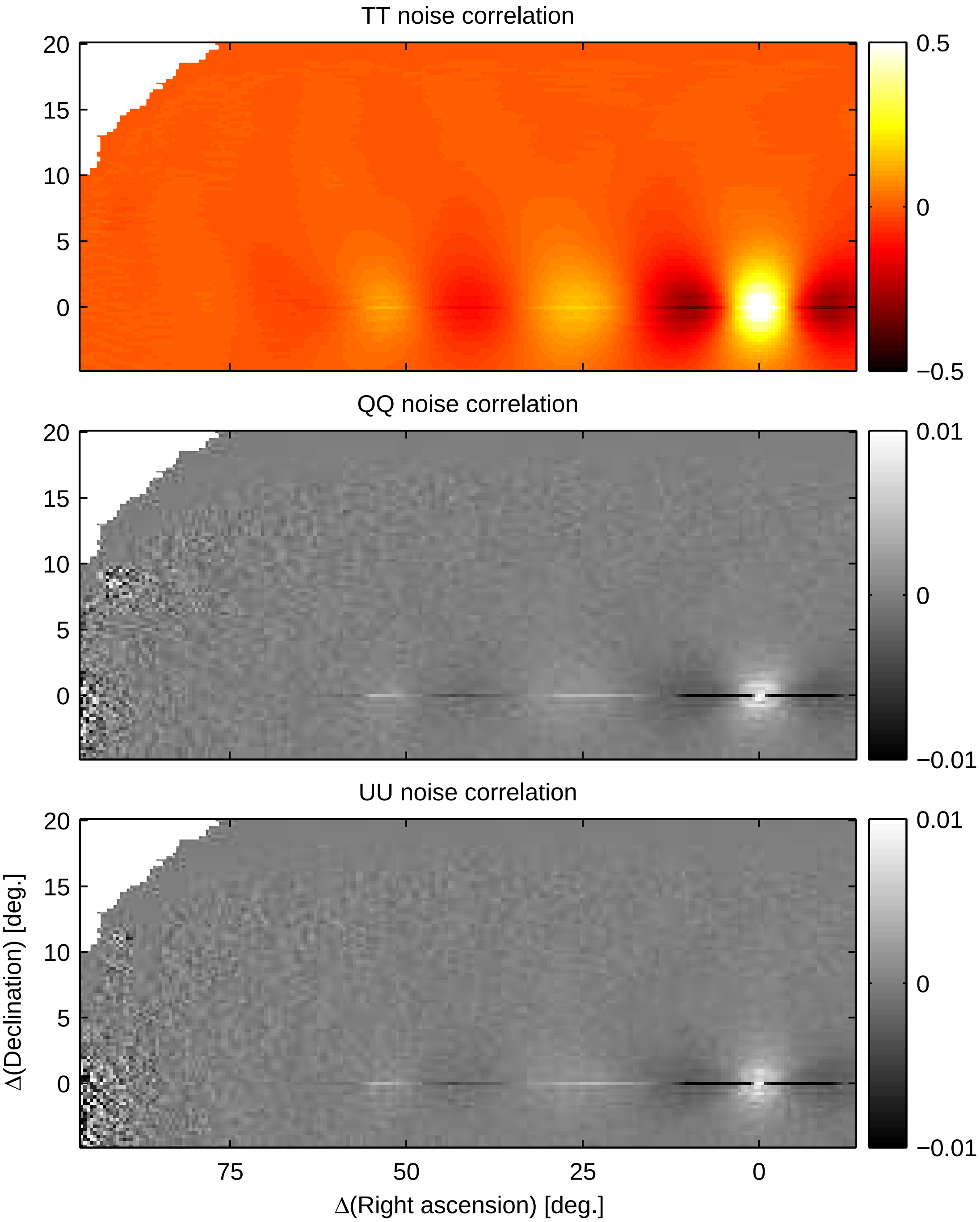

Figure 4.5: Stacked noise correlation for $TT$, $QQ$, and $UU$. Each row of the correlation matrix is represented by a set of maps. The maps are translated such that the diagonal element is at the origin. Maps of the correlation of pixels near the edge of the field are excluded in the average. The unplotted region is mostly symmetrical with the plotted region. Note the different color scales.

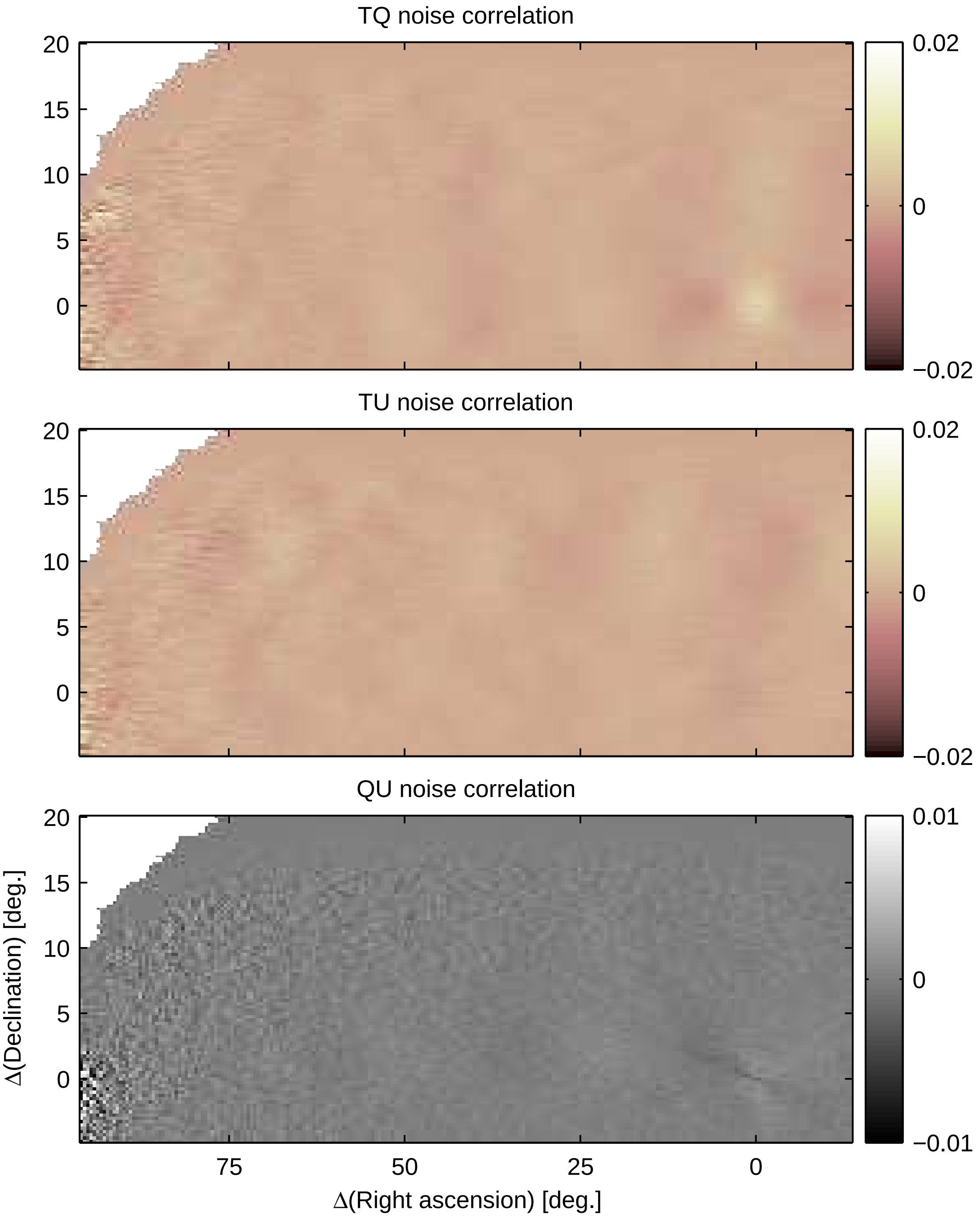

Figure 4.6: Stacked noise correlation for $TQ$, $TU$, and $QU$. Each row of the correlation matrix is represented by a set of maps. The maps are translated such that the diagonal element is at the origin. Maps of the correlation of pixels near the edge of the field are excluded in the average. The unplotted region is mostly symmetrical with the plotted region. Note the different color scales.

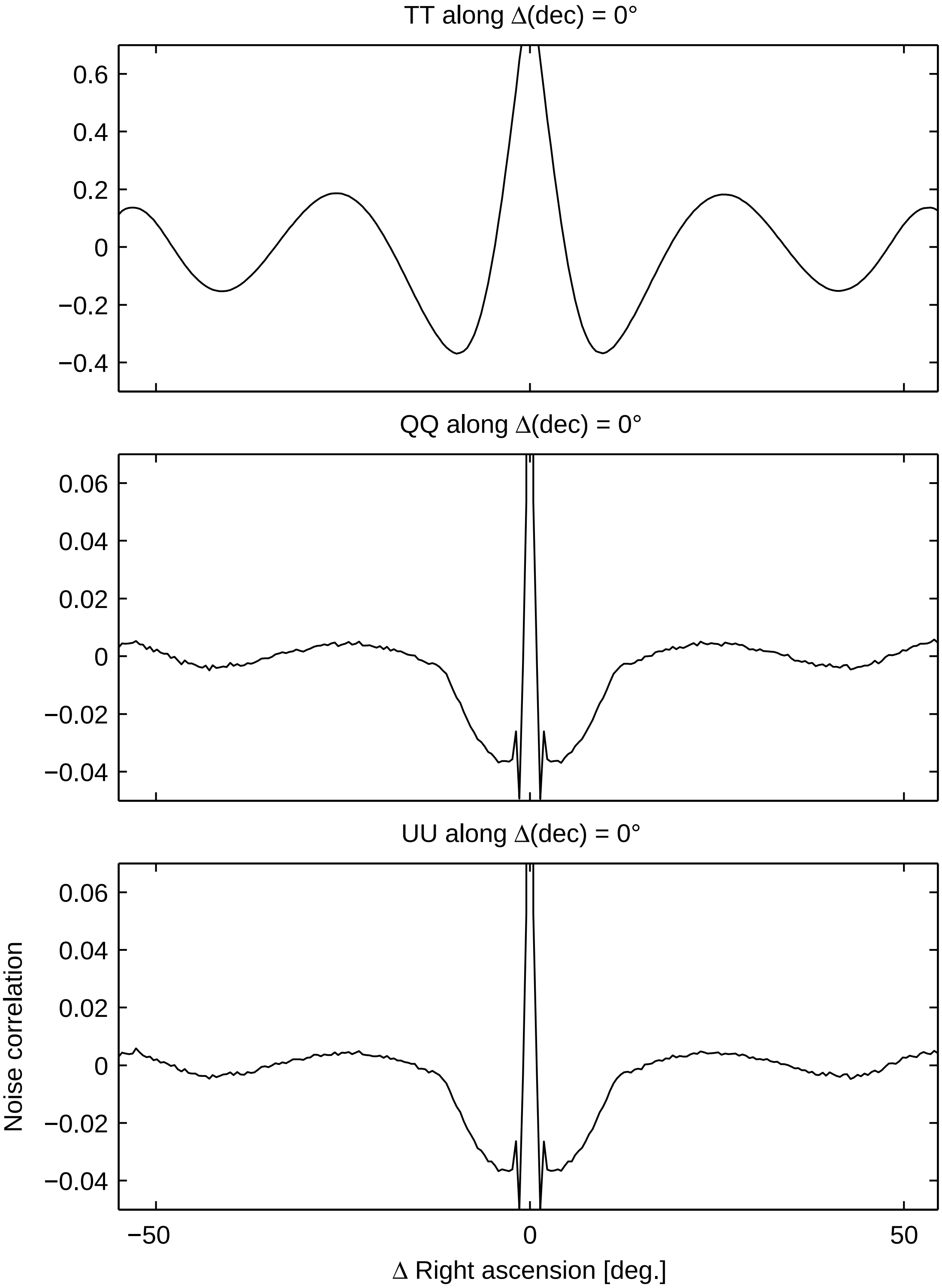

Figure 4.7: Stacked noise correlation for $TT$, $QQ$, and $UU$ along the $\Delta(\text{dec}) = 0^\circ$ stripe. The data shown match Figure 4.5.

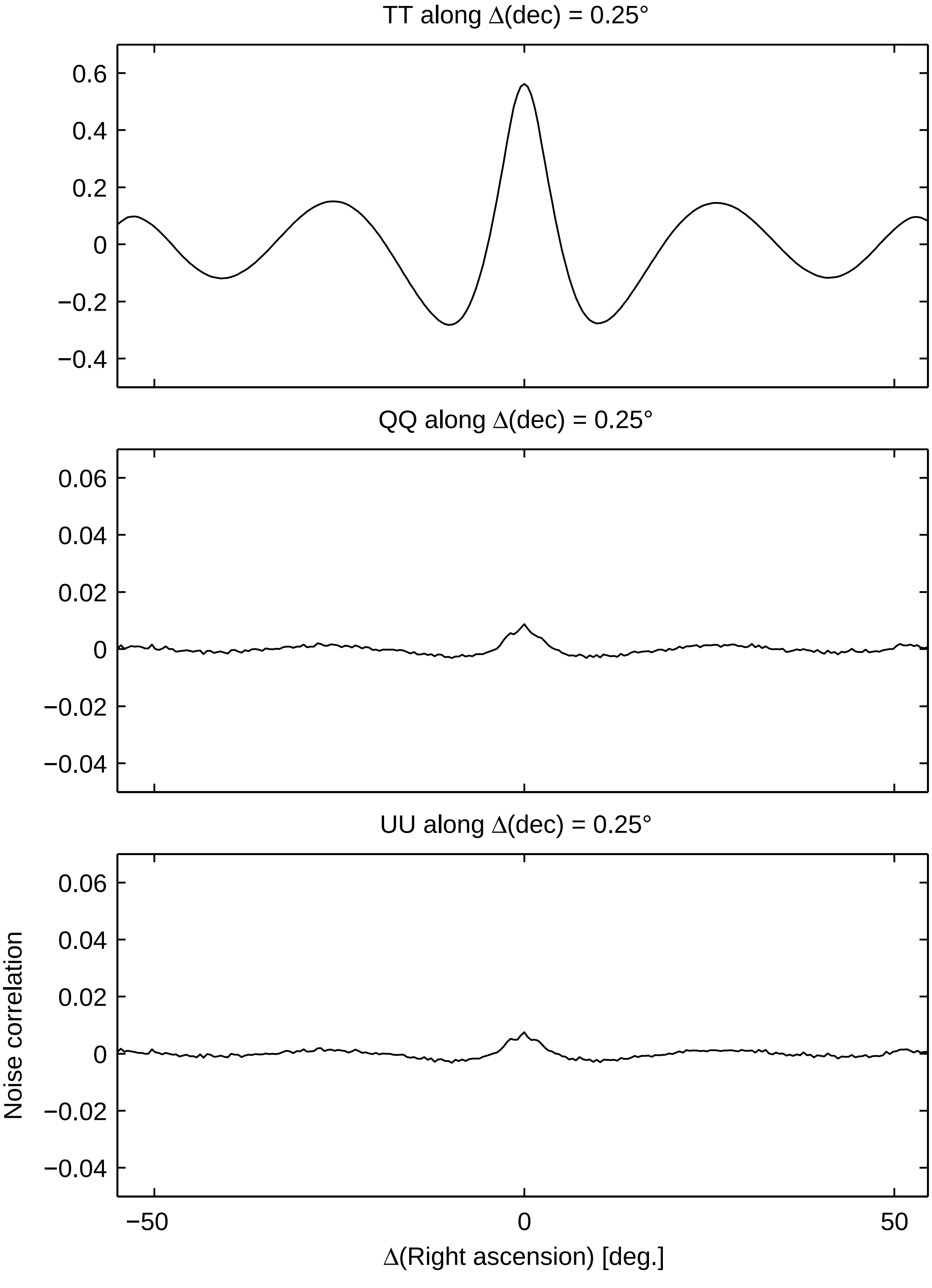

Figure 4.8: Stacked noise correlation for $TT$, $QQ$, and $UU$ along $\Delta(\text{dec}) = 0.25^{\circ}$, nearest-neighbor in declination to the $\Delta(\text{dec}) = 0^{\circ}$ stripe. The data shown match Figure 4.5.

## 4.8 Cross-spectrum noise distribution

Suppose that $f(x)$ and $g(x)$ share a single correlated signal and contain additive noise. In the Fourier domain, we write this as $\hat{f}(k) = \hat{s} + \hat{n}_1$ and $\hat{g}(k) = \hat{s} + \hat{n}_2$. Their cross-spectrum is

$$\hat{f}(k)\hat{g}^*(k) = |s|^2 + s^* n_1 + s n_2^* + n_1 n_2^* \tag{4.13}$$

A 1D cross-spectrum is the average of this over modes sharing the same $|k|$. If the noise is Gaussian, then a model for the noise contribution to the 1D cross-spectrum is the sum of products of Gaussians. Distributions of this form are the matrix elements of the Wishart distribution. We review the functional form of this distribution below.

Consider two normally-distributed random variables $X$ and $Y$ centered at zero and with standard deviations $\sigma_x$ and $\sigma_y$. The geometric mean of the standard deviations is $\sigma = \sqrt{\sigma_x \sigma_y}$, and their correlation coefficient is $\rho = \mathrm{cov}(X, Y)/\sigma^2$. We wish to find the probability density of $Z = \sum_{i=1}^{n} XY$. It is easiest to begin with its moment-generating function [22]

$$\mathrm{mgf}(t) = \frac{1}{\left(1 - 2\sigma^2 \rho t - \sigma^4 (1-\rho^2) t^2\right)^{n/2}} \tag{4.14}$$

This is easily seen to reduce to the moment-generating function of a $\chi^2$ distribution for $\rho = 1$. The probability density function is

$$\mathrm{pdf}(z) = \frac{1}{\sqrt{\pi 2^{n-1} (1-\rho^2)}} \frac{|z|^{(n-1)/2}}{\Gamma\left(\frac{n}{2}\right) \sigma^{n+1}} K_{(n-1)/2}\left(\frac{|z|}{\sigma^2 (1-\rho^2)}\right) e^{\frac{\rho z}{\sigma^2 (1-\rho^2)}} \tag{4.15}$$

where $K_\nu(u)$ is the modified Bessel function of the second kind. This is within the family of variance-gamma distributions

$$\mathrm{pdf}(z) = \frac{(\alpha^2 - \beta^2)^\lambda |z-\mu|^{\lambda - 1/2} K_{\lambda - 1/2}\left(\alpha |z-\mu|\right)}{\sqrt{\pi}\, \Gamma(\lambda) (2\alpha)^{\lambda - 1/2}} e^{\beta(z-\mu)} \tag{4.16}$$

with parameters $\alpha^{-1} = \sigma^2 (1-\rho^2)$, $\beta^{-1} = \sigma^2(1-\rho^2)/\rho$, $\lambda = n/2$, and $\mu = 0$.

There are a few special cases of the variance-gamma distribution for which the probability density does not require Bessel functions. If $X$ and $Y$ are completely correlated with $\rho = 1$, then it becomes a scaled $\chi^2$ distribution

$$\mathrm{pdf}(z) = \begin{cases} \frac{1}{\Gamma(\frac{n}{2})2^{n/2}\sigma^2}|z|^{n/2-1}e^{-\frac{z}{2\sigma^2}}, & z \geq 0 \\ 0, & z < 0 \end{cases} \tag{4.17}$$

If $X$ and $Y$ are completely anticorrelated with $\rho = -1$, then it becomes a reflected, scaled $\chi^2$ distribution

$$\mathrm{pdf}(z) = \begin{cases} \frac{1}{\Gamma(\frac{n}{2})2^{n/2}\sigma^2}|z|^{n/2-1}e^{\frac{z}{2\sigma^2}}, & z \leq 0 \\ 0, & z > 0 \end{cases} \tag{4.18}$$

If $n = 2$, then the relation $K_{1/2}(u) = \sqrt{\frac{\pi}{2u}}\, e^{-u}$ reduces the variance-gamma distribution to

$$\mathrm{pdf}(z) = \frac{1}{2\sigma^2} e^{\frac{\rho z - |z|}{\sigma^2(1-\rho^2)}} \tag{4.19}$$

## 4.9 Initial value estimation

The detection significance is estimated by comparing test statistics relative to the signal+noise simset. This simset is often limited at 499 simulations and may not contain enough simulations to cover the far tails of the distribution, especially if the signal+noise model is a poor fit to the observed data. If information about the tails is needed, then the simset can be replaced by an analytical model that best fits the simulation. Estimates of the parameters of the model are required as initial values for the fitting algorithm. Here we describe how to estimate the parameters for a variance-gamma distribution.

The moment-generating function of the variance-gamma distribution is simple, so we can easily calculate the moments/cumulants and related quantities. The first four (mean $m$, standard deviation $s$, skewness $\gamma$, kurtosis $\kappa$) are

$$m = n\rho\sigma^2 \tag{4.20}$$

$$s = \sqrt{n(1+\rho^2)}\sigma^2 \tag{4.21}$$

$$\gamma = \frac{2n\rho(3+\rho^2)\sigma^6}{s^3} \tag{4.22}$$

$$\kappa - 3 = \frac{6n(1+6\rho^2+\rho^4)\sigma^8}{s^4} \tag{4.23}$$

(Note that $s$ is the standard deviation of the variance-gamma distribution whereas $\sigma$ is the parameter coming from the widths of the underlying Gaussian distributions.) There are several properties to notice about these four equations. First, the condition $\rho^2 \geq 0$ implies that $m$, $\gamma$, and $\rho$ are constrained to have the same sign. Second, the condition $\rho^2 \leq 1$ implies the inequality $2s \geq m\gamma$. Finally, the distribution is leptokurtic (i.e., $\kappa > 3$) with $\kappa \to 3$ as $n \to \infty$ (central limit theorem).

If there is reason to believe that $\rho = 1$ as in an autospectrum, then the first pair of equations solve to

$$n = \frac{2m^2}{s^2} \tag{4.24}$$

$$\sigma^2 = \frac{s^2}{2m} \tag{4.25}$$

The initial value estimate replaces $m$ and $s$ with their estimates from the sample distribution $\hat{m}$ and $\hat{s}$. If there is reason to believe that $\rho = 0$ as in an ideal cross-spectrum with uncorrelated noise, then the mean and skewness are zero. The other equations solve to

$$n = \frac{6}{\kappa - 3} \tag{4.26}$$

$$\sigma^2 = s\sqrt{\frac{\kappa - 3}{6}} \tag{4.27}$$

The initial value estimate replaces $s$ and $\kappa$ with $\hat{s}$ and $\hat{\kappa}$, but this requires that $\hat{\kappa} > 3$. This is not always the case among a simset of 499 samples, especially if the number of degrees of freedom for a bandpower is large. On the other hand, the occurrence of $\hat{\kappa} \leq 3$ suggests that $n$ is large. In that case, the central limit theorem has brought the variance-gamma distribution to be very close to a Gaussian. Thus the first step is to verify that fitting to a variance-gamma distribution is appropriate. In addition to a simple Gaussianity test, we can check that the sample kurtosis of the simset obeys $\hat{\kappa} > 3$. Otherwise the distribution is just as well modeled by a Gaussian.

A more general case is for partial correlation. Ignoring the kurtosis, we have three unknowns and three polynomial equations. That leaves us with the following possibilities:

$$n = \frac{m}{s\gamma}\left(3 + \sqrt{9 - 4\frac{m\gamma}{s}}\right) \tag{4.28}$$

$$\sigma^2 = \frac{s^2}{4|m|}\sqrt{-6 + 4\frac{m\gamma}{s} + 2\sqrt{9 - 4\frac{m\gamma}{s}}} \tag{4.29}$$

$$\rho = \operatorname{sgn}(m)\left(\frac{\sqrt{9 - 4\frac{m\gamma}{s}} - 1}{8 - 4\frac{m\gamma}{s}}\right)\sqrt{-6 + 4\frac{m\gamma}{s} + 2\sqrt{9 - 4\frac{m\gamma}{s}}} \tag{4.30}$$

Initial value estimates come from replacing $m$, $s$, and $\gamma$ above with $\hat{m}$, $\hat{s}$, and $\hat{\gamma}$. This method works if the correlation is far enough from zero and the simset is large enough to ensure that $\hat{m}$ and $\hat{\gamma}$ have the same sign. If $\hat{m}$ and $\hat{\gamma}$ have opposite signs, however, then this procedure can fail. Since this issue mostly arises in the regime where $\rho$ is close to zero, it is recommended that the initial value estimates obtained from the sample kurtosis assuming $\rho = 0$ be used. Again, the distribution should be found to fail a Gaussianity test and have $\hat{\kappa} > 3$ before a variance-gamma model is used instead of a Gaussian model.

# Chapter 5

# Results

We present the maps of the Bicep2/*Keck Array* 95 and 150 GHz data collected through 2014 in Section 5.1. The maps that include 2014 data are new in this thesis and should be treated as preliminary. Based on the consistency of the 2010–2013 data set as assessed in Section 5.2, the 150 GHz data are combined and reduced to angular power spectra in Section 5.3. The analysis matches the results paper of BK–V [12]. The Bicep2/*Keck Array* data are further combined with *Planck* data in Section 5.4, as it was done in the joint analysis paper of BKP [10]. The model assumptions of the Galactic dust foreground is in Section 5.5. We review the framework for evaluating likelihoods in Section 5.6, and in Section 5.7 we use the likelihood framework to constrain cosmological parameters. Section 5.8 includes a method for separating the CMB and dust components of the likelihood, with supplemental tables and figures in Appendix C. We conclude in Section 5.9 with a summary of the results and a forecast of the continued sensitivity of *Keck Array*.

Significant portions of the material below were prepared for BK–V [12] and BKP [10]. The material taken from BKP in particular belongs to all 276 coauthors. I do not in any way claim originality of the BKP analysis for this thesis. Nevertheless, I include it to provide the complete context of the final results and the current state of CMB cosmology.

## 5.1 Maps

The Bicep2 and *Keck Array* 150 GHz $T/Q/U$ maps calculated from the mapmaking procedure in Section 3.2. The two experiments largely agree (see Section 5.2), and their accumulation quantities can be combined into

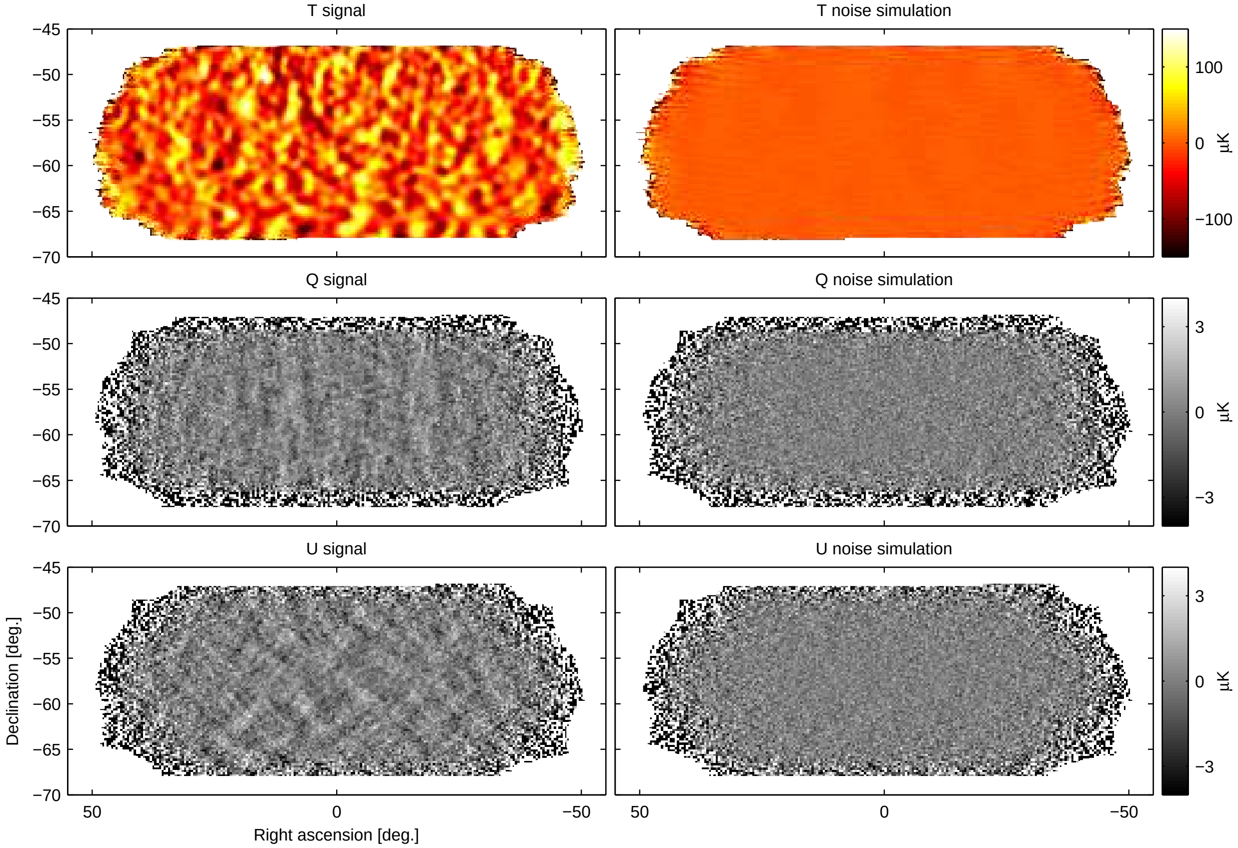

Figure 5.1: *Keck Array* 95 GHz $T$, $Q$, and $U$ maps. The maps are made using the 95 GHz data collected in 2014 and should be treated as preliminary. The left column shows the basic signal maps with 0.25° pixelization as output by the reduction pipeline. The right column shows the first sign-flip noise simulation. No additional filtering other than that imposed by the instrument beam (FWHM $\sim 0.8°$) has been done. Note that the structure seen in the $Q$ and $U$ signal maps is as expected for an $E$-mode dominated sky.

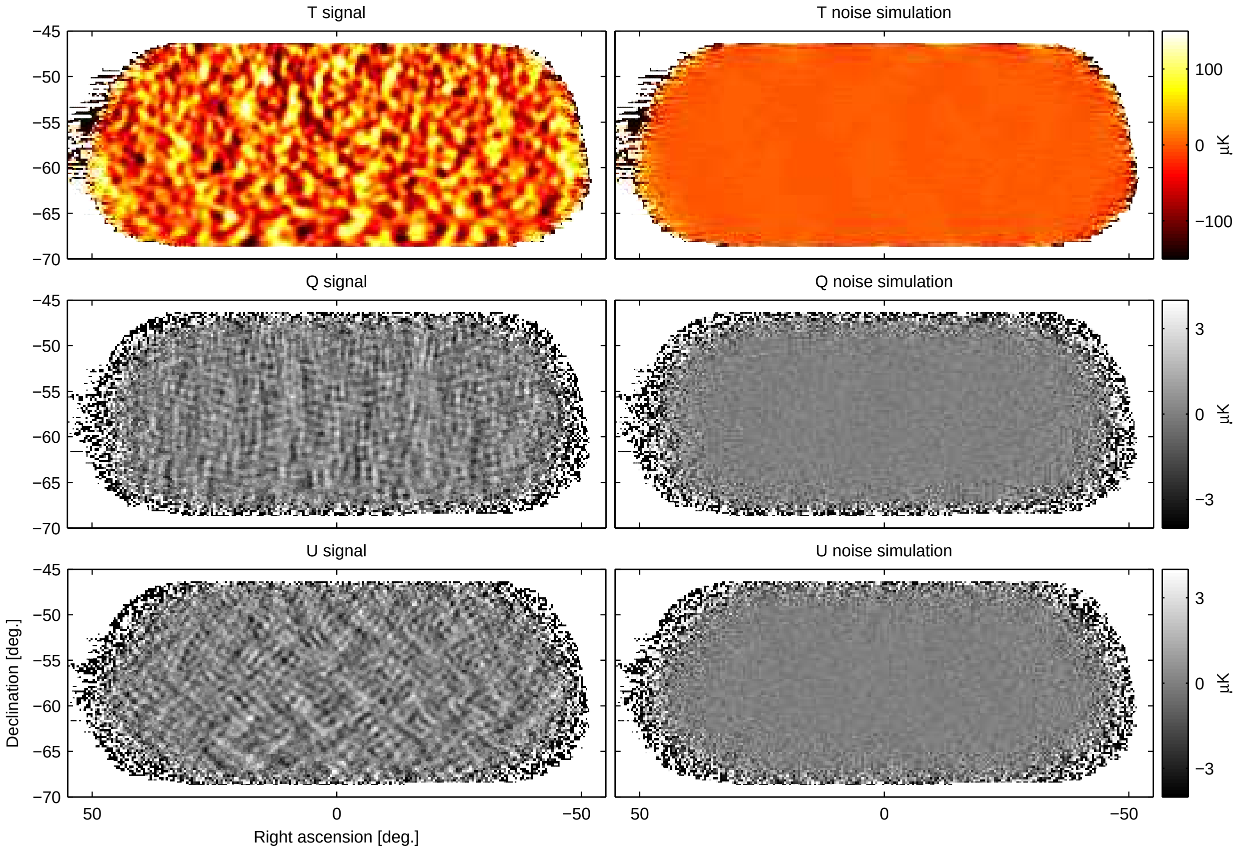

Figure 5.2: Bicep2+*Keck Array* 150 GHz $T$, $Q$, and $U$ maps. The maps are made using all 150 GHz data collected through 2014 and should be treated as preliminary. The left column shows the basic signal maps with 0.25° pixelization as output by the reduction pipeline. The right column shows the first sign-flip noise simulation. No additional filtering other than that imposed by the instrument beam (FWHM $\sim 0.5°$) has been done. Note that the structure seen in the $Q$ and $U$ signal maps is as expected for an $E$-mode dominated sky.

Table 5.1: Total sensitivity of polarized maps

| Data set (year) | Map depth [nK deg ($\mu$K arcmin)] | Total sensitivity [nK] | Survey weight [$\mu$K$^{-2}$] |
|---|---|---|---|
| BICEP2 (2010–2012) | 87 (5.2) | 3.15 | 101000 |
| BK 150 GHz (2010–2013) | 57 (3.4) | 2.01 | 248000 |
| BK 150 GHz (2010–2014) | 50 (3.0) | 1.78 | 316000 |
| *Keck Array* 95 GHz (2014) | 126 (7.6) | 4.60 | 61000 |

a total BICEP2+*Keck Array* 150 GHz map (BK150). Preliminary BICEP2+*Keck Array* 150 GHz $T/Q/U$ maps from 2010–2014 data are shown in Figure 5.2. Preliminary *Keck Array* 95 GHz maps from 2014 data are shown in Figure 5.1. Note that the 95 GHz maps have a coarser angular resolution (FWHM 0.8° beams) than the 150 GHz maps, which results in a more muted appearance with fewer resolved features on small angular scales. The 95 GHz maps, while signal dominated, are still somewhat noisier than the 150 GHz maps simply due to the smaller amount of integration time. Sign-flip noise simulation maps, introduced in Section 4.4, are shown as noise estimates.

The Stokes $Q$ and $U$ maps are matrix purified and converted into $E$-mode and $B$-mode by the procedure in Sections 3.4 and 3.7. The $E/B$ maps of the entire BICEP2 data set are in Figure 5.3. The $E/B$ maps of the *Keck Array* 150 GHz data collected in 2012–2013 are in Figure 5.4. For now, we withhold the $E$ and $B$ maps of the new 2014 data.

Map depths are estimated by the level of a noise simulation or jackknife in the deepest region, as described in BK–II [7]. The total sensitivity is the depth divided by the square root of the effective area (approximately 390 deg$^2$ for both telescopes) that accounts for the apodization. The survey weight is the inverse square of the total sensitivity and increases linearly with time for an experiment with constant instantaneous sensitivity. The map depths, total sensitivities, and survey weights are listed in Table 5.1.

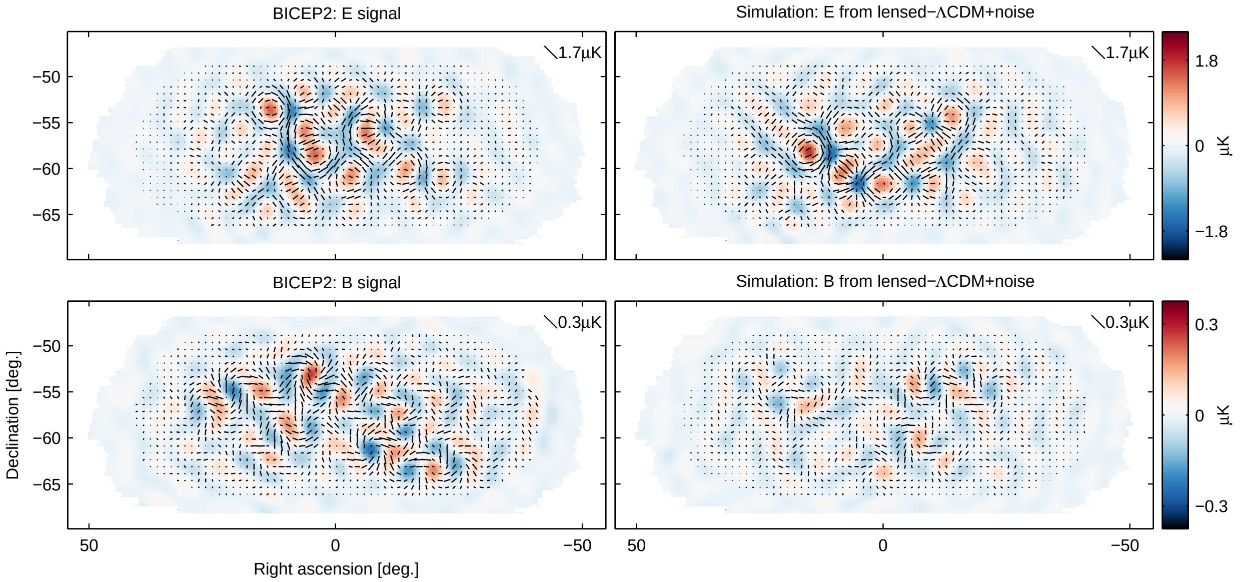

Figure 5.3: *Left:* Bicep2 apodized $E$-mode and $B$-mode maps filtered to $50 < \ell < 120$. The maps are made using all 150 GHz data collected by the Bicep2 CMB survey in 2010–2012 presented in BK–I [9]. *Right:* The equivalent maps for the first of the lensed-ΛCDM+noise simulations. The color scale displays the $E$-mode scalar and $B$-mode pseudoscalar patterns while the lines display the equivalent magnitude and orientation of linear polarization. Note that the $E$-mode and $B$-mode maps use different color/length scales.

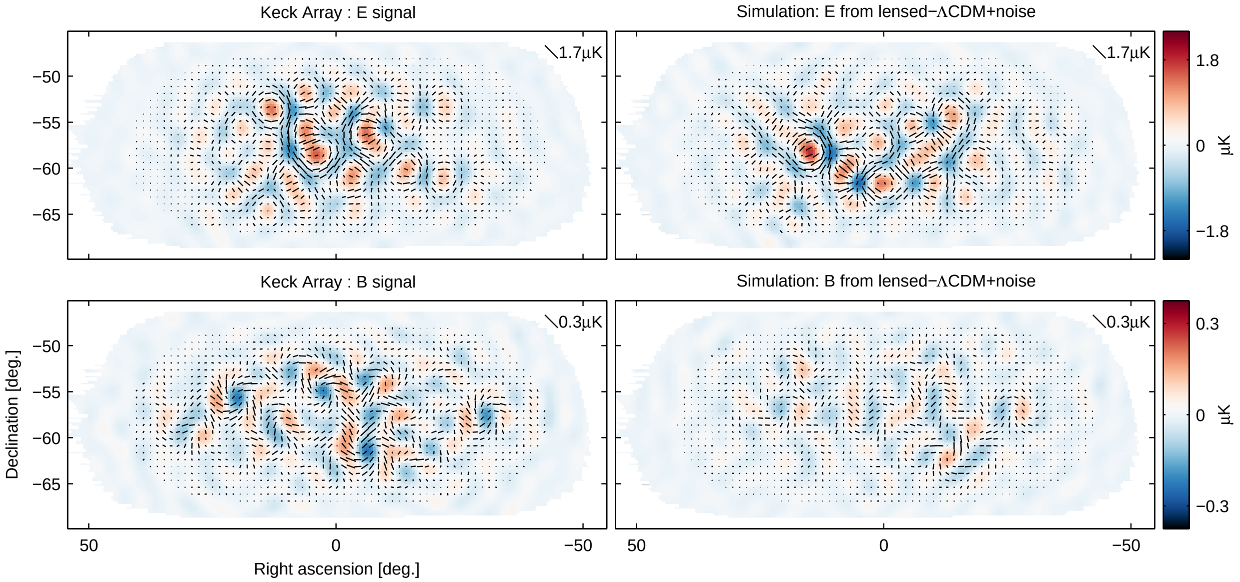

Figure 5.4: *Left: Keck Array* 150 GHz apodized $E$-mode and $B$-mode maps filtered to $50 < \ell < 120$. The maps are made using all 150 GHz data collected by the *Keck Array* CMB survey in 2012–2013 presented in BK–V [12]. *Right:* The equivalent maps for the first of the lensed-ΛCDM+noise simulations. The color scale displays the $E$-mode scalar and $B$-mode pseudoscalar patterns while the lines display the equivalent magnitude and orientation of linear polarization. Note that the $E$-mode and $B$-mode maps use different color/length scales.

## 5.2 Consistency

Before accepting the data, it is important to verify internal consistency. A way to test for systematic errors in the maps is to divide the data into two halves that may ordinarily cause the error to cancel, flip the sign of one of the halves, and then average them into a jackknife map. Let $m_1$ and $m_2$ be two halves of the data with weights $w_1$ and $w_2$ that average into a total map $\overline{m}$. Let $\epsilon_1$ be some additive error to $m_1$ that could be noise or a systematic error such that $m_1 = \overline{m} + \epsilon_1$ and $m_2 = \overline{m} - \frac{w_1}{w_2}\epsilon_1$. The jackknife map is

$$\frac{m_1 - m_2}{2} = \left(\frac{w_1 + w_2}{2w_2}\right)\epsilon_1 \tag{5.1}$$

If the weights of the two halves of the jackknife are equal, then the jackknife is $\epsilon_1$. There is reason to suspect a systematic error associated with the data split if $\epsilon_1$ is significantly larger than the amount expected from the noise level of the maps, as estimated from the simulations.

The *Keck Array* data were split in 16 different ways to test for internal consistency. The definitions of these splits and their motivations in terms of possible systematic errors are extensively described in BK-III [8]. If a contaminating signal exists in only one half of the data split, then it should show up with as much significance in the jackknife as in the signal map. However, some jackknives are more sensitive to certain systematics than the signal map because of inherent cancellation effects which operate in the full map. The different splits can be organized by category. The first set of jackknives probes for systematics that differ between different subsets of channels, which include correlated detector properties and FPU geometry. The next set of jackknives is temporal. An example temporal split compares the first half of the data by weight to the second half of the data by weight. It is essentially like a sign-flip noise simulation with a very particular sign-flip sequence, provided that there is no amplified systematic error in the jackknife. Another set of jackknives is based on external contamination, including interference from activity at South Pole Station. A set of jackknives that particularly amplifies the differential beam properties is the deck rotation jackknives. As is described in BK–III, a 180° deck rotation cancels out differential pointing. The deck jackknife, which differences the 180° rotations, amplifies the leakage by an order of magnitude in comparison to that present in the full data set. *Keck Array* also started taking data at 90° complement deck rotations in the 2013 observing season, and this jackknife is sensitive to differential gain or differential beam width leakage. The alternative deck jackknife is defined to be the difference of the 90° rotations for 2013. In this special case, the statistics for the 2012 and 2013 data are separate.

A vector of $\mathcal{D}_{\ell'}$ bandpowers derived from each jackknife map, real or simulation, is denoted $\mathbf{d}$. The bandpower covariance matrix $\mathbf{D}$ is estimated from the lensed-ΛCDM+noise simulations. A simple $\chi^2$ statistic

$$\chi^2 = (\mathbf{d} - \langle \mathbf{d}_{\mathrm{s+n}} \rangle)^{\mathrm{T}} \mathbf{D} (\mathbf{d} - \langle \mathbf{d}_{\mathrm{s+n}} \rangle) \tag{5.2}$$

and a $\chi$-like statistic, defined not as the square root of $\chi^2$ but simply the sum of scaled deviations,

$$\chi = \sum_i \frac{d_i - \langle d_{\mathrm{s+n},i} \rangle}{\sqrt{D_{ii}}} \tag{5.3}$$

are evaluated for both the real data and the lensed-ΛCDM+noise simulations.

For each of these statistics, we calculate the probability to exceed (PTE) the observed value by comparing to the values obtained in the 499 lensed-ΛCDM+noise simulations. The statistics are evaluated for all nine $\ell$ bins and for only the lowest five $\ell$ bins, where Bicep2/*Keck Array* has the best sensitivity and where an IGW $B$-mode signal may be brighter than the lensing $B$-mode signal. The PTE values for the $\chi^2$ and $\chi$ statistics using bandpowers 1–5 and 1–9 for polarization are tabulated in BK–I [9] and BK–V [12]. The PTE distributions are consistent with uniform. The most extreme value is the $\chi$ PTE for Bicep2's tile jackknife, for which the jackknife of the real data is right at the end of the 499 simulations, and may be related to variation in absolute calibration among detectors.

Some systematic effects are not amenable to jackknife tests but can be simulated. An example is the effect of the residual beam effects beyond the elliptical Gaussian approximation. Deprojection removes imperfections to the elliptical Gaussians, but there is an undeprojected residual. Simulations based on the beam maps estimate the amount of leaked power and are discussed in C. L. Wong's thesis [91]. The residual leakage from beam effects is subdominant to the observed signal and noise levels in 1D angular power spectra, and the bias predicted from the simulations is subtracted from the real bandpowers. Many other potential contaminants relating to optical, thermal, and electrical imperfections are simulated and found to be small. Details of these simulations are presented in BK–III.

## 5.3 Bicep2/*Keck Array* power spectra

The Bicep2/*Keck Array* matrix-purified 150 GHz 2D angular power spectra are binned and averaged into 1D angular power spectra. The autospectra for Bicep2 or *Keck Array* are evaluated individually and the cross-spectra of the two experiments are evaluated. As an example, Figure 5.5 shows the *Keck Array* 1D autospectra. The lensed-ΛCDM model is a good fit to all angular power spectra, with the exception of $BB$ at low $\ell$, where a strong excess is observed.

The *Keck Array* data are also compared to Bicep2 for consistency between the two experiments. This can be done by a simple jackknife between the maps or by comparing the autospectra and cross-spectra of the experiments. To test the compatibility of the resulting bandpowers with null we compare them to the differences of signal+noise simulations that share common input skies. In such tests it is necessary that the simulations contain power roughly equal to the real sky as the cross terms between signal and noise increase the fluctuation of the differences even for perfectly common sky coverage. We added power to the signal simulations that matches the amplitude of the signal in excess of ΛCDM in bandpowers 1–5. (The origin of the extra signal over ΛCDM is not important here—only its approximate amplitude.) The results are shown in Figure 5.6. We then proceed to calculate the PTE of the $\chi$ and $\chi^2$ statistics versus the simulated distributions for the two bandpower ranges and give the results in Table 5.2. In both the figure and the table we note the effect of the two bandpowers at $\ell \approx 220$ that are high with respect to lensed-ΛCDM in B2xB2 (as noted in the Bicep2 Results Paper) but not in KxK and B2xK—as expected these also show up in the map difference. Again note that the PTE values are correlated (both along and between rows of the table) so overinterpretation should be avoided. Our conclusion is that the Bicep2 and *Keck Array* data are consistent—especially in the lowest five bandpowers, where an IGW contribution would be strongest.

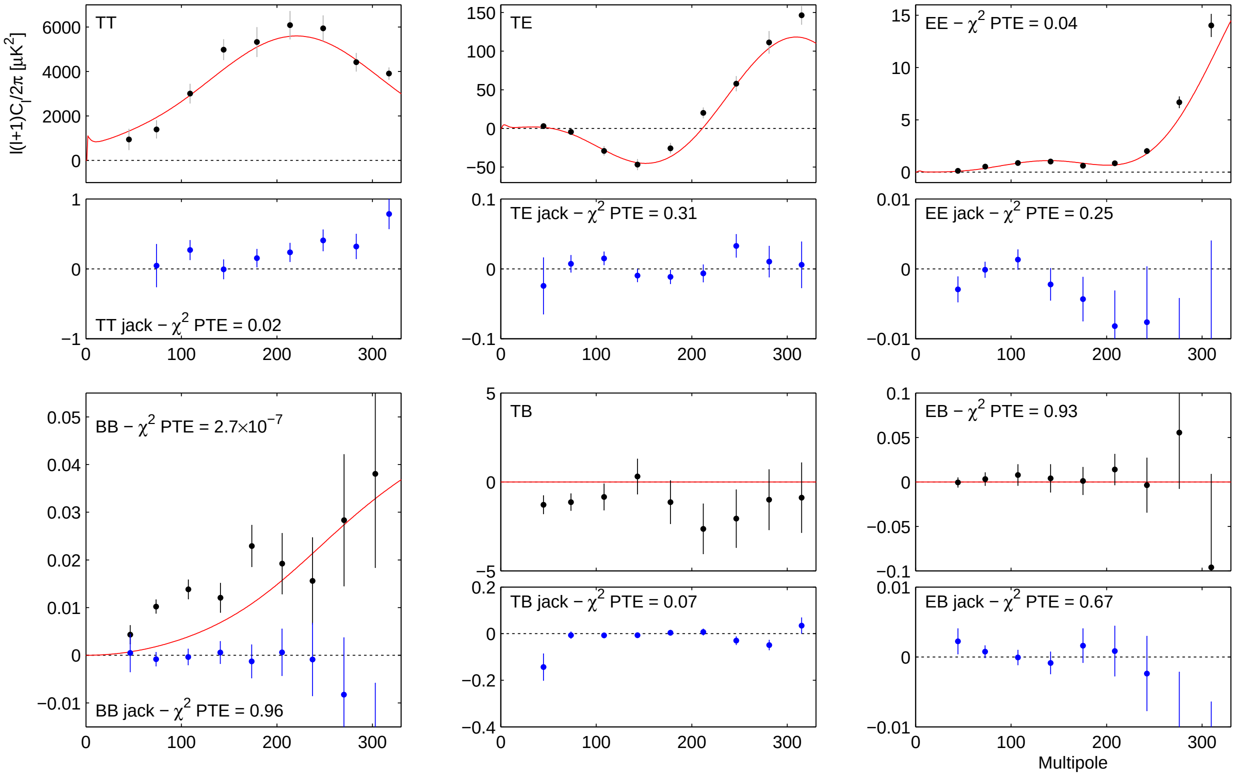

Figure 5.5: *Keck Array* power spectrum results for signal (black points) and early/late season jackknife (blue points). The solid red curves show the lensed-ΛCDM theory expectations. The error bars are the standard deviations of the lensed-ΛCDM+noise simulations and hence contain no sample variance on any additional signal component. The probability to exceed (PTE) the observed value of a simple $\chi^2$ statistic is given (as evaluated against the simulations). Note the very different $y$-axis scales for the jackknife spectra (other than $BB$). See the text for additional discussion of the $BB$ spectrum. (Note that the calibration procedure uses $EB$ to set the overall polarization angle so $TB$ and $EB$ as plotted above cannot be used to measure astrophysical polarization rotation.)

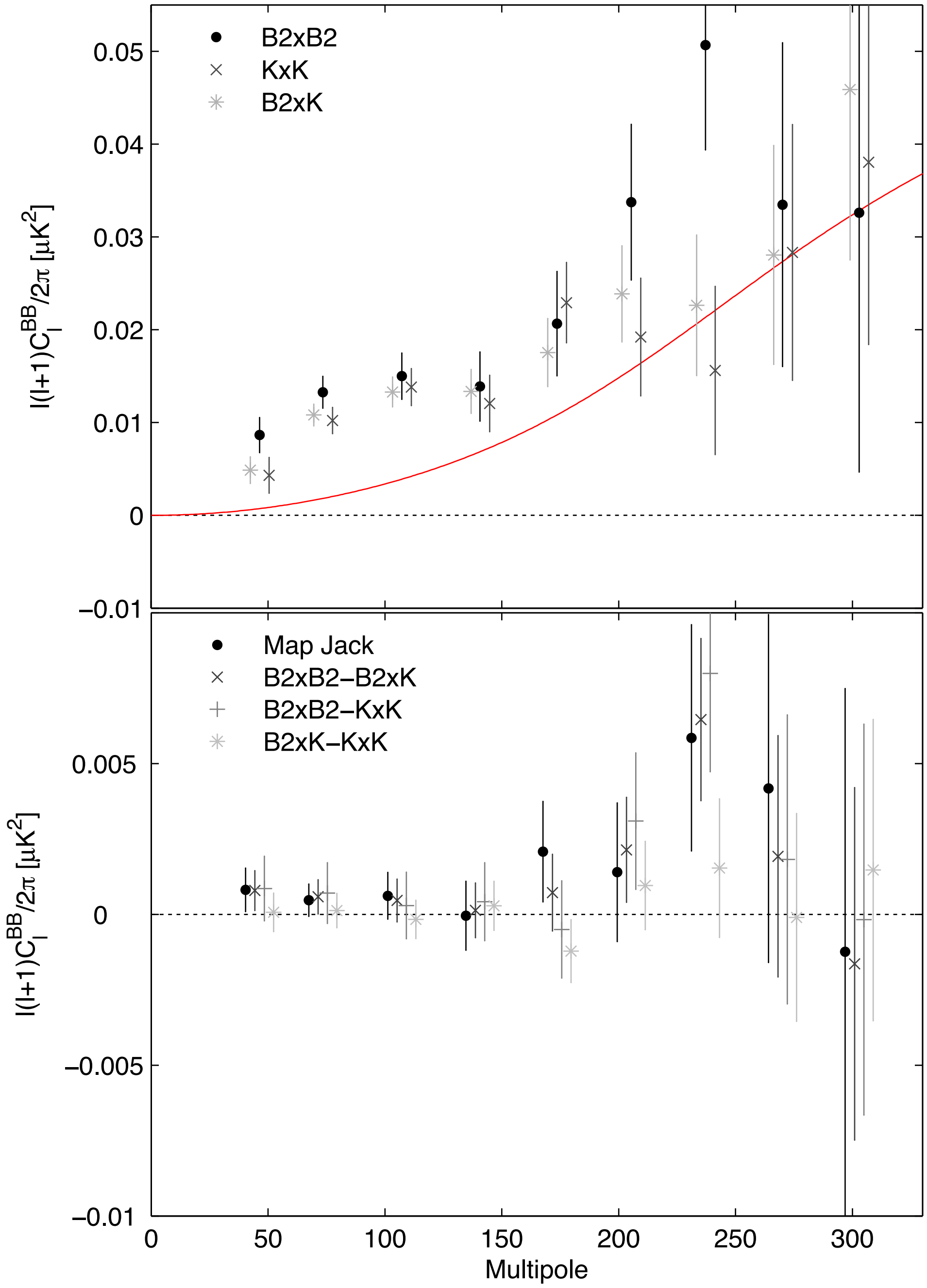

Figure 5.6: *Upper:* Comparison of the *Keck Array BB* auto spectrum, the BICEP2 auto spectrum, and the cross-spectrum taken between the two. The error bars are the standard deviation of the lensed-ΛCDM+noise simulations and are not appropriate for comparison of the data values. (For clarity the *Keck Array* and cross-spectrum points are offset horizontally.) *Lower:* Four compatibility tests between the $B$-modes measured by BICEP2 and *Keck Array*. The "map jack" takes the difference of the $Q$ and $U$ maps, divides by a factor of two, and calculates the $BB$ spectrum. The other three sets of points are the differences of the spectra shown in the upper panel divided by a factor of four. In each case the error bars are the standard deviation of the pairwise differences of signal+noise simulations that share common input skies—comparison of each set of these points (individually) with null is an appropriate test of the compatibility of the experiments—see text for details.

Table 5.2: BICEP2/*Keck Array* compatibility test PTE values from $\chi^2$ and $\chi$-like (sum of deviation) tests

| Jackknife | Bandpowers 1–5 $\chi^2$ | Bandpowers 1–9 $\chi^2$ | Bandpowers 1–5 $\chi$ | Bandpowers 1–9 $\chi$ |
|---|---|---|---|---|
| Map jackknife | | | | |
| EE | 0.034 | 0.048 | 0.106 | 0.028 |
| BB | 0.561 | 0.695 | 0.054 | 0.018 |
| EB | 0.741 | 0.754 | 0.405 | 0.651 |
| Spectral jackknife B2-cross | | | | |
| EE | 0.112 | 0.092 | 0.068 | 0.078 |
| BB | 0.687 | 0.387 | 0.052 | 0.008 |
| EB | 0.555 | 0.224 | 0.212 | 0.234 |
| Spectral jackknife B2-Keck | | | | |
| EE | 0.138 | 0.128 | 0.066 | 0.126 |
| BB | 0.920 | 0.485 | 0.200 | 0.022 |
| EB | 0.511 | 0.214 | 0.210 | 0.200 |
| Spectral jackknife cross-Keck | | | | |
| EE | 0.176 | 0.204 | 0.074 | 0.202 |
| BB | 0.880 | 0.966 | 0.643 | 0.435 |
| EB | 0.361 | 0.437 | 0.443 | 0.188 |

Inasmuch as the two experiments are consistent with each other and measuring the same sky at the same spectral band, their accumulation quantities can be combined to average maps, which is equivalent to a noise weighted combination of the maps. This results in $Q$ and $U$ maps that have a depth of 57 nK deg (3.4 $\mu$K arcmin) over an effective area of 400 square degrees for an equivalent survey weight of 248000 $\mu\mathrm{K}^{-2}$ (see Table 5.1).

The observation regions and strategies are sufficiently similar that it is found empirically using simulations that the purification matrix of either experiment delivers adequate $B$-mode purity when applied to the combined map (with contamination equivalent to $r < 10^{-3}$).

The final $BB$ spectrum is shown in Figure 5.7 and is inconsistent with the lensed-ΛCDM expectation at $> 6\sigma$ (for either bandpowers 1–5 or 1–9). The lensed-ΛCDM+noise error bars as plotted are approximately a factor two smaller than those of the previous BICEP2 only results—saturation on the (small) sample variance of the lensing component is occurring—the noise component is a factor 2.3 times smaller. All the spectra (including $TT$, $EE$ etc.) are available for download at `http://bicepkeck.org/` together with the ancillary data, noise information, etc., required to use them.

## 5.4 Combination with *Planck*

The BICEP2/*Keck Array* detection of excess $BB$ power above lensed-ΛCDM can be compared to *Planck* data at different observing frequencies. A joint analysis of the two data sets is presented in BKP [10].

In order to facilitate comparison, we prepare "Planck as seen by BICEP2/*Keck Array*" maps. In the first step we use the `anafast`, `alteralm`, and `synfast` routines from the `HEALPix` package [30] to resmooth the Planck maps with the BICEP2/Keck beam profile, assuming azimuthal symmetry of the beam. The coordinate rotation from Galactic to celestial coordinates of the $T$, $Q$, and $U$ maps is performed using the `alteralm` routine in the `HEALPix` package. The sign of the Stokes $U$ map is flipped to convert from the `HEALPix` to the IAU polarization convention, as noted in Section 3.4. Next we multiply these by the observation matrix of Section 3.6 to produce maps that include the filtering of modes occurring in the data

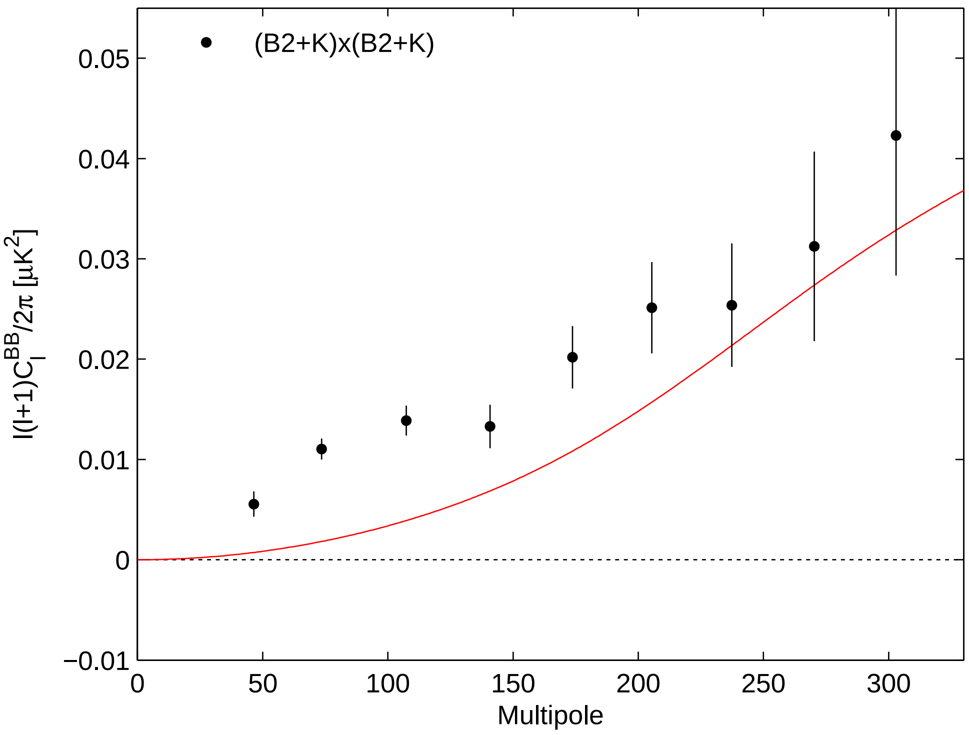

Figure 5.7: The $BB$ power spectrum of combined Bicep2 and *Keck Array* 150 GHz maps. The error bars are the standard deviation of the lensed-ΛCDM+noise simulations and hence contain no sample variance on any additional signal component.

processing pipeline.

Figure 5.8 shows the resmoothed *Planck* 353 GHz $T/Q/U$ maps before and after filtering. In both cases the Bicep2/*Keck Array* inverse variance apodization mask has been applied. This figure emphasizes the need to account for the filtering before any comparison of maps is attempted, either qualitative or quantitative.

cross-spectra are formed between the combined Bicep2/*Keck Array* 150 GHz map and each of the polarized *Planck* maps. All of the cross-spectra with *Planck* 353 GHz are shown in Figure 5.9, and $EE$ and $BB$ cross-spectra with all of the *Planck* polarized channels are shown in Figure 5.10. The temperature and $E$-mode cross-spectra are broadly consistent with the lensed-ΛCDM model, indicating that the CMB is the dominant source of degree angular scale power in the Bicep2/*Keck Array* field, both in intensity and in polarization, over all measured frequency channels. A modest excess in $TT$ and $EE$ between Bicep2/*Keck Array* and *Planck* 353 GHz is observed, presumably due to a Galactic dust foreground that is brighter

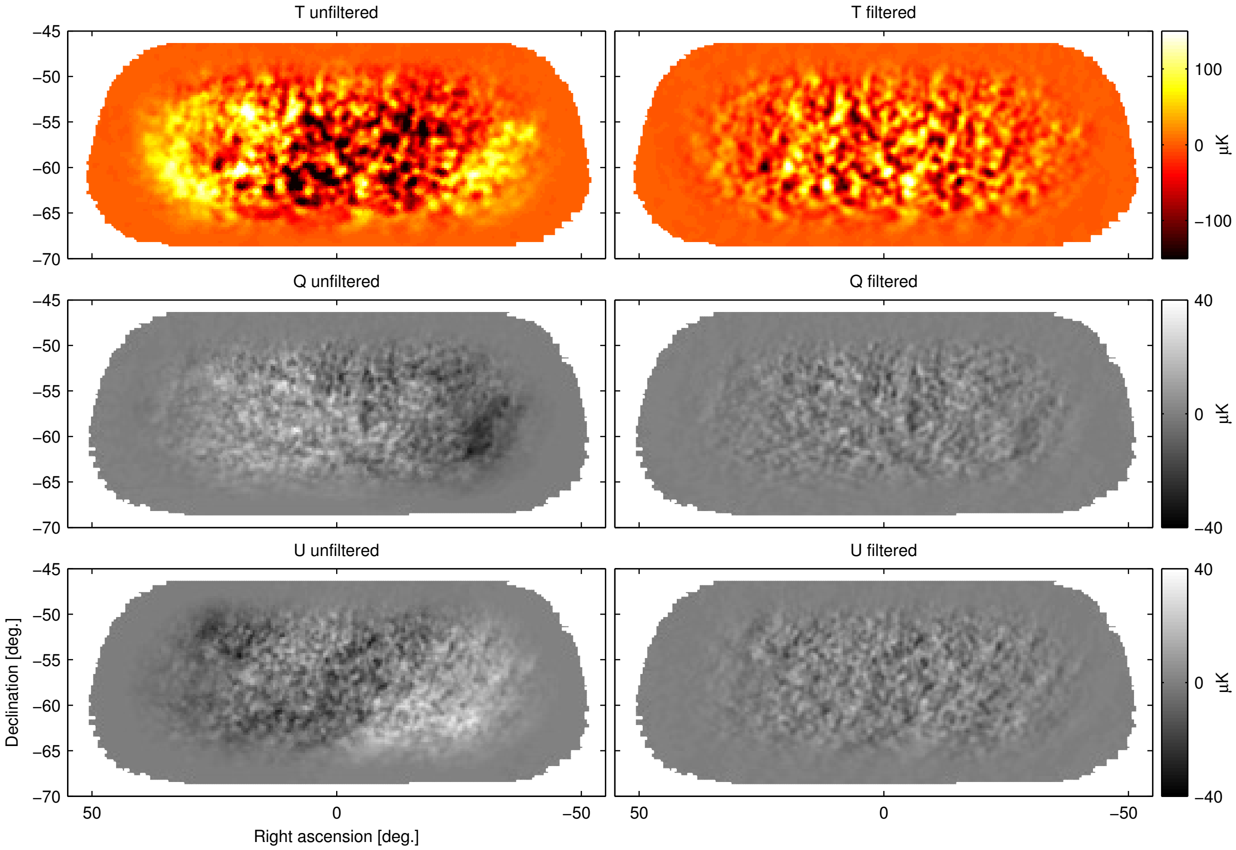

Figure 5.8: *Planck* 353 GHz $T$, $Q$, and $U$ maps before (left) and after (right) the application of Bicep2/*Keck Array* filtering. In both cases the maps have been multiplied by the Bicep2/*Keck Array* apodization mask. The *Planck* maps are presmoothed to the Bicep2/*Keck Array* beam profile and have the mean value subtracted. The filtering, in particular the third order polynomial subtraction to suppress atmospheric pickup, removes large-angular scale signal along the Bicep2/*Keck Array* scanning direction (parallel to the right ascension direction in the maps here).

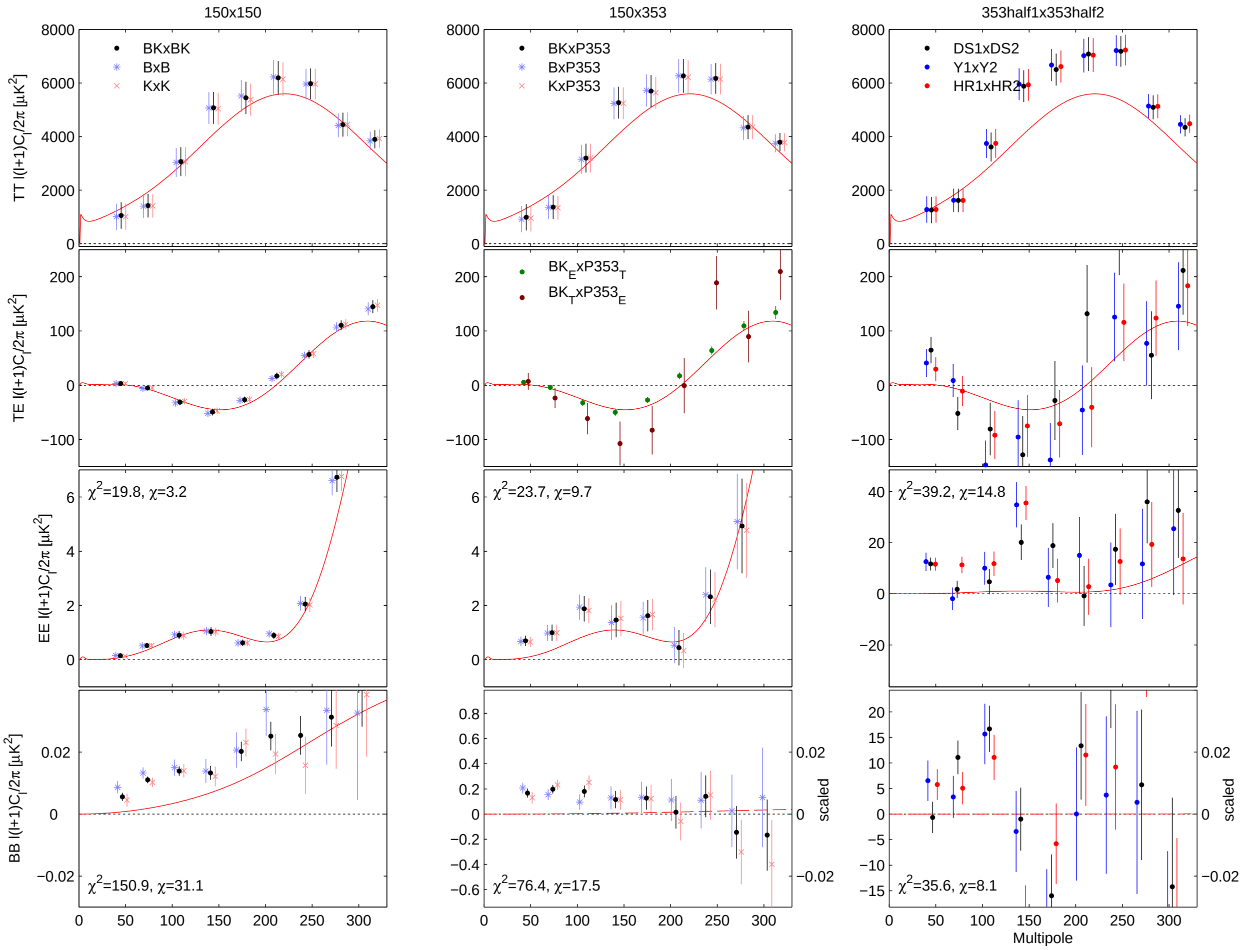

Figure 5.9: Single- and cross-frequency spectra between Bicep2/*Keck Array* maps at 150 GHz and *Planck* maps at 353 GHz. The left column shows single-frequency spectra of the Bicep2, *Keck Array*, and combined Bicep2/*Keck Array* maps. The Bicep2 spectra are identical to those in BK–I, while the *Keck Array* and combined are as given in BK–V. The center column shows cross-frequency spectra between Bicep2/*Keck Array* maps and *Planck* 353 GHz maps. The right column shows *Planck* 353 GHz data-split cross-spectra. In all cases the error bars are the standard deviations of lensed-ΛCDM+noise simulations and hence contain no sample variance on any other component. For $EE$ and $BB$ the $\chi^2$ and $\chi$ (sum of deviations) versus lensed-ΛCDM for the nine bandpowers shown is marked at upper/lower left (for the combined Bicep2/*Keck Array* points and DS1×DS2). In the bottom row (for $BB$) the center and right panels have a scaling applied such that signal from dust with the fiducial frequency spectrum would produce signal with the same apparent amplitude as in the 150 GHz panel on the left (as indicated by the right-side $y$-axes). We see from the significant excess apparent in the bottom center panel that a substantial amount of the signal detected at 150 GHz by Bicep2 and *Keck Array* indeed appears to be due to dust.

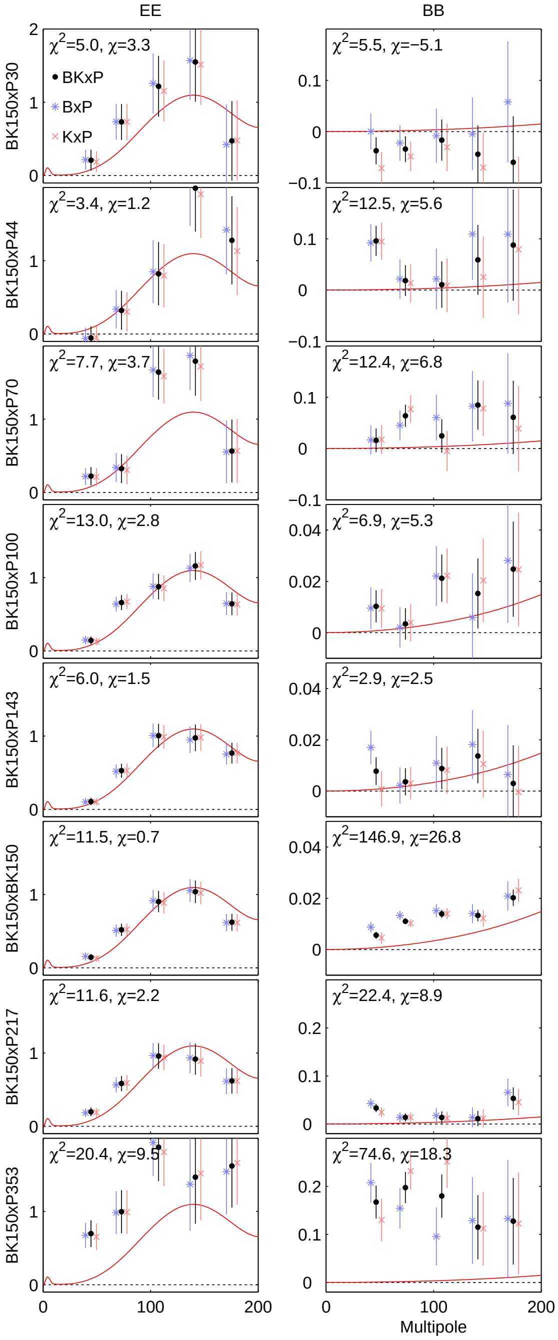

Figure 5.10: *EE* (left column) and *BB* (right column) cross-spectra between BICEP2/*Keck Array* maps and all of the polarized frequencies of *Planck*. In all cases the quantity plotted is $\frac{\ell(\ell+1)C_\ell}{2\pi}$ in units of $\mu K^2_{\rm CMB}$. The error bars are the standard deviations of lensed-ΛCDM+noise simulations and hence contain no sample variance on any other component. Also note that the $y$-axis scales differ from panel to panel in the right column. The $\chi^2$ and $\chi$ (sum of deviations) versus lensed-ΛCDM for the five bandpowers shown is marked at upper left. There are no additional strong detections of deviation from lensed-ΛCDM over those already shown in Figure 5.9, although BK150×P217 shows some evidence of excess.

at high frequency. The $B$-mode cross-spectra with low frequency *Planck* data are mostly consistent with noise and set an upper limit on the level of $BB$ power from polarized Galactic synchrotron radiation in the BICEP2/*Keck Array* field. The $B$-mode cross-spectra with the 217 GHz and 353 GHz *Planck* data show an excess above the lensed-ΛCDM expectation, also presumably due in large part to Galactic dust.

## 5.5 Dust model

The extrapolation of polarized Galactic dust observed at high frequency to the BICEP2/*Keck Array* 150 GHz band requires assumptions about the spectral behavior of the dust. The description and motivation for the form of the models is given in BKP [10] and is copied below.

Figure 2 of *Planck* Int. XXX [61] shows that the dust $BB$ (and $EE$) angular power spectra are well fit by a simple power law $\mathcal{D}_\ell \propto \ell^{-0.42}$ when averaging over large regions of sky. Section 5.2 of the same paper states that there is no evidence for departure from this behavior for 1% sky patches, although the signal-to-noise ratio is low for some regions. Presumably we expect greater fluctuation from the mean behavior than would be expected for a Gaussian random field.

The spectral energy distribution (SED) of dust polarization was measured in *Planck* Int. XXII [60] for 400 patches with 10 radius at intermediate Galactic latitudes. The SED is well fit by a modified blackbody spectrum with $T_\mathrm{d} = 19.6\,\mathrm{K}$ and $\beta_\mathrm{d} = 1.59 \pm 0.17$, where the dust temperature is obtained from a fit to the SED of total intensity, and the uncertainty on the spectral index represents the $1\sigma$ dispersion of the individual patch measurements. The uncertainty is an upper limit, since some fluctuation is due to noise rather than real variation on the sky. This SED is confirmed to be a good match to data when averaging over 24% of the cleanest high latitude sky in Figure 6 of *Planck* Int. XXX.

As an extension of the simplest lensed-ΛCDM paradigm, we initially consider a two component model of IGW with amplitude $r$, plus dust with amplitude $A_\mathrm{d}$. The dust amplitude $A_\mathrm{d}$ is the value of 353 GHz power $\mathcal{D}_\ell$ at $\ell = 80$ in CMB power units $\mu\mathrm{K}^2_{\mathrm{CMB}}$. The dust is modeled as a power law $\mathcal{D}_\ell \propto \ell^{-0.42}$, with free amplitude $A_\mathrm{d}$ and scaling with frequency according to the modified blackbody model. Here we assume that the spectral index of the tensor modes ($n_\mathrm{t}$) is zero, and a scalar pivot scale of $0.05\,\mathrm{Mpc}^{-1}$. The flat spectral index simplifies the scaling of tensor power to be linear in $r$.

A tight Gaussian prior $\beta_\mathrm{d} = 1.59 \pm 0.11$ is imposed, since this parameter is not well constrained from these data alone, but does appear to be stable across the sky. For the frequency range of interest here variations in the two parameters of the modified blackbody are highly degenerate and the choice is made to hold $T_\mathrm{d}$ fixed while allowing $\beta_\mathrm{d}$ to be free. The prior assumes that the SED of dust polarization at intermediate latitudes [60] applies to the BICEP2/*Keck Array* field, where the signal-to-noise ratio of the *Planck* data is too low to determine it directly. From dust astrophysics, we expect variations of the dust SED in intensity and polarization to be correlated [50]. We thus tested our assumption by measuring the spectral index of the dust total intensity in the BICEP2/*Keck Array* field using the template fitting analysis described in *Planck* Int. XVII [59], and find the same value. The uncertainty on $\beta_\mathrm{d}$ is scaled from the dispersion of spectral indices at intermediate Galactic latitudes in *Planck* Int. XXII [60], as explained in *Planck* Int. XXX.

## 5.6 Likelihood calculation

BKP uses a likelihood framework for estimating the contributions of signal components to the observed bandpowers. The likelihood calculation is based on the Hamimeche–Lewis (HL) approximation [31], and its implementation is similar to its use in BICEP1 [6]. The baseline analysis uses only data from $\mathcal{D}_{\ell'}^{BB}$ in bandpowers 1–5 ($20 < \ell < 200$) coming from BICEP2/*Keck Array* 150 GHz and *Planck* 217 and 353 GHz to focus on the degeneracy between Galactic dust and IGW signals. In each $\ell$ bin, we compute an observed bandpower matrix

$$\boldsymbol{\mathcal{D}}_{\ell'}^{\mathrm{obs}} = \begin{pmatrix} \mathcal{D}_{\ell'}^{\mathrm{BKxBK}} & \mathcal{D}_{\ell'}^{\mathrm{BKxP217}} & \mathcal{D}_{\ell'}^{\mathrm{BKxP353}} \\ \mathcal{D}_{\ell'}^{\mathrm{BKxP217}} & \mathcal{D}_{\ell'}^{\mathrm{P217xP217}} & \mathcal{D}_{\ell'}^{\mathrm{P217xP353}} \\ \mathcal{D}_{\ell'}^{\mathrm{BKxP353}} & \mathcal{D}_{\ell'}^{\mathrm{P217xP353}} & \mathcal{D}_{\ell'}^{\mathrm{P353xP353}} \end{pmatrix} \tag{5.4}$$

For the *Planck* single-frequency case, the diagonal elements are the internal cross-spectrum of detector-sets (DS1×DS2), following *Planck* Int. XXX, instead of the autospectra.

The theoretical bandpower matrices $\boldsymbol{\mathcal{D}}_{\ell'}$ are evaluated for a range of models that contribute to $BB$ power through lensed-$\Lambda$CDM, Galactic dust, and IGW. We compute multi-dimensional grids of models explicitly and/or use `COSMOMC` [47] to sample the parameter space.

The HL formulation requires the choice of a single "fiducial model." The main analysis of BKP chose the fiducial model to be the lensed-$\Lambda$CDM+dust model with $r = 0$. At each grid point of the model space, we adjust the smaller observed bandpower matrices by

$$\mathbf{X}_{\ell'} = \mathrm{vecp}\left[(\boldsymbol{\mathcal{D}}^{\mathrm{f}}_{\ell'})^{\frac{1}{2}} g(\boldsymbol{\mathcal{D}}_{\ell'}^{-\frac{1}{2}} \boldsymbol{\mathcal{D}}^{\mathrm{obs}}_{\ell'} \boldsymbol{\mathcal{D}}_{\ell'}^{-\frac{1}{2}})(\boldsymbol{\mathcal{D}}^{\mathrm{f}}_{\ell'})^{\frac{1}{2}}\right] \tag{5.5}$$

where $\boldsymbol{\mathcal{D}}^{\mathrm{f}}_{\ell'}$ is the theoretical bandpower matrix of the fiducial model, $g(\mathbf{A})$ is a function that replaces the eigenvalues $\lambda$ of matrix $\mathbf{A}$ in the standard eigendecomposition with $\mathrm{sgn}\,(\lambda - 1)\sqrt{2(\lambda - \ln\lambda - 1)}$, and the function vecp($\mathbf{S}$) arranges the upper triangular elements of the symmetric matrix $\mathbf{S}$ into a column vector. The bandpower vectors are concatenated into a vector $\mathbf{X}$ with dimension 30. The full bandpower covariance matrix $\boldsymbol{\mathcal{M}}$ is determined for the fiducial model only. In the HL approximation, the log-likelihood of the theoretical bandpowers $\{\boldsymbol{\mathcal{D}}_{\ell'}\}$ for a model given the observation $\{\boldsymbol{\mathcal{D}}^{\mathrm{obs}}_{\ell'}\}$ is

$$-2\ln\mathcal{L}(\{\boldsymbol{\mathcal{D}}_{\ell'}\}|\{\boldsymbol{\mathcal{D}}^{\mathrm{obs}}_{\ell'}\}) = \mathbf{X}^{\mathrm{T}}\boldsymbol{\mathcal{M}}^{-1}\mathbf{X} \tag{5.6}$$

An advantage of the HL approximation is that $(\boldsymbol{\mathcal{D}}^{\mathrm{f}}_{\ell'})^{\frac{1}{2}}$ and $\boldsymbol{\mathcal{M}}^{-1}$ only need to be computed once for the fiducial model and not for other grid points in the model parameter space. A public data release of $\boldsymbol{\mathcal{M}}^{-1}$ along with the real bandpowers, noise bias, and bandpower window functions are enough for anyone else to replicate the likelihood calculation. The evaluation of $g(\boldsymbol{\mathcal{D}}_{\ell'}^{-\frac{1}{2}} \boldsymbol{\mathcal{D}}^{\mathrm{obs}}_{\ell'} \boldsymbol{\mathcal{D}}_{\ell'}^{-\frac{1}{2}})$ involves solving the eigenvalue problem for smaller matrices.

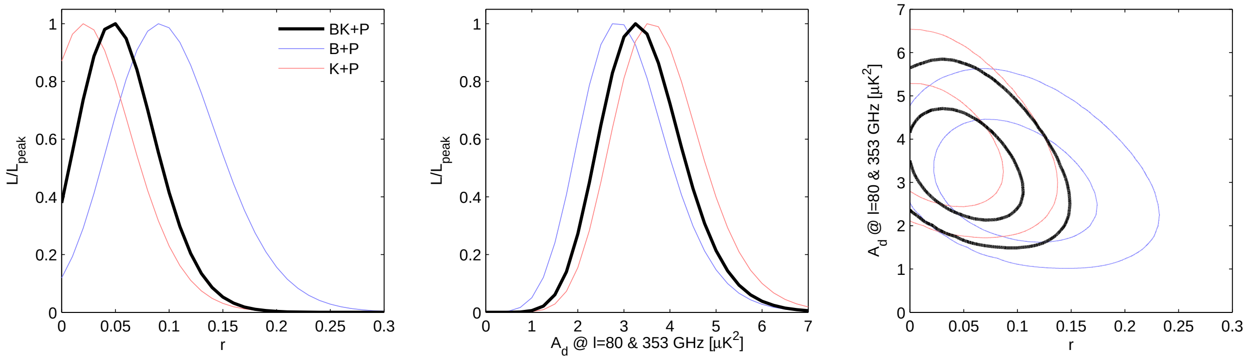

Figure 5.11: Likelihood results from a basic lensed-ΛCDM+$r$+dust model, fitting $BB$ auto- and cross-spectra taken between maps at 150 GHz, 217, and 353 GHz. The 217 and 353 GHz maps come from *Planck*. The primary results (heavy black) use the 150 GHz combined maps from BICEP2/*Keck Array*. Alternate curves (light blue and red) show how the results vary when the BICEP2 and *Keck Array* only maps are used. In all cases a Gaussian prior is placed on the dust frequency spectrum parameter $\beta_d = 1.59 \pm 0.11$. In the right panel the two-dimensional contours enclose 68% and 95% of the total likelihood.

## 5.7 Parameter constraints

Figure 5.11 shows the HL likelihood results using the lensed-ΛCDM+dust fiducial model and $BB$ bandpowers 1–5 of BICEP2/*Keck Array* 150 GHz data and *Planck* 217 and 353 GHz data. We see that the BICEP2 data produce an $r$ likelihood that peaks higher than that for the *Keck Array* data. This is because for $\ell < 120$ the auto-spectrum B150×B150 is higher than for K150×K150, while the cross-spectrum B150×P353 is lower than K150×P353 (see Figure 5.9). However, recall that both pairs of spectra B150×B150/K150×K150 and B150×P353/K150×P353 have been shown to be consistent within noise fluctuation (see Section 5.3). Given the consistency between the two experiments, the combined result gives the best available measurement of the sky.

The combined curves (BK+P) in the left and center panels of Figure 5.11 yield the following results: $r = 0.048^{+0.035}_{-0.032}$, $r < 0.12$ at 95% confidence, and $A_d = 3.3^{+0.9}_{-0.8}$. For $r$ the zero-to-peak likelihood ratio is 0.38. Taking $\frac{1}{2}\left(1 - f\left(-2\log\frac{\mathcal{L}_0}{\mathcal{L}_{\rm peak}}\right)\right)$, where $f$ is the $\chi^2$ cdf (for one degree of freedom), we estimate that the probability to get a number smaller than this is 8% if in fact $r = 0$. For $A_d$ the zero-to-peak ratio is $1.8 \times 10^{-6}$ corresponding to a smaller-than probability of $1.4 \times 10^{-7}$, and a $5.1\sigma$ detection of dust power.

The maximum likelihood model on the grid has parameters $r = 0.05$, $A_d = 3.30\,\mu\text{K}^2$ (and $\beta_d = 1.6$). Computing the bandpower covariance matrix for this model, we obtain a $\chi^2$ of 40.9. Using 28 degrees of

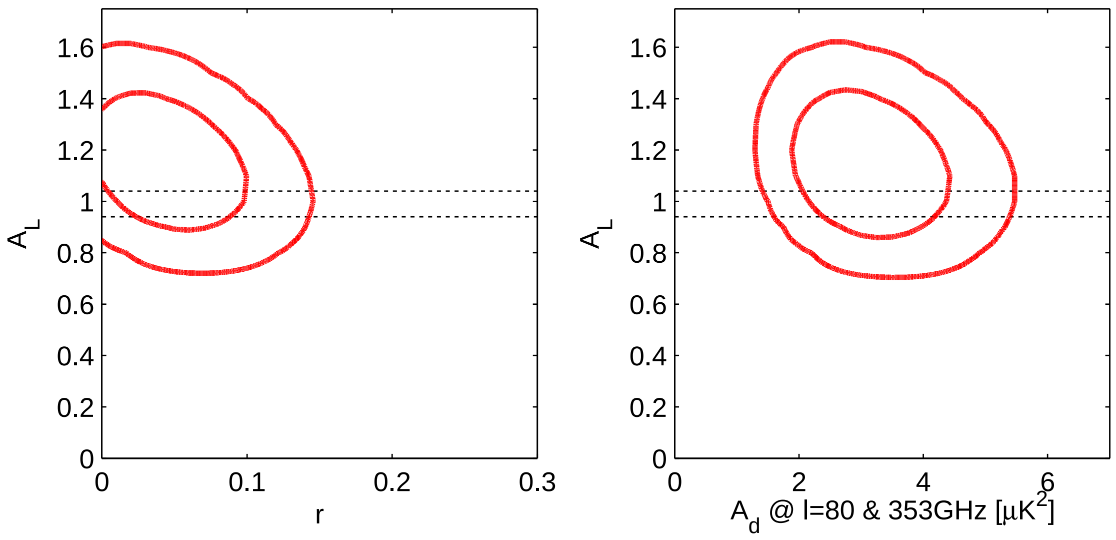

Figure 5.12: Likelihood results for a fit allowing the lensing scale factor $A_{\rm L}$ to float freely and using all nine bandpowers. Marginalizing over $r$ and $A_{\rm d}$, we find that $A_{\rm L} = 1.13 \pm 0.18$ and $A_{\rm L} = 0$ is ruled out with $7.0\,\sigma$ significance.

freedom—5 bandpowers times 6 spectra, minus 2 fit parameters (since $\beta_{\rm d}$ is not really free)—gives a PTE of 0.06. The largest contributions to $\chi^2$ come from the P353×P353 spectrum, shown in the lower right panel of Figure 5.9.

Alternative data selections extend the analysis to include $EE$ power, all nine $\ell$ bins, or more *Planck* frequency channels. The additional data, which are dominated by lensed-ΛCDM or noise, do not strongly affect the main result. See BKP for discussion of the different analysis methods and their consistency.

In the fiducial analysis the amplitude of the lensing effect is held fixed at the ΛCDM expectation ($A_{\rm L} = 1$). Using their own and other data, the *Planck* Collaboration quote a limit on the amplitude of the lensing effect versus the ΛCDM expectation of $A_{\rm L} = 0.99 \pm 0.05$ [58]. Allowing $A_{\rm L}$ to float freely, and using all nine bandpowers, we obtain the results shown in Fig. 5.12—there is only weak degeneracy between $A_{\rm L}$ and both $r$ and $A_{\rm d}$. Marginalizing over $r$ and $A_{\rm d}$ we find $A_{\rm L} = 1.13 \pm 0.18$ with a likelihood ratio between zero and peak of $3 \times 10^{-11}$. This corresponds to a smaller-than probability of $2 \times 10^{-12}$, equivalent to a $7.0\,\sigma$ detection of lensing in the $BB$ spectrum. We note that this is the most significant direct measurement of lensing in $B$-mode polarization to date.

## 5.8 Component-separated bandpowers

The results presented above and in BKP use all of the bandpowers to derive the likelihood of $r$ and $A_\mathrm{d}$. An interesting component separation repeats this process but using only a single $\ell$ bin at a time. The data used here for the component separation are all publicly available.

The model contains just two signal types, CMB and dust, although it can be extended to include more components. It is simplified to discard information about the $\ell$ dependence of the signals. The CMB component therefore has only one parameter, namely its power level in $\mu\mathrm{K}^2$. It does not matter whether the CMB signal is from lensing or from IGW. The dust component has three parameters: power level at 150 GHz, greybody temperature, and spectral index. The temperature is fixed at 19.6 K, and the spectral index is given a Gaussian prior $\beta_\mathrm{d} = 1.59 \pm 0.11$ as in the fiducial analysis. The pivot frequency for the dust power is set to 150 GHz because the goal is to estimate the effect of dust in the BICEP2/*Keck Array* 150 GHz bandpowers. The data set used here is BICEP2/*Keck Array* 150 GHz, *Planck* 217 GHz, and *Planck* 353 GHz. There are six $BB$ bandpowers at each $\ell$ bin to fit for three parameters (but with additional prior information for the spectral index).

Since the likelihood framework uses the HL approximation for the bandpower likelihoods, it is necessary to choose a fiducial model for each $\ell$ bin. This is done in two iterations. In the first iteration, the fiducial model is set to have CMB power equal to the observed 150 GHz $BB$ bandpower, and the dust power equal to the 353 GHz $BB$ bandpower (but forcing both values to be positive). The likelihood is calculated using that first fiducial model. In the second iteration, the fiducial model is updated to be the maximum likelihood model derived from the first iteration.

The likelihoods are evaluated on a grid that assumes a flat prior on $\mathcal{D}_\ell^{BB}$ for the two components. For dust, the grid for $A_{\mathrm{d},150}$ ranges from 0 to 0.04 $\mu\mathrm{K}^2$ in all $\ell$ bins. For CMB, the grid for $A_\mathrm{CMB}$ goes up to 0.03 $\mu\mathrm{K}^2$ in $\ell$ bins 1–4, 0.05 $\mu\mathrm{K}^2$ in bin 5, 0.10 $\mu\mathrm{K}^2$ in bins 6–8, and 0.20 $\mu\mathrm{K}^2$ in bin 9. The Gaussian prior for $\beta_\mathrm{d}$ is evaluated between 1.15 and 2.03.

The 2D likelihoods for all nine $\ell$ bins and the 1D marginal likelihoods of CMB and dust are shown in Appendix C. Component-separated bandpowers are given by the marginalized likelihoods of the two

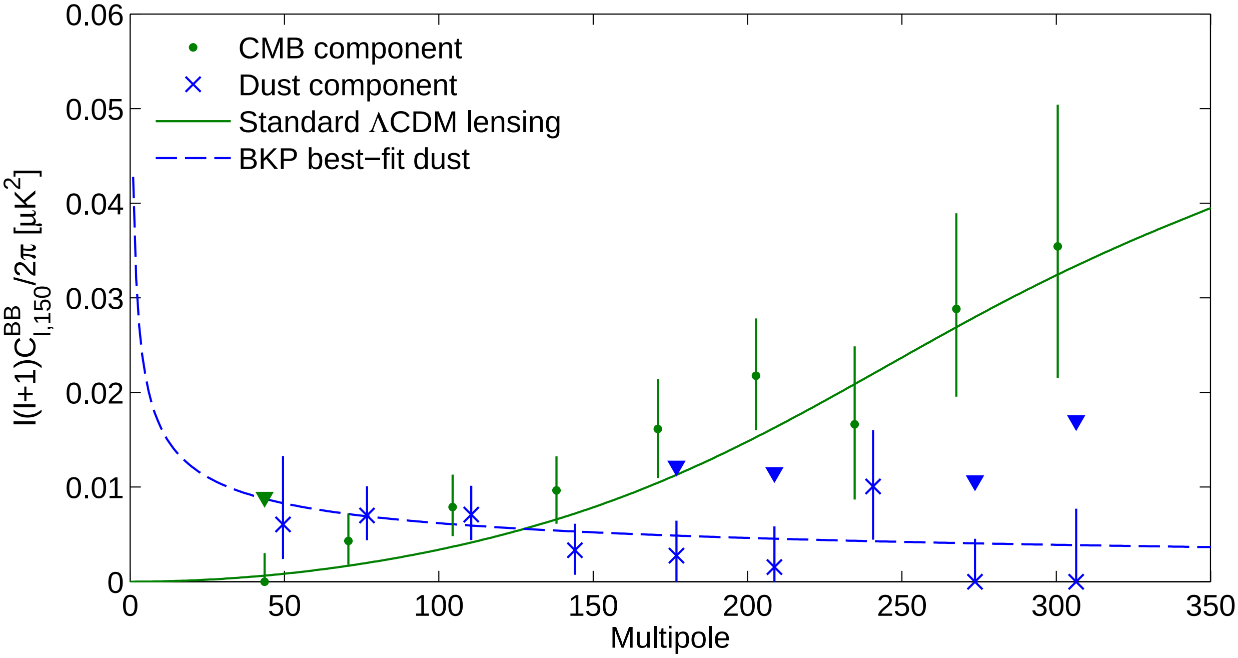

Figure 5.13: Component-separated $BB$ bandpowers using the HL likelihood analysis on individual $\ell$ bins. The method is described further in Section 5.8. The error bars are the $1\sigma$ credible intervals of the marginal likelihoods in Appendix C. If the credible interval includes zero, then the 95% upper limit is also shown. The CMB and dust points have been shifted apart in $\ell$ for clarity. The solid green line is standard ΛCDM lensing $BB$ power. The solid blue line corresponds to $A_\mathrm{d} = 3.3\mu\mathrm{K}^2$ at 353 GHz (with $\beta = 1.59$). The theory curves are drawn only for reference – they are not directly derived from the data points. Data values on this plot are listed in Table C.1 for the CMB and Table C.2 for Galactic dust.

components at each $\ell$ bin. Figure 5.13 shows maximum likelihood values for the CMB and dust power at 150 GHz, along with $1\sigma$ credible intervals derived from the marginalized likelihood. The error bars are not generally symmetric and the allowed region is constrained to be non-negative. For bandpowers within $1\sigma$ of zero, Figure 5.13 also shows the 95% upper limit. It is important to note that the likelihoods ignore the correlation between different $\ell$ bins because they have been analyzed separately. The likelihood of the fiducial analysis in Figure 5.11 is the combination of the nine $\ell$ bins together with their correlation. Therefore this helps to visualize the results of the multicomponent analysis without invoking specific any specific theoretical model, apart from the assumptions about the frequency scaling of dust.

## 5.9 Conclusion

BICEP2/*Keck Array* has made the deepest map of CMB polarization to date. In combination with *Planck*, the data are found to be consistent with the lensed-ΛCDM model. An excess of power at low $\ell$ can be explained by a faint but non-negligible, polarized foreground signal from Galactic dust.

Forthcoming analysis of 95 and 230 GHz data will help to discriminate CMB from foregrounds at higher signal-to-noise. *Keck Array* has completed its first year of observation at 95 GHz. The preliminary 95 GHz maps shown in Figure 5.1 have achieved a depth of 126 nK deg (7.6 $\mu$K arcmin) and will soon help to constrain $r$ below the Galactic dust foreground. Figure 5.14 shows the sensitivity at $\ell \sim 80$ of the BKP analysis at the various frequency channels, and to this we add a prediction for the sensitivity of the *Keck Array* 95 GHz data collected in 2014. We see that with data already collected, we may be approaching the $r \leq 0.02$ lensing confusion limit that is the target of the BICEP2/*Keck Array* program.

We look forward to these upcoming results, as well as results from the many other cutting-edge experiments throughout cosmology. Primary data products from this thesis and the BK series of papers are all publicly available at `http://bicepkeck.org/`, and we encourage other experiments to combine our results with other data sets for the best constraints on cosmological parameters.

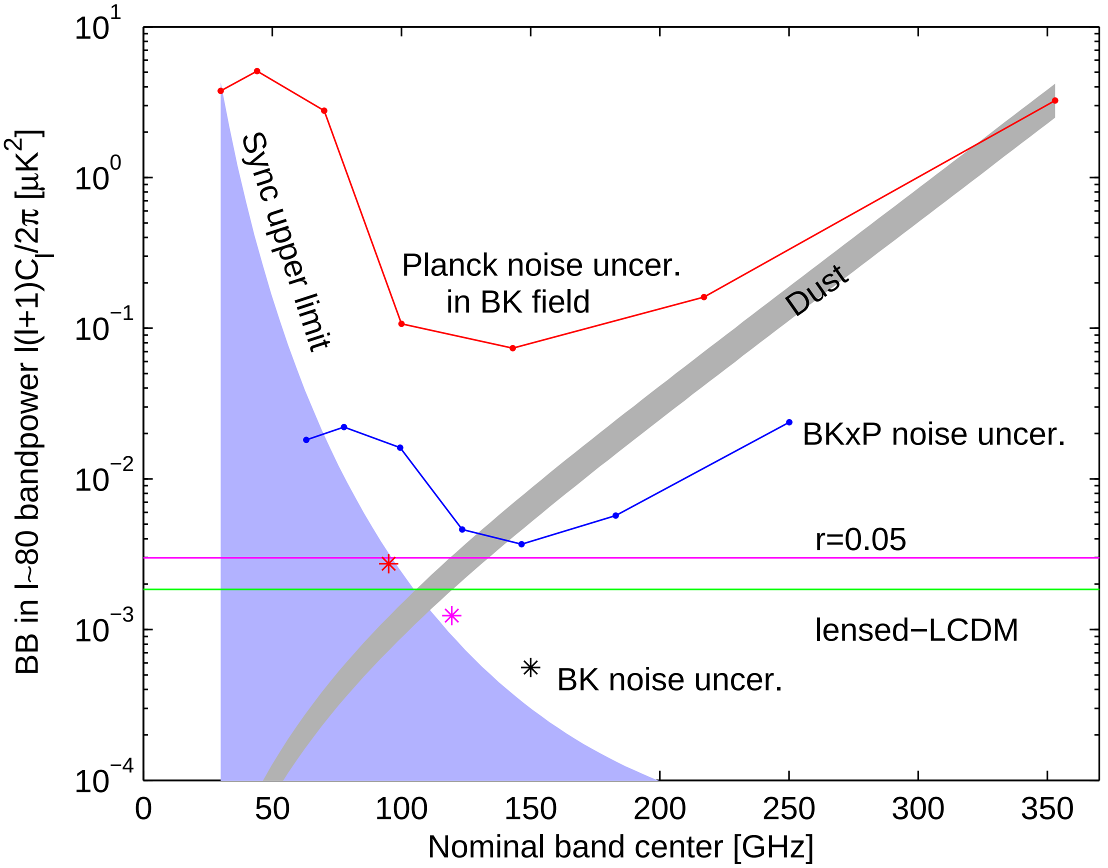

Figure 5.14: Expectation values, and uncertainties thereon, for the $\ell \sim 80$ $BB$ bandpower in the Bicep2/*Keck Array* field. The green and magenta lines correspond to the expected signal power of lensed-ΛCDM and $r = 0.05$. Since CMB units are used, the levels corresponding to these are flat with frequency. The grey band shows the best fit dust model (see Section 5.5) and the blue shaded region shows the allowed region for synchrotron (see BKP Section IIIC). The BK150 noise uncertainty is shown as a single black, starred point, and the noise uncertainties of the *Planck* single-frequency spectra evaluated in the Bicep2/*Keck Array* field are shown in red. The blue points show the noise uncertainty of the cross-spectra taken between BK150 and, from left to right, *Planck* 30, 44, 70, 100, 143, 217 & 353 GHz, and plotted at horizontal positions such that they can be compared vertically with the dust and sync curves. The red, starred point is a prediction of the sensitivity K95 based on the noise level in the maps using 2014 data (see Section 5.1), and the magenta, starred point is the predicted sensitivity of BK150×K95.

# Appendix A

# Accumulation quantities

Table A.1: Names and descriptions of data accumulation quantities

| Abstract quantity | Matlab analysis pipeline variable name | Description |
|---|---|---|
| $w_{ik}^T$ | `wsum` | Detector pair sum weight. BICEP2/*Keck Array* uses the inverse variance of a channel's $d_{\text{sum}}$ time stream across a scanset, common to all map pixels $i$ covered by the channel during the scanset. |
| $w_{ik}^P$ | `w` | Detector pair difference weight. BICEP2/*Keck Array* uses the inverse variance of a channel's $d_{\text{diff}}$ time stream across a scanset, common to all map pixels $i$ covered by the channel during the scanset. |
| $x_{ik}$ | `wz` | Weighted detector pair sum `wsum` $d_{\text{sum}}$ |
| $y_{ik}$ | `wcz` | Weighted, oriented detector pair difference `w` $\cos(2\psi)\, d_{\text{diff}}$ |
| $z_{ik}$ | `wsz` | Weighted, oriented detector pair difference `w` $\sin(2\psi)\, d_{\text{diff}}$ |
| $\frac{1}{4} w_{ik} \alpha_{ik}^2$ | `wcc` | Oriented weight `w` $\cos^2(2\psi)$ |
| $\frac{1}{4} w_{ik} \beta_{ik}^2$ | `wss` | Oriented weight `w` $\sin^2(2\psi)$ |
| $\frac{1}{4} w_{ik} \alpha_{ik} \beta_{ik}$ | `wcs` | Oriented weight `w` $\cos(2\psi)\sin(2\psi)$ |

Table A.2: Names and descriptions of noise accumulation quantities

| Abstract quantity | Matlab analysis pipeline variable name | Description |
|---|---|---|
| $\delta x_{ik}$ | Replaces `wz` | Weighted pair sum deviation $\texttt{wz} - \texttt{wsum}\,\overline{T}$ |
| $\delta y_{ik}$ | Replaces `wcz` | Weighted, oriented pair difference deviation $\texttt{wcz} - \texttt{wcc}\,\overline{Q} - \texttt{wcs}\,\overline{U}$ |
| $\delta z_{ik}$ | Replaces `wsz` | Weighted, oriented pair difference deviation $\texttt{wsz} - \texttt{wcs}\,\overline{Q} - \texttt{wss}\,\overline{U}$ |
| $\delta x_{ik}\delta x_{jk}$ | `wdzwdz` | Outer product of deviations in the map domain with various weights and polarization orientation information |
| $\delta x_{ik}\delta y_{jk}$ | `wdzwdcz` | |
| $\delta x_{ik}\delta z_{jk}$ | `wdzwdsz` | |
| $\delta y_{ik}\delta y_{jk}$ | `wdczwdcz` | |
| $\delta y_{ik}\delta z_{jk}$ | `wdczwdsz` | |
| $\delta z_{ik}\delta z_{jk}$ | `wdszwdsz` | |
| | `wwv` | Square of weight times the variance of the pair sum/difference time stream across a scanset. If the noise is stationary on timescales of a phase, then `wwv`, `wwccv`, `wwcsv`, and `wwssv` are similar to the diagonal elements $\delta x_{ik}\delta x_{ik}$, $\delta y_{ik}\delta y_{ik}$, $\delta y_{ik}\delta z_{ik}$, and $\delta y_{ik}\delta z_{ik}$ of the map domain. |
| | `wwccv` | |
| | `wwcsv` | |
| | `wwssv` | |

# Appendix B

# 2D bandpower window functions

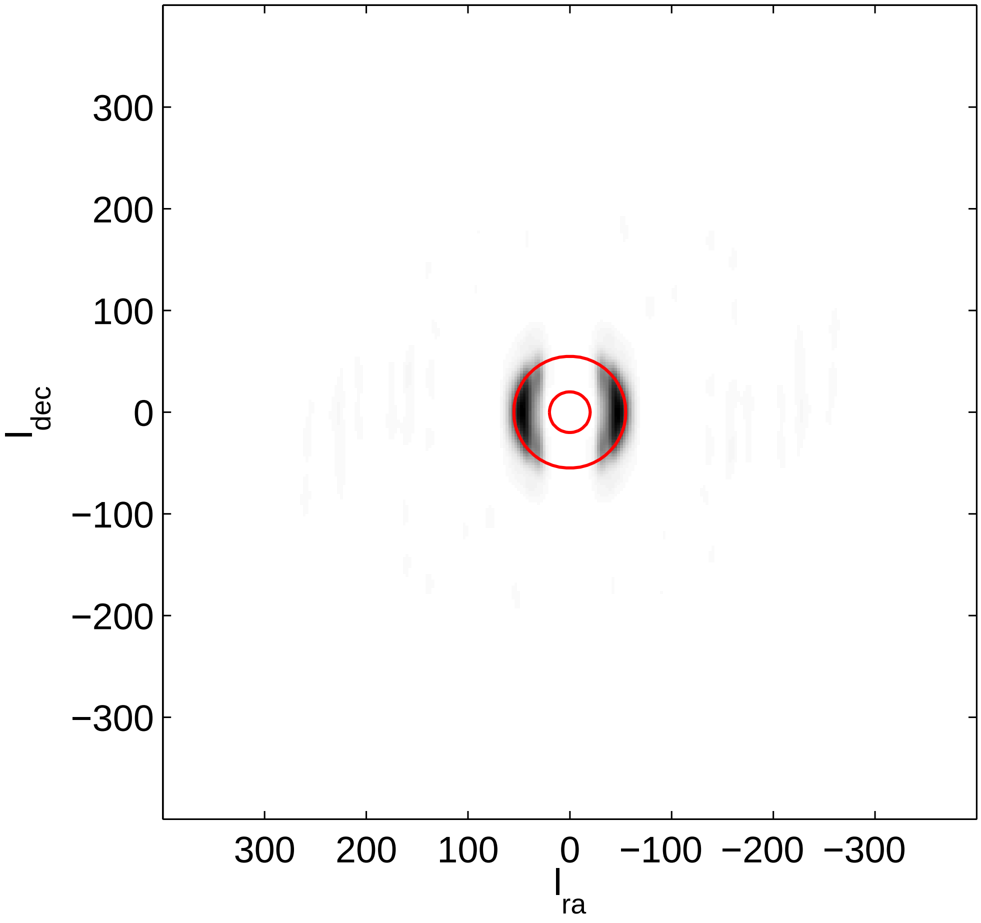

Figure B.1: 2D bandpower window function of the $\ell = 45.3$ bin for $BB$. The red circles are the $\ell$ of 21–55 bin edges. The $BB$ bandpower window function is derived using simulations at a single multipole containing no $E$-mode power and processed through the analysis pipeline, including matrix purification. The suppression of modes along $|\ell_{\rm ra}| \lesssim 40$ is the result of filtering the azimuth scans. The 2D bandpower window functions for $TT$ and $EE$ look qualitatively similar. See Section 4.2 for discussion.

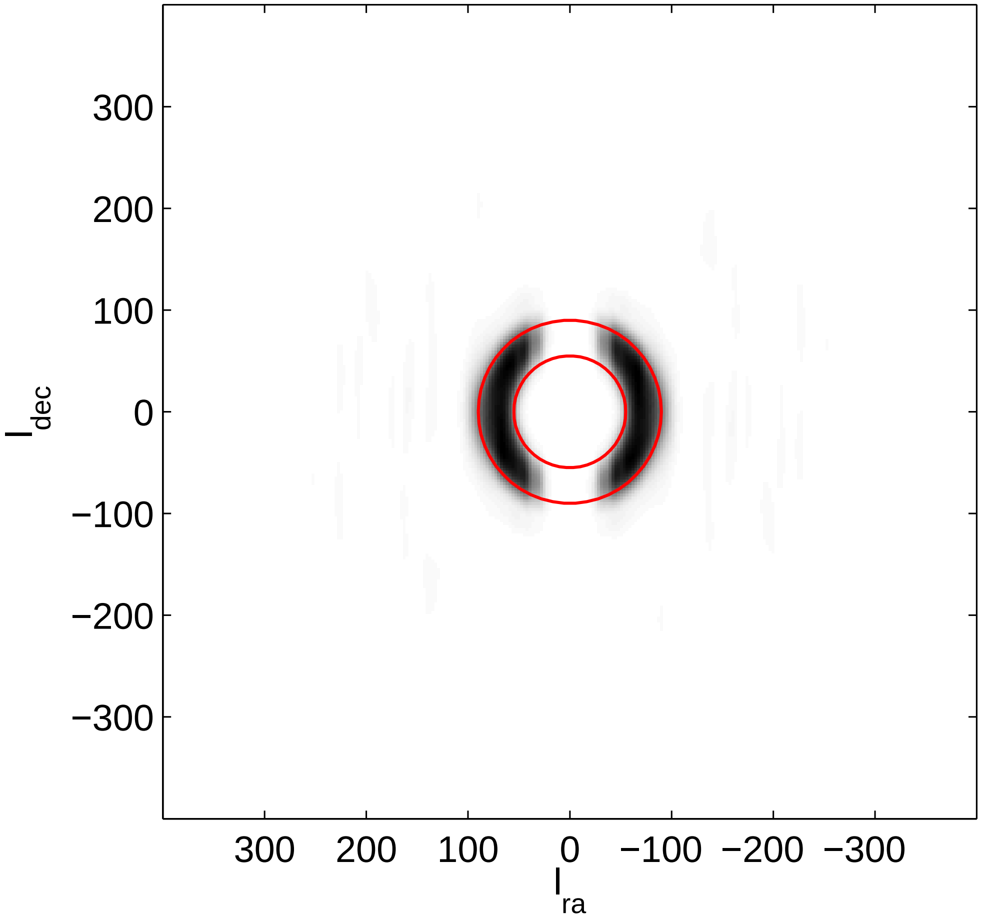

Figure B.2: 2D bandpower window function of the $\ell = 74.2$ bin for $BB$. The red circles are the $\ell$ of 56–90 bin edges. The $BB$ bandpower window function is derived using simulations at a single multipole containing no $E$-mode power and processed through the analysis pipeline, including matrix purification. The suppression of modes along $|\ell_{\rm ra}| \lesssim 40$ is the result of filtering the azimuth scans. The 2D bandpower window functions for $TT$ and $EE$ look qualitatively similar. See Section 4.2 for discussion.

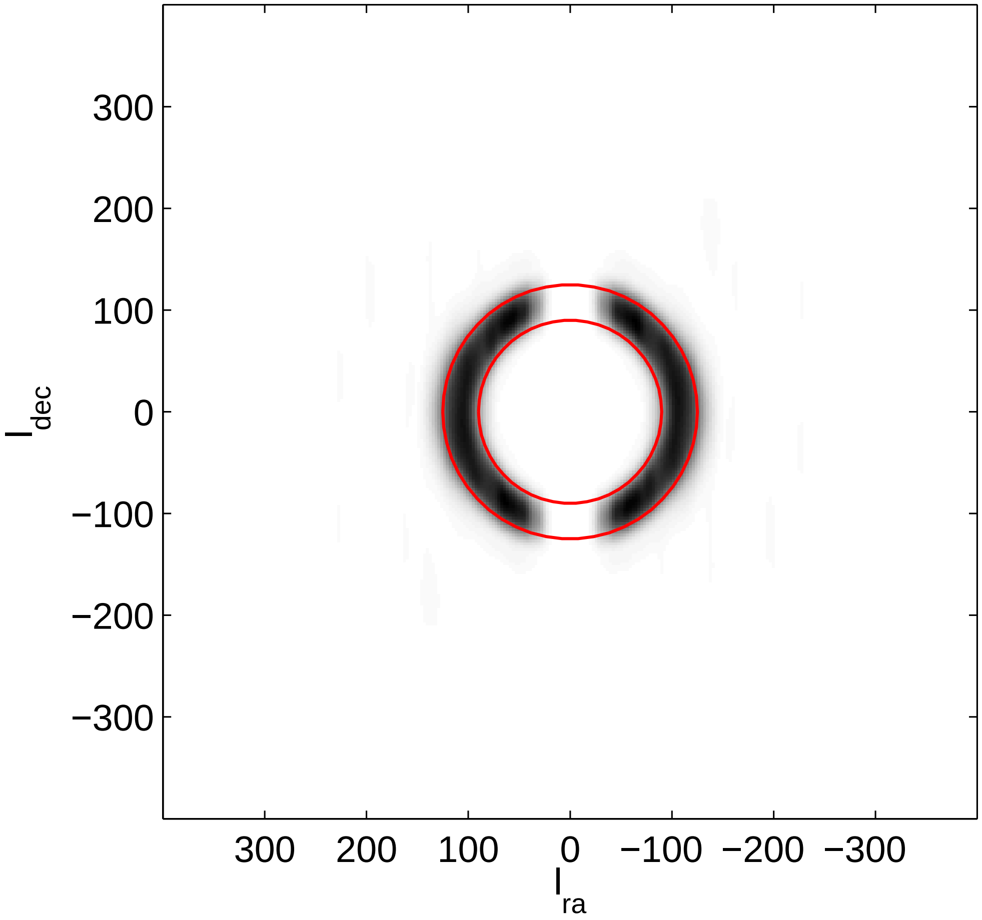

Figure B.3: 2D bandpower window function of the $\ell = 109.2$ bin for $BB$. The red circles are the $\ell$ of 91–125 bin edges. The $BB$ bandpower window function is derived using simulations at a single multipole containing no $E$-mode power and processed through the analysis pipeline, including matrix purification. The suppression of modes along $|\ell_{\mathrm{ra}}| \lesssim 40$ is the result of filtering the azimuth scans. The 2D bandpower window functions for $TT$ and $EE$ look qualitatively similar. See Section 4.2 for discussion.

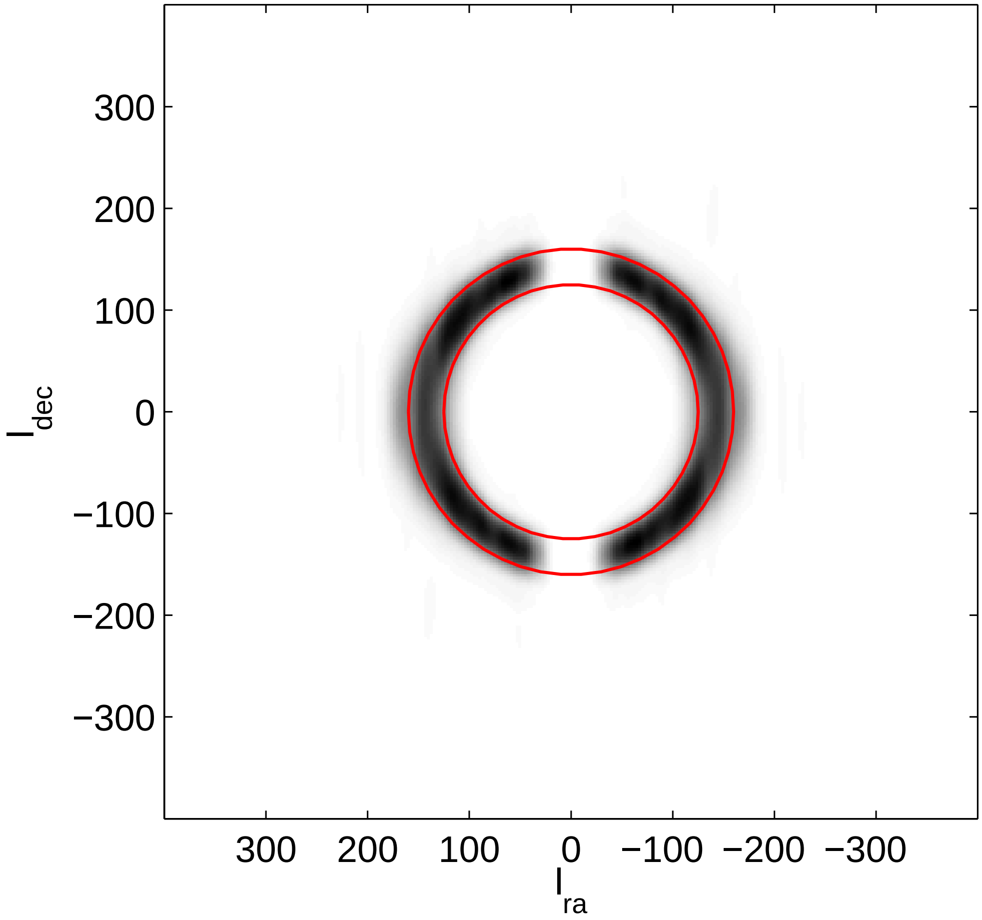

Figure B.4: 2D bandpower window function of the $\ell = 144.3$ bin for $BB$. The red circles are the $\ell$ of 126–160 bin edges. The $BB$ bandpower window function is derived using simulations at a single multipole containing no $E$-mode power and processed through the analysis pipeline, including matrix purification. The suppression of modes along $|\ell_{\rm ra}| \lesssim 40$ is the result of filtering the azimuth scans. The 2D bandpower window functions for $TT$ and $EE$ look qualitatively similar. See Section 4.2 for discussion.

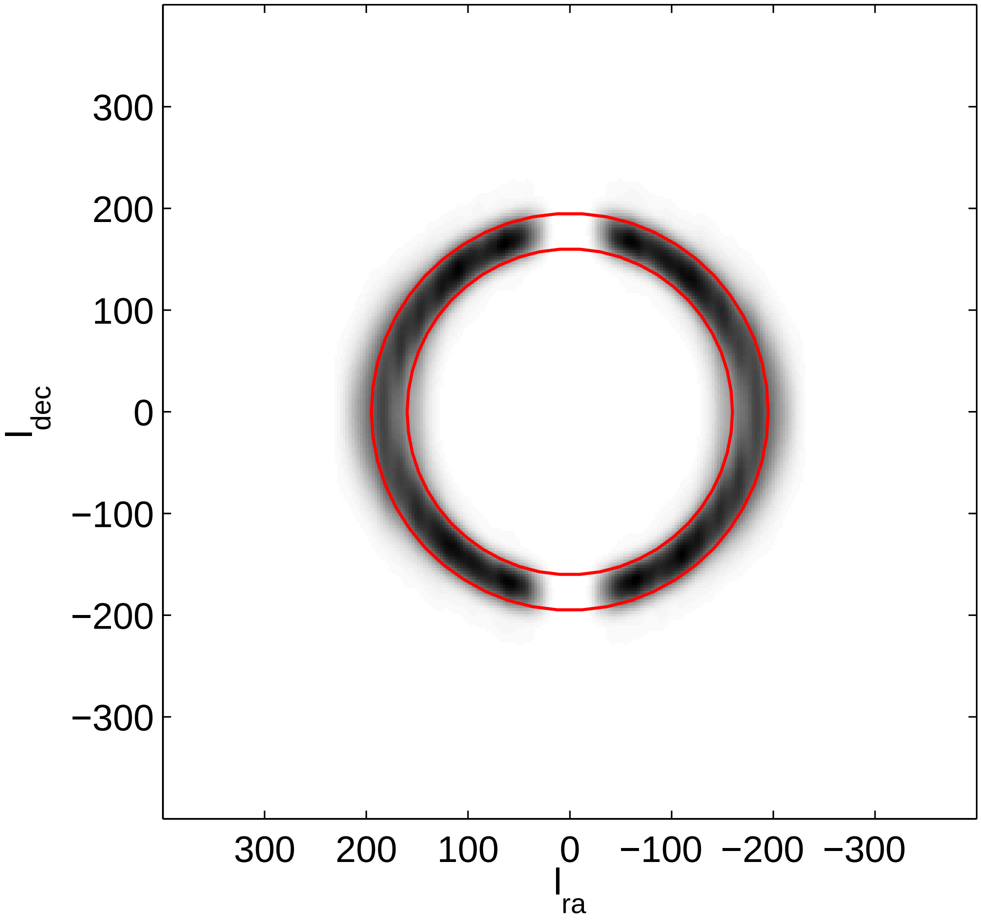

Figure B.5: 2D bandpower window function of the $\ell = 179.1$ bin for $BB$. The red circles are the $\ell$ of 161–195 bin edges. The $BB$ bandpower window function is derived using simulations at a single multipole containing no $E$-mode power and processed through the analysis pipeline, including matrix purification. The suppression of modes along $|\ell_{\rm ra}| \lesssim 40$ is the result of filtering the azimuth scans. The 2D bandpower window functions for $TT$ and $EE$ look qualitatively similar. See Section 4.2 for discussion.

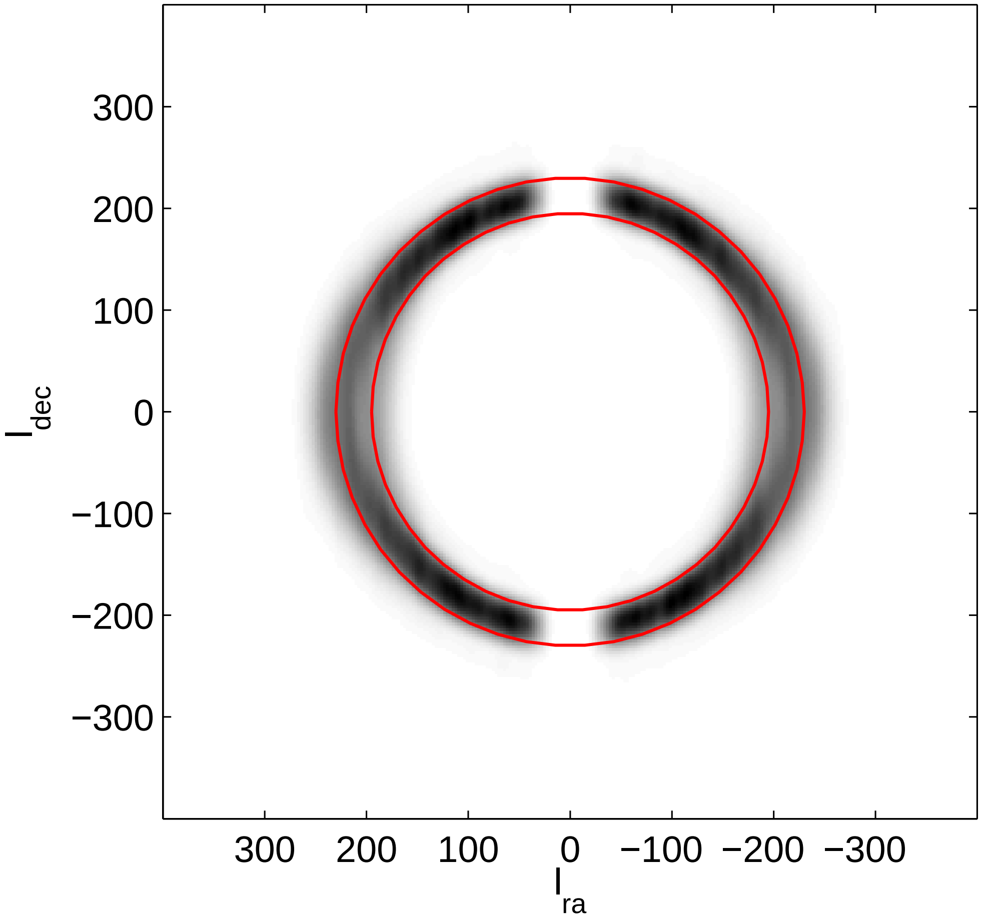

Figure B.6: 2D bandpower window function of the $\ell = 213.7$ bin for $BB$. The red circles are the $\ell$ of 196–230 bin edges. The $BB$ bandpower window function is derived using simulations at a single multipole containing no $E$-mode power and processed through the analysis pipeline, including matrix purification. The suppression of modes along $|\ell_{\rm ra}| \lesssim 40$ is the result of filtering the azimuth scans. The 2D bandpower window functions for $TT$ and $EE$ look qualitatively similar. See Section 4.2 for discussion.

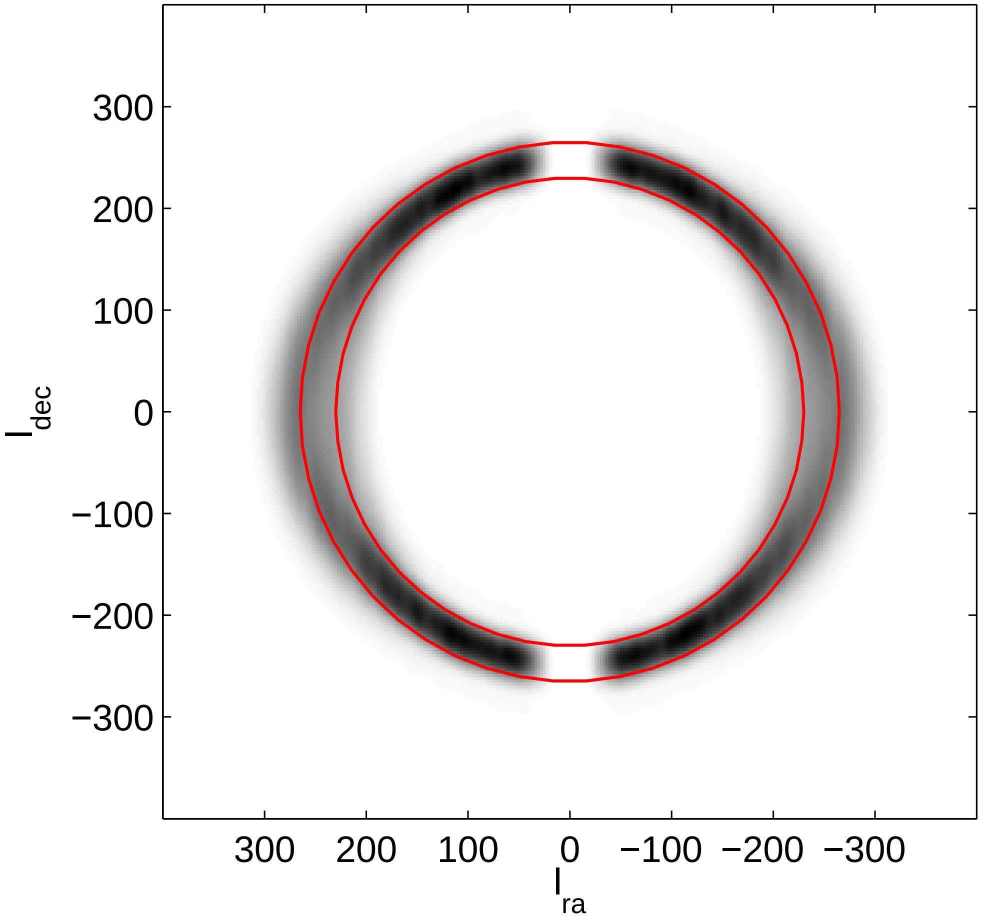

Figure B.7: 2D bandpower window function of the $\ell = 248.4$ bin for $BB$. The red circles are the $\ell$ of 231–265 bin edges. The $BB$ bandpower window function is derived using simulations at a single multipole containing no $E$-mode power and processed through the analysis pipeline, including matrix purification. The suppression of modes along $|\ell_{\rm ra}| \lesssim 40$ is the result of filtering the azimuth scans. The 2D bandpower window functions for $TT$ and $EE$ look qualitatively similar. See Section 4.2 for discussion.

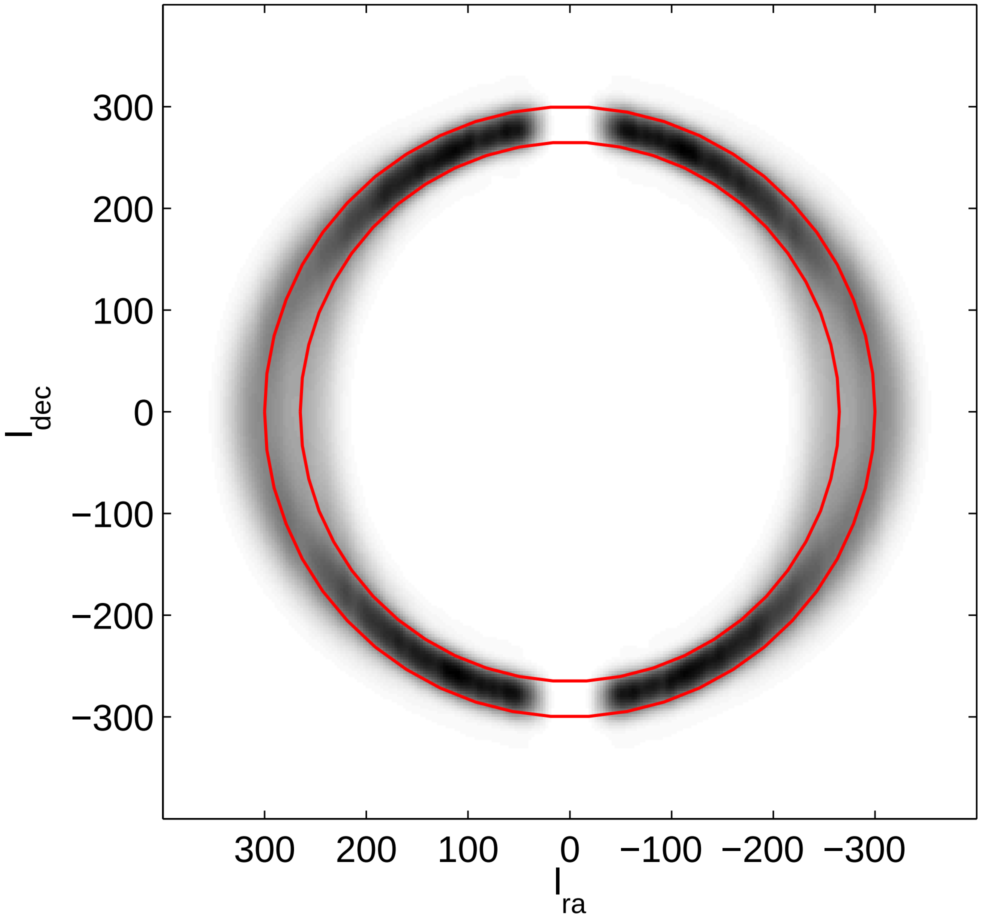

Figure B.8: 2D bandpower window function of the $\ell = 283.0$ bin for $BB$. The red circles are the $\ell$ of 266–300 bin edges. The $BB$ bandpower window function is derived using simulations at a single multipole containing no $E$-mode power and processed through the analysis pipeline, including matrix purification. The suppression of modes along $|\ell_{\rm ra}| \lesssim 40$ is the result of filtering the azimuth scans. The 2D bandpower window functions for $TT$ and $EE$ look qualitatively similar. See Section 4.2 for discussion.

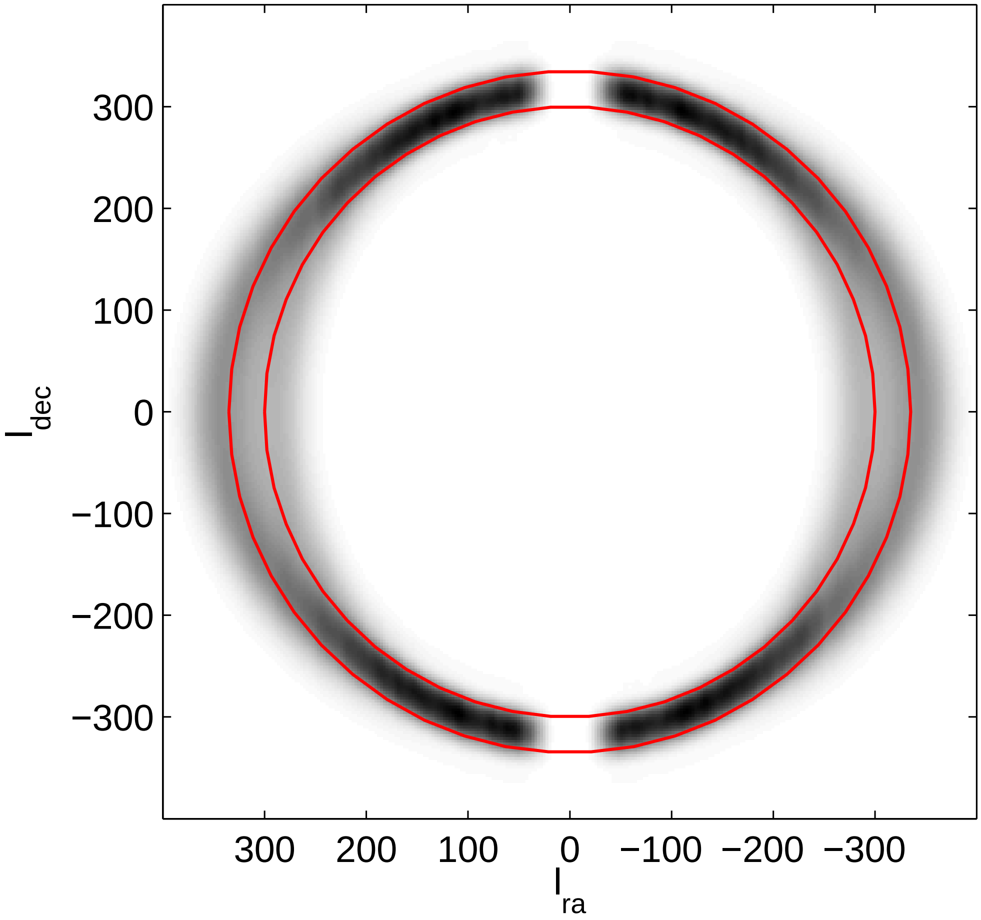

Figure B.9: 2D bandpower window function of the $\ell = 317.2$ bin for $BB$. The red circles are the $\ell$ of 301–335 bin edges. The $BB$ bandpower window function is derived using simulations at a single multipole containing no $E$-mode power and processed through the analysis pipeline, including matrix purification. The suppression of modes along $|\ell_{\rm ra}| \lesssim 40$ is the result of filtering the azimuth scans. The 2D bandpower window functions for $TT$ and $EE$ look qualitatively similar. See Section 4.2 for discussion.

# Appendix C

# BB likelihoods per $\ell$ bin

Table C.1: Marginal likelihood of $\mathcal{D}_\ell^{BB}$ at 150 GHz from the CMB using Bicep2/*Keck Array* and *Planck* 217 and 353 GHz data. The units are in $\mu$K$^2$. The likelihoods are derived in the HL approximation for each $\ell$ bin independently. The data values match Figure 5.13 and Figures C.1–C.9. See Section 5.8 for details of the input model.

| $\ell$ bin center (bin edges) | Maximum likelihood | 68% credible interval | 95% credible interval |
|---|---|---|---|
| 45.3 (21 – 55) | 0.00e+00 | 0.00e+00 – 3.02e-03 | 0.00e+00 – 8.94e-03 |
| 74.2 (56 – 90) | 4.30e-03 | 1.80e-03 – 7.20e-03 | 0.00e+00 – 1.03e-02 |
| 109.2 (91 – 125) | 7.88e-03 | 4.82e-03 – 1.13e-02 | 2.04e-03 – 1.51e-02 |
| 144.3 (126 – 160) | 9.65e-03 | 6.12e-03 – 1.32e-02 | 2.67e-03 – 1.70e-02 |
| 179.1 (161 – 195) | 1.61e-02 | 1.10e-02 – 2.14e-02 | 5.70e-03 – 2.70e-02 |
| 213.7 (196 – 230) | 2.18e-02 | 1.60e-02 – 2.78e-02 | 1.04e-02 – 3.43e-02 |
| 248.4 (231 – 265) | 1.66e-02 | 8.68e-03 – 2.49e-02 | 1.74e-03 – 3.26e-02 |
| 283.0 (266 – 300) | 2.88e-02 | 1.96e-02 – 3.89e-02 | 1.11e-02 – 4.97e-02 |
| 317.2 (301 – 335) | 3.54e-02 | 2.15e-02 – 5.04e-02 | 8.81e-03 – 6.60e-02 |

Table C.2: Marginal likelihood of $\mathcal{D}_\ell^{BB}$ at 150 GHz from Galactic dust using Bicep2/*Keck Array* and *Planck* 217 and 353 GHz data. The units are in $\mu\mathrm{K}^2$. The likelihoods are derived in the HL approximation for each $\ell$ bin independently. The data values match Figure 5.13 and Figures C.1–C.9. See Section 5.8 for details of the input model.

| $\ell$ bin center (bin edges) | Maximum likelihood | 68% credible interval | 95% credible interval |
|---|---|---|---|
| 45.3 (21 – 55) | 6.04e-03 | 2.40e-03 – 1.33e-02 | 3.25e-04 – 2.55e-02 |
| 74.2 (56 – 90) | 7.00e-03 | 4.39e-03 – 1.01e-02 | 2.19e-03 – 1.38e-02 |
| 109.2 (91 – 125) | 7.09e-03 | 4.41e-03 – 1.01e-02 | 2.06e-03 – 1.36e-02 |
| 144.3 (126 – 160) | 3.33e-03 | 7.34e-04 – 6.13e-03 | 0.00e+00 – 9.57e-03 |
| 179.1 (161 – 195) | 2.76e-03 | 0.00e+00 – 6.44e-03 | 0.00e+00 – 1.22e-02 |
| 213.7 (196 – 230) | 1.54e-03 | 0.00e+00 – 5.85e-03 | 0.00e+00 – 1.15e-02 |
| 248.4 (231 – 265) | 1.01e-02 | 4.44e-03 – 1.60e-02 | 0.00e+00 – 2.12e-02 |
| 283.0 (266 – 300) | 0.00e+00 | 0.00e+00 – 4.53e-03 | 0.00e+00 – 1.07e-02 |
| 317.2 (301 – 335) | 0.00e+00 | 0.00e+00 – 7.71e-03 | 0.00e+00 – 1.70e-02 |

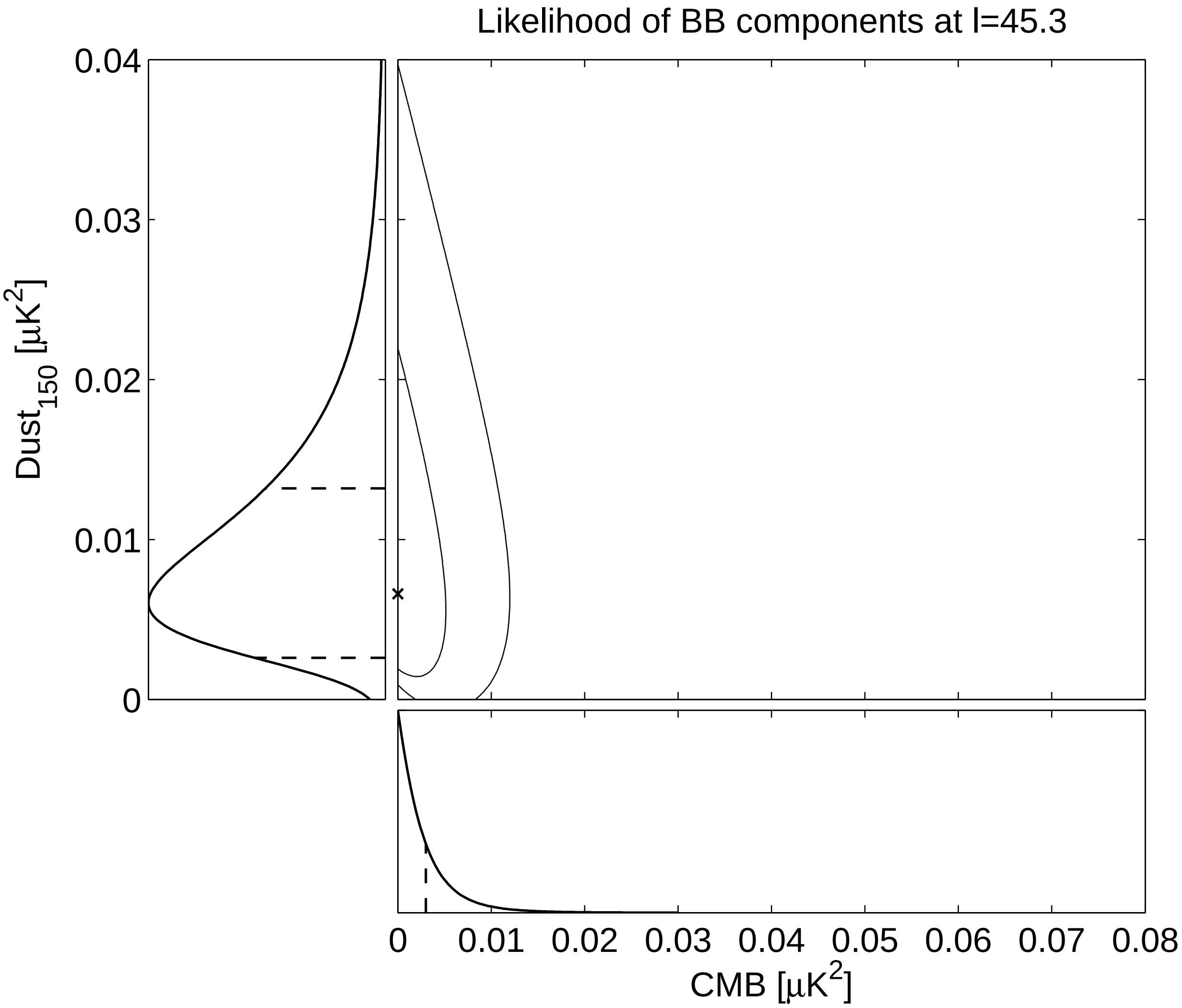

Figure C.1: Likelihood results of BKP for $r$ and dust power at 150 GHz using only the $\ell = 45.3$ bin. The one-dimensional curves are the marginal likelihoods, and the dashed lines are a 68% credible interval. The two-dimensional contours enclose 68% and 95% of the total likelihood. See Section 5.8 for details of the input model.

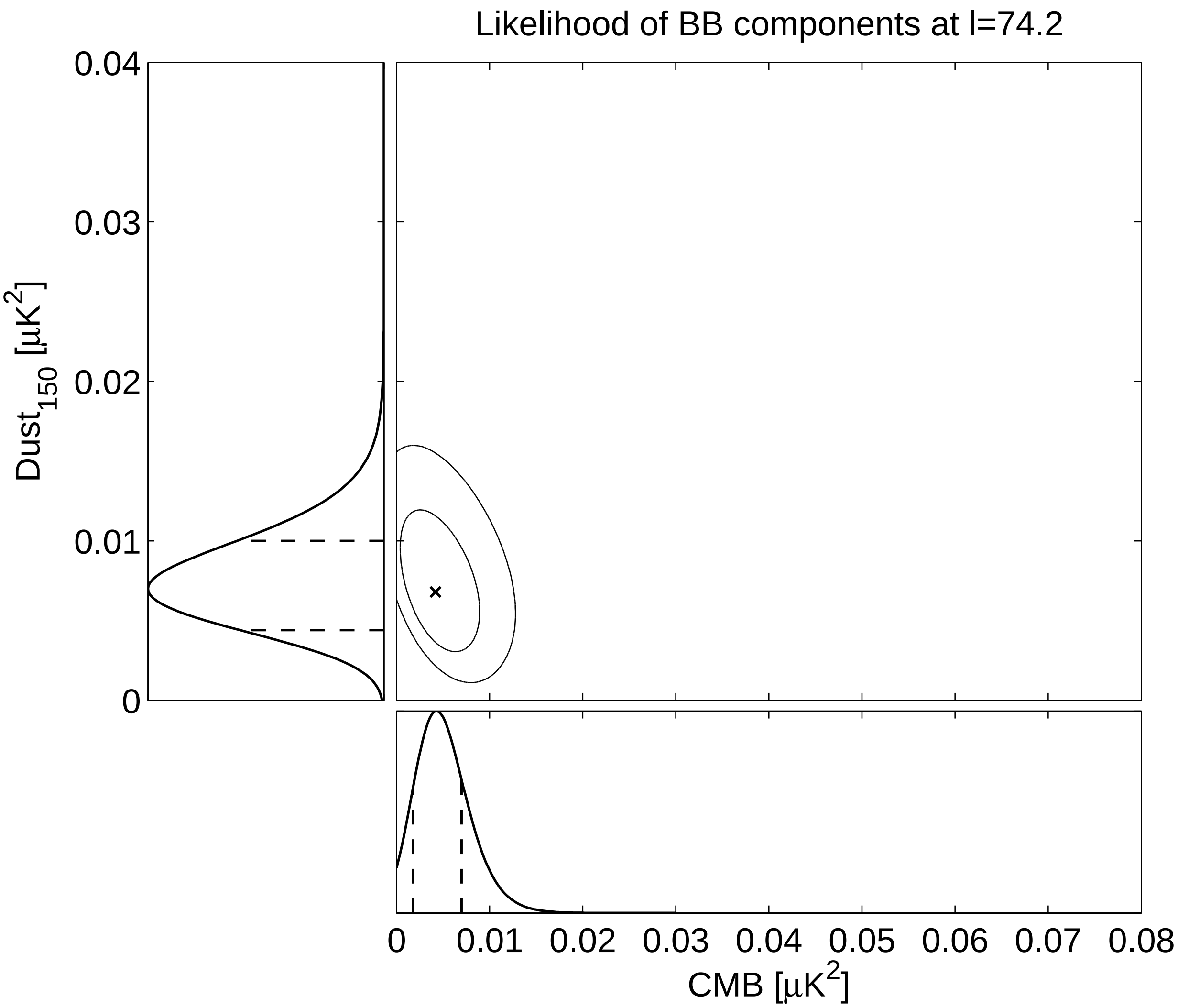

Figure C.2: Likelihood results of BKP for $r$ and dust power at 150 GHz using only the $\ell = 74.2$ bin. The one-dimensional curves are the marginal likelihoods, and the dashed lines are a 68% credible interval. The two-dimensional contours enclose 68% and 95% of the total likelihood. See Section 5.8 for details of the input model.

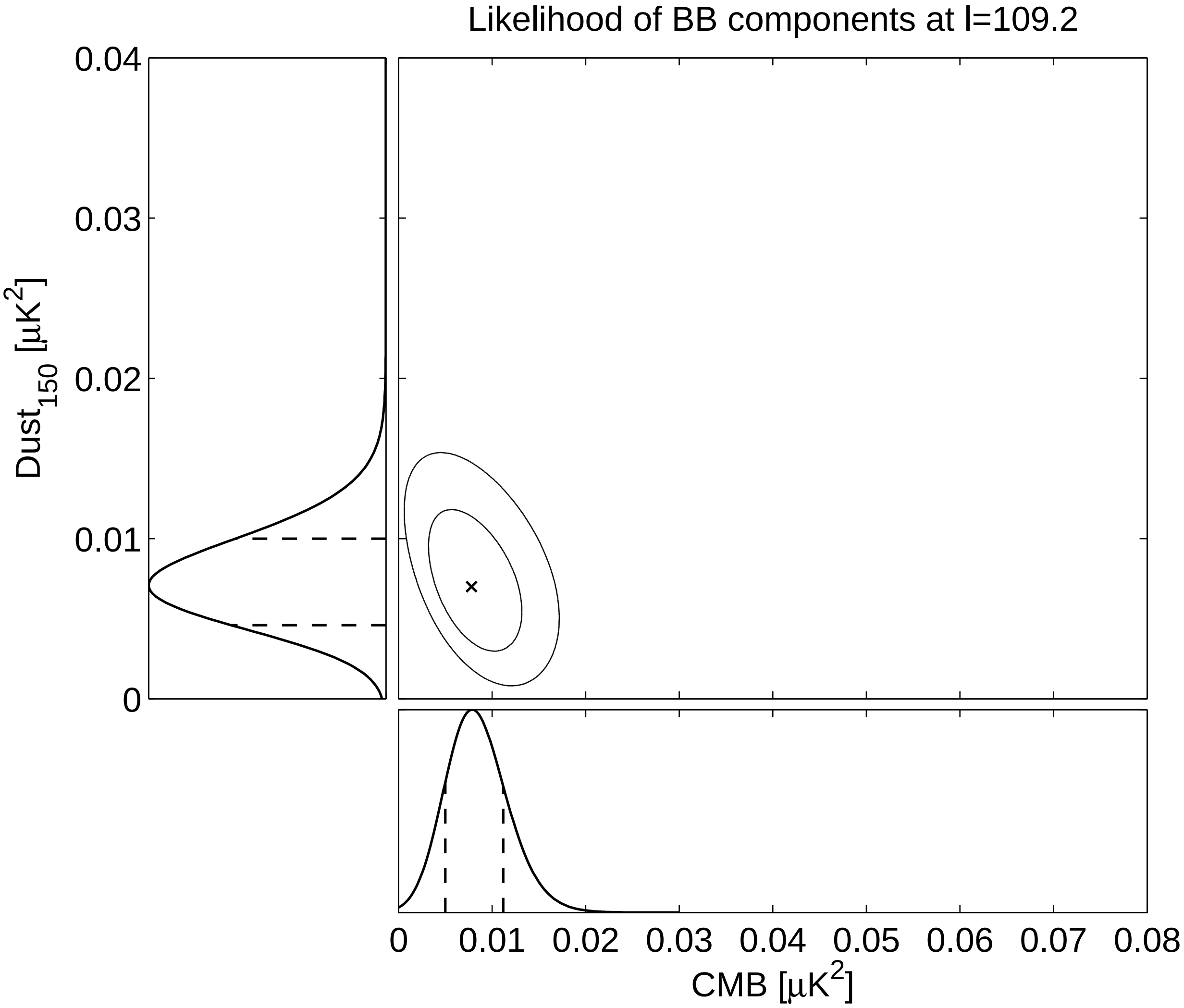

Figure C.3: Likelihood results of BKP for $r$ and dust power at 150 GHz using only the $\ell = 109.2$ bin. The one-dimensional curves are the marginal likelihoods, and the dashed lines are a 68% credible interval. The two-dimensional contours enclose 68% and 95% of the total likelihood. See Section 5.8 for details of the input model.

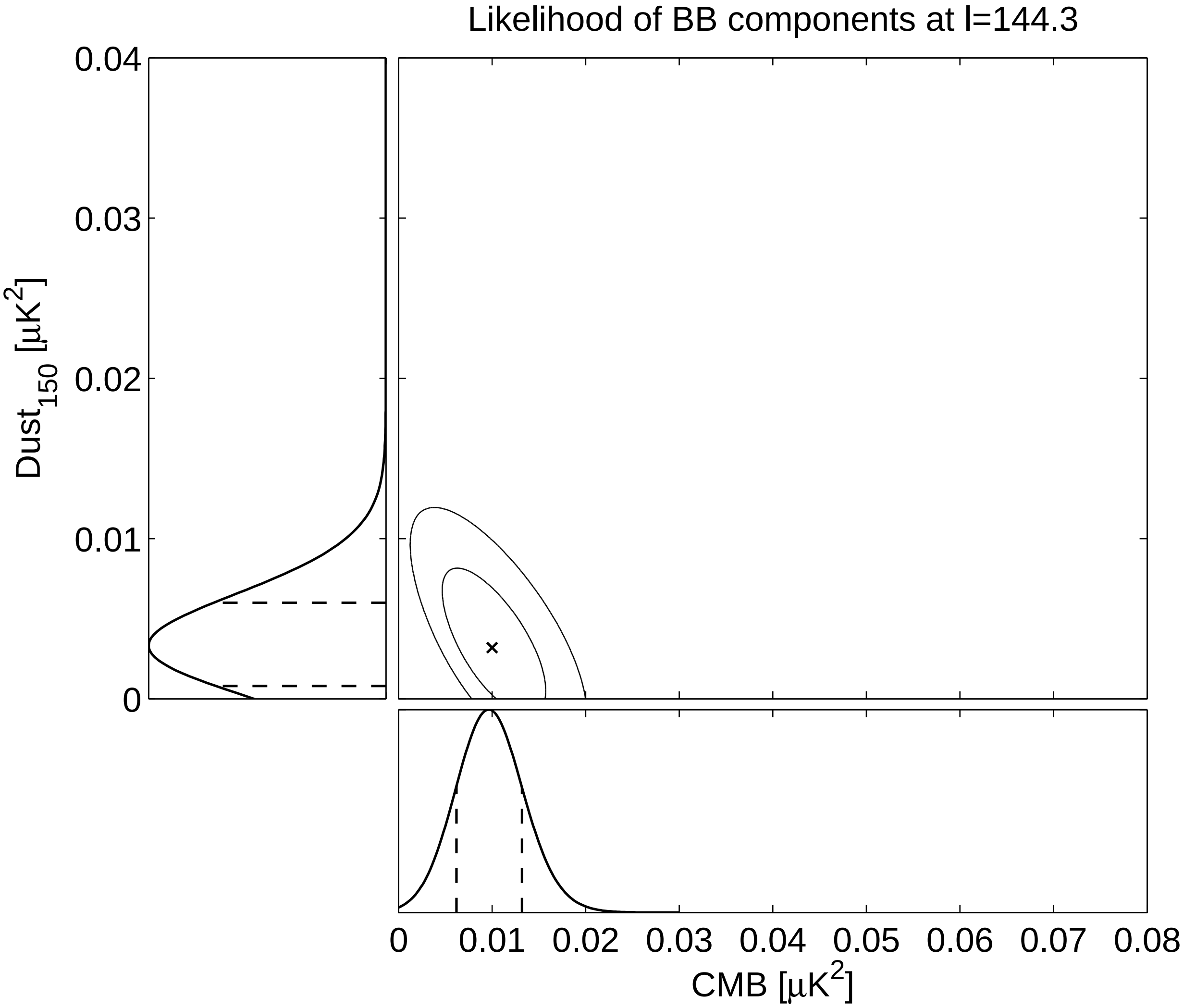

Figure C.4: Likelihood results of BKP for $r$ and dust power at 150 GHz using only the $\ell = 144.3$ bin. The one-dimensional curves are the marginal likelihoods, and the dashed lines are a 68% credible interval. The two-dimensional contours enclose 68% and 95% of the total likelihood. See Section 5.8 for details of the input model.

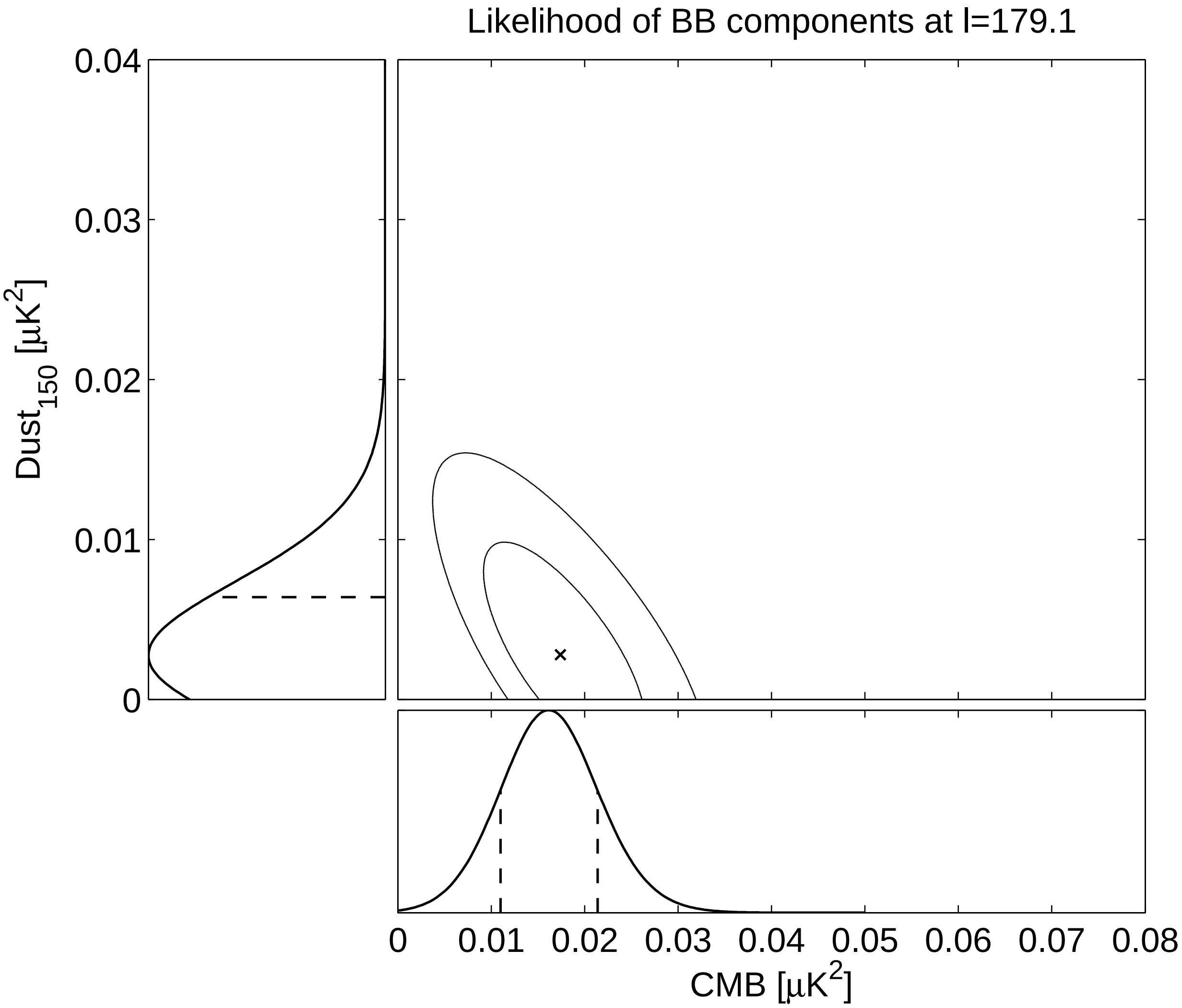

Figure C.5: Likelihood results of BKP for $r$ and dust power at 150 GHz using only the $\ell = 179.1$ bin. The one-dimensional curves are the marginal likelihoods, and the dashed lines are a 68% credible interval. The two-dimensional contours enclose 68% and 95% of the total likelihood. See Section 5.8 for details of the input model.

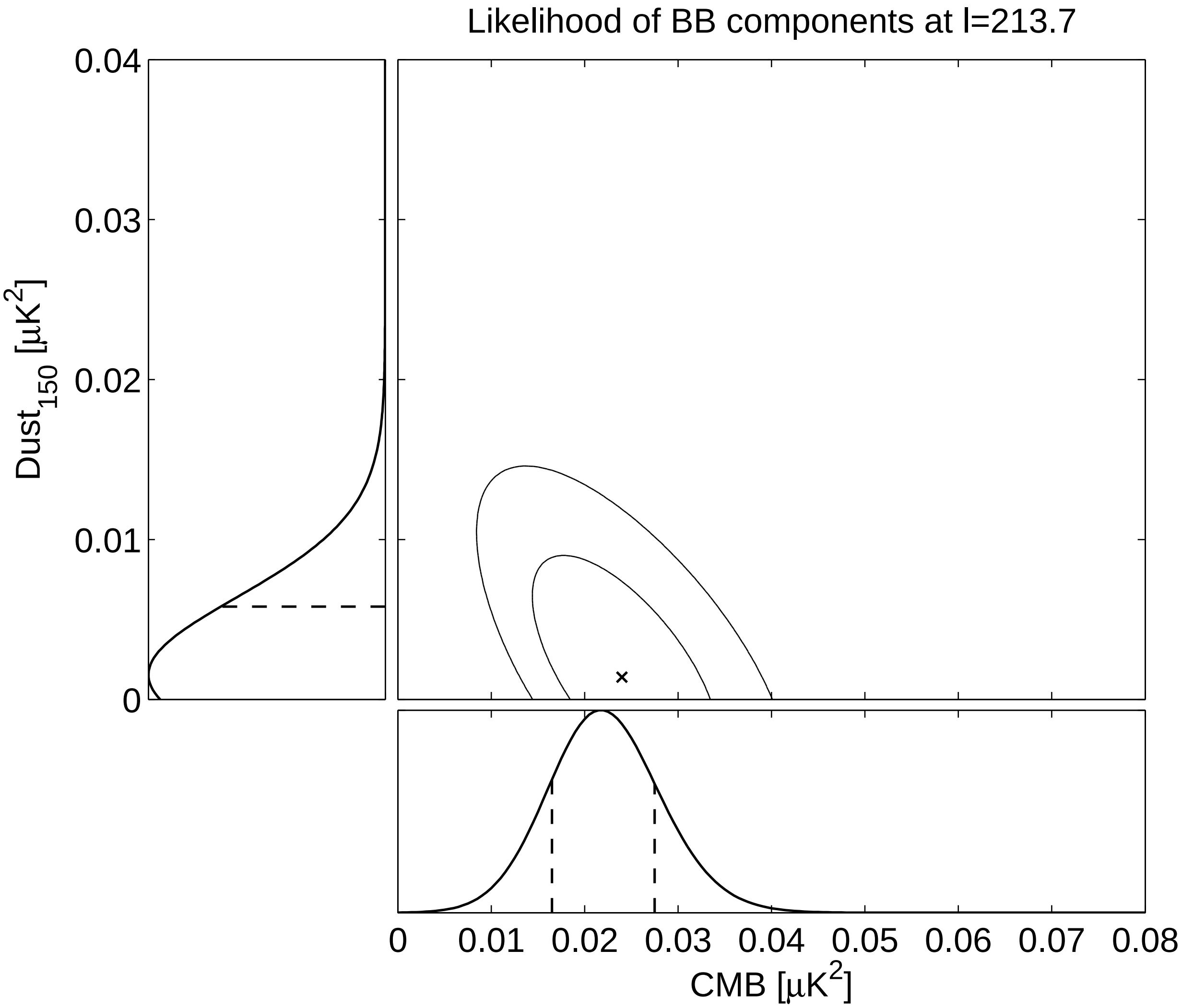

Figure C.6: Likelihood results of BKP for $r$ and dust power at 150 GHz using only the $\ell = 213.7$ bin. The one-dimensional curves are the marginal likelihoods, and the dashed lines are a 68% credible interval. The two-dimensional contours enclose 68% and 95% of the total likelihood. See Section 5.8 for details of the input model.

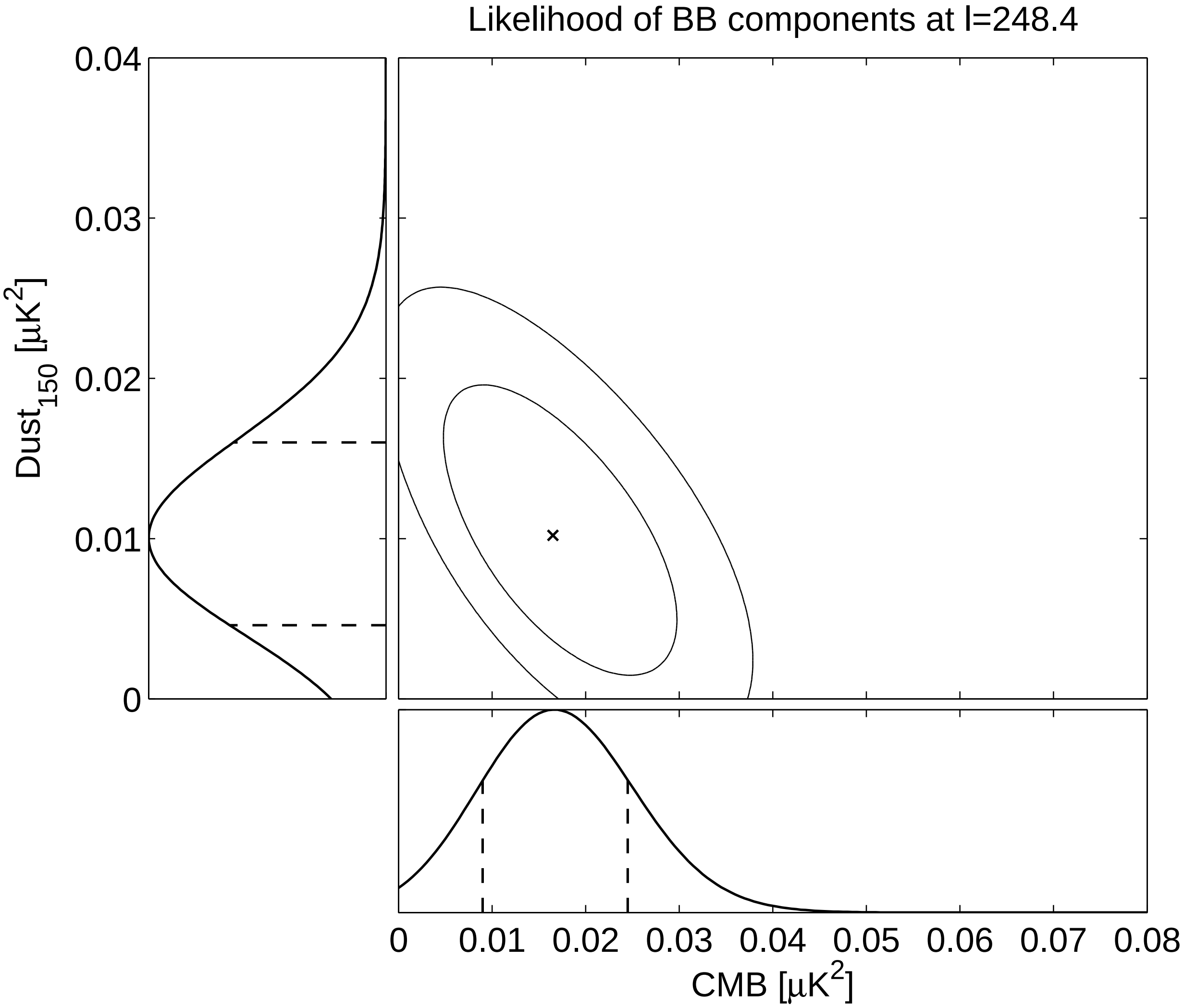

Figure C.7: Likelihood results of BKP for $r$ and dust power at 150 GHz using only the $\ell = 248.4$ bin. The one-dimensional curves are the marginal likelihoods, and the dashed lines are a 68% credible interval. The two-dimensional contours enclose 68% and 95% of the total likelihood. See Section 5.8 for details of the input model.

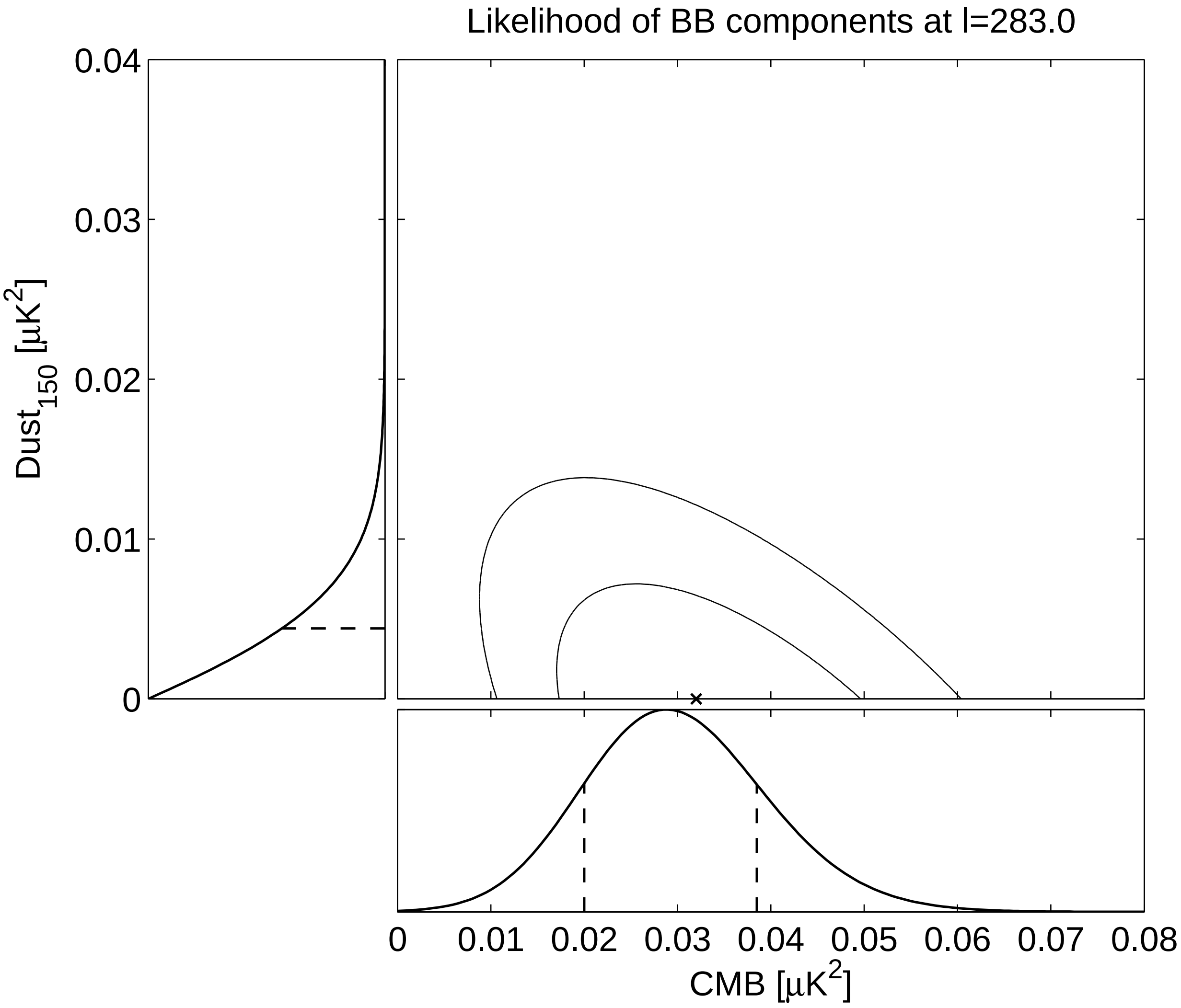

Figure C.8: Likelihood results of BKP for $r$ and dust power at 150 GHz using only the $\ell = 283.0$ bin. The one-dimensional curves are the marginal likelihoods, and the dashed lines are a 68% credible interval. The two-dimensional contours enclose 68% and 95% of the total likelihood. See Section 5.8 for details of the input model.

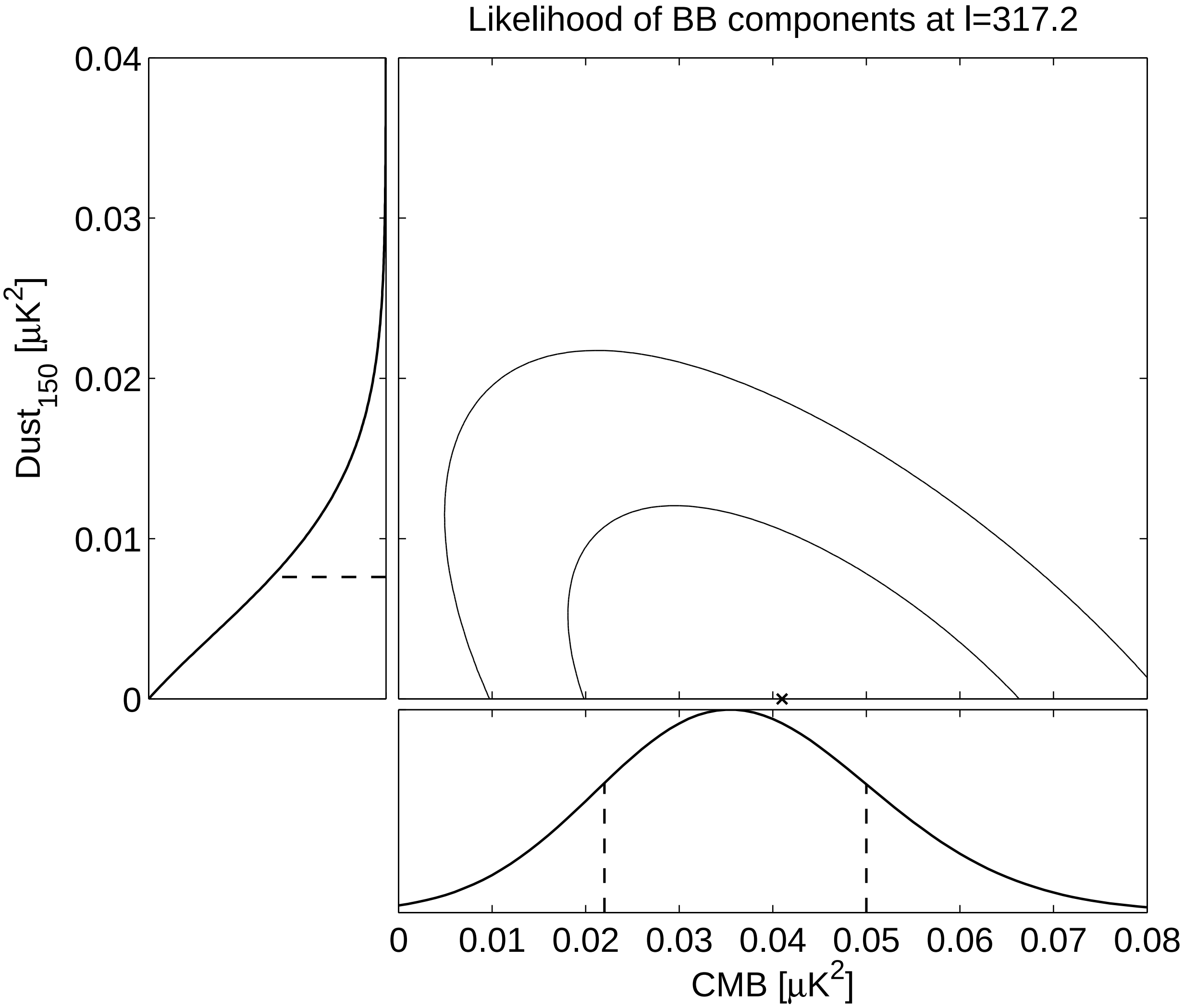

Figure C.9: Likelihood results of BKP for $r$ and dust power at 150 GHz using only the $\ell = 317.2$ bin. The one-dimensional curves are the marginal likelihoods, and the dashed lines are a 68% credible interval. The two-dimensional contours enclose 68% and 95% of the total likelihood. See Section 5.8 for details of the input model.

# Bibliography

[1] Z. Ahmed, M. Amiri, S. J. Benton, J. J. Bock, R. Bowens-Rubin, I. Buder, E. Bullock, J. Connors, J. P. Filippini, J. A. Grayson, M. Halpern, G. C. Hilton, V. V. Hristov, H. Hui, K. D. Irwin, J. Kang, K. S. Karkare, E. Karpel, J. M. Kovac, C. L. Kuo, C. B. Netterfield, H. T. Nguyen, R. O'Brient, R. W. Ogburn, C. Pryke, C. D. Reintsema, S. Richter, K. L. Thompson, A. D. Turner, A. G. Vieregg, W. L. K. Wu, and K. W. Yoon. BICEP3: a 95 GHz refracting telescope for degree-scale CMB polarization. In *Society of Photo-Optical Instrumentation Engineers (SPIE) Conference Series*, volume 9153 of *Society of Photo-Optical Instrumentation Engineers (SPIE) Conference Series*, page 1, August 2014.

[2] R. W. Aikin. *Testing Inflationary Cosmology with the* BICEP1 *and* BICEP2 *Experiments*. Ph.D. thesis, California Institute of Technology, 2013.

[3] D. Barkats, C. Bischoff, P. Farese, L. Fitzpatrick, T. Gaier, J. O. Gundersen, M. M. Hedman, L. Hyatt, J. J. McMahon, D. Samtleben, S. T. Staggs, K. Vanderlinde, and B. Winstein. First Measurements of the Polarization of the Cosmic Microwave Background Radiation at Small Angular Scales from CAPMAP. *Astrophys. J. Lett.*, 619:L127–L130, February 2005.

[4] C. L. Bennett, D. Larson, J. L. Weiland, N. Jarosik, G. Hinshaw, N. Odegard, K. M. Smith, R. S. Hill, B. Gold, M. Halpern, E. Komatsu, M. R. Nolta, L. Page, D. N. Spergel, E. Wollack, J. Dunkley, A. Kogut, M. Limon, S. S. Meyer, G. S. Tucker, and E. L. Wright. Nine-year Wilkinson Microwave Anisotropy Probe (WMAP) Observations: Final Maps and Results. *Astrophys. J. Suppl.*, 208:20, October 2013.

[5] S. J. Benton, P. A. Ade, M. Amiri, F. E. Angilè, J. J. Bock, J. R. Bond, S. A. Bryan, H. C. Chiang, C. R. Contaldi, B. P. Crill, M. J. Devlin, B. Dober, O. P. Doré, M. Farhang, J. P. Filippini, L. M. Fissel, A. A. Fraisse, Y. Fukui, N. Galitzki, A. E. Gambrel, N. N. Gandilo, S. R. Golwala, J. E. Gudmundsson, M. Halpern, M. Hasselfield, G. C. Hilton, W. A. Holmes, V. V. Hristov, K. D. Irwin, W. C. Jones, Z. D. Kermish, J. Klein, A. L. Korotkov, C. L. Kuo, C. J. MacTavish, P. V. Mason, T. G. Matthews, K. G. Megerian, L. Moncelsi, T. A. Morford, T. K. Mroczkowski, J. M. Nagy, C. B. Netterfield, G. Novak, D. Nutter, R. O'Brient, R. W. Ogburn, E. Pascale, F. Poidevin, A. S. Rahlin, C. D. Reintsema, J. E. Ruhl, M. C. Runyan, G. Savini, D. Scott, J. A. Shariff, J. D. Soler, N. E. Thomas, A. Trangsrud, M. D. Truch, C. E. Tucker, G. S. Tucker, R. S. Tucker, A. D. Turner, D. Ward-Thompson, A. C. Weber, D. V. Wiebe, and E. Y. Young. BLASTbus electronics: general-purpose readout and control for balloon-borne experiments. In *Society of Photo-Optical Instrumentation Engineers (SPIE) Conference Series*, volume 9145 of *Society of Photo-Optical Instrumentation Engineers (SPIE) Conference Series*, page 0, July 2014.

[6] BICEP1 Collaboration, D. Barkats, R. Aikin, C. Bischoff, I. Buder, J. P. Kaufman, B. G. Keating, J. M. Kovac, M. Su, P. A. R. Ade, J. O. Battle, E. M. Bierman, J. J. Bock, H. C. Chiang, C. D. Dowell, L. Duband, J. Filippini, E. F. Hivon, W. L. Holzapfel, V. V. Hristov, W. C. Jones, C. L. Kuo, E. M. Leitch, P. V. Mason, T. Matsumura, H. T. Nguyen, N. Ponthieu, C. Pryke, S. Richter, G. Rocha, C. Sheehy, S. S. Kernasovskiy, Y. D. Takahashi, J. E. Tolan, and K. W. Yoon. Degree-scale cosmic microwave background polarization measurements from three years of BICEP1 data. *The Astrophysical Journal*, 783(2):67, 2014.

[7] BICEP2 Collaboration, P. A. R. Ade, R. W. Aikin, M. Amiri, D. Barkats, S. J. Benton, C. A. Bischoff, J. J. Bock, J. A. Brevik, I. Buder, E. Bullock, G. Davis, P. K. Day, C. D. Dowell, L. Duband, J. P. Filippini, S. Fliescher, S. R. Golwala, M. Halpern, M. Hasselfield, S. R. Hildebrandt, G. C. Hilton, K. D. Irwin, K. S. Karkare, J. P. Kaufman, B. G. Keating, S. A. Kernasovskiy, J. M. Kovac, C. L. Kuo, E. M. Leitch, N. Llombart, M. Lueker, C. B. Netterfield, H. T. Nguyen, R. O'Brient, R. W. Ogburn, IV,

A. Orlando, C. Pryke, C. D. Reintsema, S. Richter, R. Schwarz, C. D. Sheehy, Z. K. Staniszewski, K. T. Story, R. V. Sudiwala, G. P. Teply, J. E. Tolan, A. D. Turner, A. G. Vieregg, P. Wilson, C. L. Wong, and K. W. Yoon. BICEP2 II. Experiment and three-year Data Set. *Astrophys. J.*, 792:62, September 2014.

[8] BICEP2 Collaboration, P. A. R. Ade, R. W. Aikin, D. Barkats, S. J. Benton, C. A. Bischoff, J. J. Bock, J. A. Brevik, I. Buder, E. Bullock, C. D. Dowell, L. Duband, J. P. Filippini, S. Fliescher, S. R. Golwala, M. Halpern, M. Hasselfield, S. R. Hildebrandt, G. C. Hilton, K. D. Irwin, K. S. Karkare, J. P. Kaufman, B. G. Keating, S. A. Kernasovskiy, J. M. Kovac, C. L. Kuo, E. M. Leitch, M. Lueker, C. B. Netterfield, H. T. Nguyen, R. O'Brient, R. W. Ogburn, IV, A. Orlando, C. Pryke, S. Richter, R. Schwarz, C. D. Sheehy, Z. K. Staniszewski, R. V. Sudiwala, G. P. Teply, J. E. Tolan, A. D. Turner, A. G. Vieregg, C. L. Wong, and K. W. Yoon. BICEP2 III: Instrumental Systematics. *ArXiv e-prints*, February 2015.

[9] BICEP2 Collaboration, R. W. Ade, P. A. R., D. Barkats, S. J. Benton, C. A. Bischoff, J. J. Bock, J. A. Brevik, I. Buder, E. Bullock, C. D. Dowell, L. Duband, J. P. Filippini, S. Fliescher, S. R. Golwala, M. Halpern, M. Hasselfield, S. R. Hildebrandt, G. C. Hilton, V. V. Hristov, K. D. Irwin, K. S. Karkare, J. P. Kaufman, B. G. Keating, S. A. Kernasovskiy, J. M. Kovac, C. L. Kuo, E. M. Leitch, M. Lueker, P. Mason, C. B. Netterfield, H. T. Nguyen, R. O'Brient, R. W. Ogburn, A. Orlando, C. Pryke, C. D. Reintsema, S. Richter, R. Schwarz, C. D. Sheehy, Z. K. Staniszewski, R. V. Sudiwala, G. P. Teply, J. E. Tolan, A. D. Turner, A. G. Vieregg, C. L. Wong, and K. W. Yoon. Detection of $B$-Mode Polarization at Degree Angular Scales by BICEP2. *Phys. Rev. Lett.*, 112:241101, Jun 2014.

[10] BICEP2, *Keck Array*, and *Planck* Collaborations, P. A. R. Ade, N. Aghanim, Z. Ahmed, R. W. Aikin, K. D. Alexander, M. Arnaud, J. Aumont, C. Baccigalupi, A. J. Banday, D. Barkats, R. B. Barreiro, J. G. Bartlett, N. Bartolo, E. Battaner, K. Benabed, A. Benoît, A. Benoit-Lévy, S. J. Benton, J.-P. Bernard, M. Bersanelli, P. Bielewicz, C. A. Bischoff, J. J. Bock, A. Bonaldi, L. Bonavera, J. R. Bond, J. Borrill, F. R. Bouchet, F. Boulanger, J. A. Brevik, M. Bucher, I. Buder, E. Bullock, C. Burigana, R. C. Butler, V. Buza, E. Calabrese, J.-F. Cardoso, A. Catalano, A. Challinor, R.-R. Chary, H. C. Chi-

ang, P. R. Christensen, L. P. L. Colombo, C. Combet, J. Connors, F. Couchot, A. Coulais, B. P. Crill, A. Curto, F. Cuttaia, L. Danese, R. D. Davies, R. J. Davis, P. de Bernardis, A. de Rosa, G. de Zotti, J. Delabrouille, J.-M. Delouis, F.-X. Désert, C. Dickinson, J. M. Diego, H. Dole, S. Donzelli, O. Doré, M. Douspis, C. D. Dowell, L. Duband, A. Ducout, J. Dunkley, X. Dupac, C. Dvorkin, G. Efstathiou, F. Elsner, T. A. Enßlin, H. K. Eriksen, E. Falgarone, J. P. Filippini, F. Finelli, S. Fliescher, O. Forni, M. Frailis, A. A. Fraisse, E. Franceschi, A. Frejsel, S. Galeotta, S. Galli, K. Ganga, T. Ghosh, M. Giard, E. Gjerløw, S. R. Golwala, J. González-Nuevo, K. M. Górski, S. Gratton, A. Gregorio, A. Gruppuso, J. E. Gudmundsson, M. Halpern, F. K. Hansen, D. Hanson, D. L. Harrison, M. Hasselfield, G. Helou, S. Henrot-Versillé, D. Herranz, S. R. Hildebrandt, G. C. Hilton, E. Hivon, M. Hobson, W. A. Holmes, W. Hovest, V. V. Hristov, K. M. Huffenberger, H. Hui, G. Hurier, K. D. Irwin, A. H. Jaffe, T. R. Jaffe, J. Jewell, W. C. Jones, M. Juvela, A. Karakci, K. S. Karkare, J. P. Kaufman, B. G. Keating, S. Kefeli, E. Keihänen, S. A. Kernasovskiy, R. Keskitalo, T. S. Kisner, R. Kneissl, J. Knoche, L. Knox, J. M. Kovac, N. Krachmalnicoff, M. Kunz, C. L. Kuo, H. Kurki-Suonio, G. Lagache, A. Lähteenmäki, J.-M. Lamarre, A. Lasenby, M. Lattanzi, C. R. Lawrence, E. M. Leitch, R. Leonardi, F. Levrier, A. Lewis, M. Liguori, P. B. Lilje, M. Linden-Vørnle, M. López-Caniego, P. M. Lubin, M. Lueker, J. F. Macías-Pérez, B. Maffei, D. Maino, N. Mandolesi, A. Mangilli, M. Maris, P. G. Martin, E. Martínez-González, S. Masi, P. Mason, S. Matarrese, K. G. Megerian, P. R. Meinhold, A. Melchiorri, L. Mendes, A. Mennella, M. Migliaccio, S. Mitra, M.-A. Miville-Deschênes, A. Moneti, L. Montier, G. Morgante, D. Mortlock, A. Moss, D. Munshi, J. A. Murphy, P. Naselsky, F. Nati, P. Natoli, C. B. Netterfield, H. T. Nguyen, H. U. Nørgaard-Nielsen, F. Noviello, D. Novikov, I. Novikov, R. O'Brient, R. W. Ogburn, A. Orlando, L. Pagano, F. Pajot, R. Paladini, D. Paoletti, B. Partridge, F. Pasian, G. Patanchon, T. J. Pearson, O. Perdereau, L. Perotto, V. Pettorino, F. Piacentini, M. Piat, D. Pietrobon, S. Plaszczynski, E. Pointecouteau, G. Polenta, N. Ponthieu, G. W. Pratt, S. Prunet, C. Pryke, J.-L. Puget, J. P. Rachen, W. T. Reach, R. Rebolo, M. Reinecke, M. Remazeilles, C. Renault, A. Renzi, S. Richter, I. Ristorcelli, G. Rocha, M. Rossetti, G. Roudier, M. Rowan-Robinson, J. A. Rubiño Martín, B. Rusholme, M. Sandri, D. Santos, M. Savelainen, G. Savini, R. Schwarz, D. Scott, M. D. Seiffert, C. D. Sheehy, L. D.

Spencer, Z. K. Staniszewski, V. Stolyarov, R. Sudiwala, R. Sunyaev, D. Sutton, A.-S. Suur-Uski, J.-F. Sygnet, J. A. Tauber, G. P. Teply, L. Terenzi, K. L. Thompson, L. Toffolatti, J. E. Tolan, M. Tomasi, M. Tristram, M. Tucci, A. D. Turner, L. Valenziano, J. Valiviita, B. Van Tent, L. Vibert, P. Vielva, A. G. Vieregg, F. Villa, L. A. Wade, B. D. Wandelt, R. Watson, A. C. Weber, I. K. Wehus, M. White, S. D. M. White, J. Willmert, C. L. Wong, K. W. Yoon, D. Yvon, A. Zacchei, and A. Zonca. Joint Analysis of Bicep2/*Keck Array* and *Planck* Data. *Physical Review Letters*, 114(10):101301, March 2015.

[11] Bicep2, *Keck Array*, and Spider Collaborations, P. A. R. Ade, R. W. Aikin, M. Amiri, D. Barkats, S. J. Benton, C. A. Bischoff, J. J. Bock, J. A. Bonetti, J. A. Brevik, I. Buder, E. Bullock, G. Chattopadhyay, G. Davis, P. K. Day, C. D. Dowell, L. Duband, J. P. Filippini, S. Fliescher, S. R. Golwala, M. Halpern, M. Hasselfield, S. R. Hildebrandt, G. C. Hilton, V. Hristov, H. Hui, K. D. Irwin, W. C. Jones, K. S. Karkare, J. P. Kaufman, B. G. Keating, S. Kefeli, S. A. Kernasovskiy, J. M. Kovac, C. L. Kuo, H. G. Leduc, E. M. Leitch, N. Llombart, M. Lueker, P. Mason, K. Megerian, L. Moncelsi, C. B. Netterfield, H. T. Nguyen, R. O'Brient, R. W. Ogburn, Iv, A. Orlando, C. Pryke, A. S. Rahlin, C. D. Reintsema, S. Richter, M. C. Runyan, R. Schwarz, C. D. Sheehy, Z. K. Staniszewski, R. V. Sudiwala, G. P. Teply, J. E. Tolan, A. Trangsrud, R. S. Tucker, A. D. Turner, A. G. Vieregg, A. Weber, D. V. Wiebe, P. Wilson, C. L. Wong, K. W. Yoon, and J. Zmuidzinas. Antenna-coupled TES bolometers used in Bicep2, *Keck Array*, and Spider. *ArXiv e-prints*, February 2015.

[12] Bicep2/*Keck Array* Collaborations, P. A. R. Ade, Z. Ahmed, R. W. Aikin, K. D. Alexander, D. Barkats, S. J. Benton, C. A. Bischoff, J. J. Bock, J. A. Brevik, I. Buder, E. Bullock, V. Buza, J. Connors, B. P. Crill, C. D. Dowell, C. Dvorkin, L. Duband, J. P. Filippini, S. Fliescher, S. R. Golwala, M. Halpern, M. Hasselfield, S. R. Hildebrandt, G. C. Hilton, V. V. Hristov, H. Hui, K. D. Irwin, K. S. Karkare, J. P. Kaufman, B. G. Keating, S. Kefeli, S. A. Kernasovskiy, J. M. Kovac, C. L. Kuo, E. M. Leitch, M. Lueker, P. Mason, K. G. Megerian, C. B. Netterfield, H. T. Nguyen, R. O'Brient, R. W. Ogburn, IV, A. Orlando, C. Pryke, C. D. Reintsema, S. Richter, R. Schwarz, C. D. Sheehy, Z. K. Staniszewski, R. V. Sudiwala,

G. P. Teply, K. L. Thompson, J. E. Tolan, A. D. Turner, A. G. Vieregg, A. C. Weber, J. Willmert, C. L. Wong, and K. W. Yoon. BICEP2/*Keck Array* V: Measurements of B-mode Polarization at Degree Angular Scales and 150 GHz by the Keck Array. *ArXiv e-prints*, February 2015.

[13] BICEP2/*Keck Array* Collaborations, P. A. R. Ade, R. W. Aikin, D. Barkats, S. J. Benton, C. A. Bischoff, J. J. Bock, K. J. Bradford, J. A. Brevik, I. Buder, E. Bullock, C. D. Dowell, L. Duband, J. P. Filippini, S. Fliescher, S. R. Golwala, M. Halpern, M. Hasselfield, S. R. Hildebrandt, G. C. Hilton, H. Hui, K. D. Irwin, J. H. Kang, K. S. Karkare, J. P. Kaufman, B. G. Keating, S. Kefeli, S. A. Kernasovskiy, J. M. Kovac, C. L. Kuo, E. M. Leitch, M. Lueker, K. G. Megerian, C. B. Netterfield, H. T. Nguyen, R. O'Brient, R. W. Ogburn, IV, A. Orlando, C. Pryke, S. Richter, R. Schwarz, C. D. Sheehy, Z. K. Staniszewski, R. V. Sudiwala, G. P. Teply, K. Thompson, J. E. Tolan, A. D. Turner, A. G. Vieregg, A. C. Weber, C. L. Wong, and K. W. Yoon. BICEP2/*Keck Array* IV: Optical Characterization and Performance of the BICEP2 and *Keck Array* Experiments. *ArXiv e-prints*, February 2015.

[14] J. J. Bock, J. Glenn, S. M. Grannan, K. D. Irwin, A. E. Lange, H. G. Leduc, and A. D. Turner. Silicon nitride micromesh bolometer arrays for SPIRE. In T. G. Phillips, editor, *Advanced Technology MMW, Radio, and Terahertz Telescopes*, volume 3357 of *Society of Photo-Optical Instrumentation Engineers (SPIE) Conference Series*, pages 297–304, July 1998.

[15] J. A. Brevik. *Searching for Primordial Gravitational Waves at Degree Scales from the South Pole*. Ph.D. thesis, California Institute of Technology, 2012.

[16] M. Bucher. Physics of the cosmic microwave background anisotropy. *International Journal of Modern Physics D*, 24:30004, January 2015.

[17] E. F. Bunn, M. Zaldarriaga, M. Tegmark, and A. de Oliveira-Costa. ¡i¿e/b¡/i¿ decomposition of finite pixelized cmb maps. *Phys. Rev. D*, 67:023501, Jan 2003.

[18] J. Caligiuri and A. Kosowsky. Inflationary Tensor Perturbations after BICEP2. *Physical Review Letters*, 112(19):191302, May 2014.

[19] CAPMAP Collaboration, C. Bischoff, L. Hyatt, J. J. McMahon, G. W. Nixon, D. Samtleben, K. M. Smith, K. Vanderlinde, D. Barkats, P. Farese, T. Gaier, J. O. Gundersen, M. M. Hedman, S. T. Staggs, and B. Winstein. New Measurements of Fine-Scale CMB Polarization Power Spectra from CAPMAP at Both 40 and 90 GHz. *Astrophys. J.*, 684:771–789, September 2008.

[20] R. A. Chamberlin, A. P. Lane, and A. A. Stark. The 492 GHz atmospheric opacity at the geographic South Pole. *The Astrophysical Journal*, 476(1):428, 1997.

[21] H. C. Chiang, P. A. R. Ade, D. Barkats, J. O. Battle, E. M. Bierman, J. J. Bock, C. D. Dowell, L. Duband, E. F. Hivon, W. L. Holzapfel, V. V. Hristov, W. C. Jones, B. G. Keating, J. M. Kovac, C. L. Kuo, A. E. Lange, E. M. Leitch, P. V. Mason, T. Matsumura, H. T. Nguyen, N. Ponthieu, C. Pryke, S. Richter, G. Rocha, C. Sheehy, Y. D. Takahashi, J. E. Tolan, and K. W. Yoon. Measurement of Cosmic Microwave Background Polarization Power Spectra from Two Years of Bicep Data. *Astrophys. J.*, 711:1123–1140, March 2010.

[22] C. C. Craig. On the frequency function of *xy*. *Ann. Math. Statist.*, 7(1):1–15, 03 1936.

[23] A. T. Crites, J. W. Henning, P. A. R. Ade, K. A. Aird, J. E. Austermann, J. A. Beall, A. N. Bender, B. A. Benson, L. E. Bleem, J. E. Carstrom, C. L. Chang, H. C. Chiang, H. Cho, R. Citron, T. M. Crawford, T. De Haan, M. A. Dobbs, W. Everett, J Gallicchio, J. Gao, E. M. George, A. Gilbert, N. W. Halverson, D. Hanson, N. Harrington, G. C. Hilton, G. P. Holder, W. L. Holzapfel, S. Hoover, Z. Hou, J. D. Hrubes, N. Huang, J. Hubmayr, K. D. Irwin, R. Keisler, L. Knox, A. T. Lee, E. M. Leitch, D. Li, C. Liang, D. Luong-Van, J. J. McMahon, J. Mehl, S. S. Meyer, L. Mocanu, T. E. Montroy, T. Natoli, J. P. Nibarger, V. Novosad, S. Padin, C. Pryke, C. L. Reichardt, J. E. Ruhl, B. R. Saliwanchik, J. T. Sayre, K. K. Schaffer, G. Smecher, A. A. Stark, K. T. Story, C. Tucker, K. Vanderlinde, J. D. Vieira, G. Wang, N. Whitehorn, V. Yefremenko, and O. Zahn. Measurements of E-Mode Polarization and Temperature-E-Mode Correlation in the Cosmic Microwave Background from 100 Square Degrees of SPTpol Data. *ArXiv e-prints*, November 2014.

[24] S. Dodelson. Coherent Phase Argument for Inflation. In J. F. Nieves and R. R. Volkas, editors, *Neutrinos, Flavor Physics, and Precision Cosmology*, volume 689 of *American Institute of Physics Conference Series*, pages 184–196, October 2003.

[25] S. Dodelson. How Much Can We Learn about the Physics of Inflation? *Physical Review Letters*, 112(19):191301, May 2014.

[26] L. Duband and B. Collaudin. Sorption coolers development at CEA-SBT. *Cryogenics*, 39(8):659–663, 1999.

[27] D. J. Fixsen. The Temperature of the Cosmic Microwave Background. *Astrophys. J.*, 707:916–920, December 2009.

[28] S. Galli, K. Benabed, F. Bouchet, J.-F. Cardoso, F. Elsner, E. Hivon, A. Mangilli, S. Prunet, and B. Wandelt. Cmb polarization can constrain cosmology better than cmb temperature. *Phys. Rev. D*, 90:063504, Sep 2014.

[29] J. M. Gildemeister, A. T. Lee, and P. L. Richards. Model for excess noise in voltage-biased superconducting bolometers. *Appl. Opt.*, 40:6229–6235, December 2001.

[30] K. M. Górski, E. Hivon, A. J. Banday, B. D. Wandelt, F. K. Hansen, M. Reinecke, and M. Bartelmann. HEALPix: A Framework for High-Resolution Discretization and Fast Analysis of Data Distributed on the Sphere. *Astrophys. J.*, 622:759–771, April 2005.

[31] S. Hamimeche and A. Lewis. Likelihood analysis of CMB temperature and polarization power spectra. *Phys. Rev. D*, 77(10):103013, May 2008.

[32] D. Hanson, S. Hoover, A. Crites, P. A. R. Ade, K. A. Aird, J. E. Austermann, J. A. Beall, A. N. Bender, B. A. Benson, L. E. Bleem, J. J. Bock, J. E. Carlstrom, C. L. Chang, H. C. Chiang, H.-M. Cho, A. Conley, T. M. Crawford, T. de Haan, M. A. Dobbs, W. Everett, J. Gallicchio, J. Gao, E. M. George, N. W. Halverson, N. Harrington, J. W. Henning, G. C. Hilton, G. P. Holder, W. L. Holzapfel, J. D. Hrubes, N. Huang, J. Hubmayr, K. D. Irwin, R. Keisler, L. Knox, A. T. Lee, E. Leitch, D. Li, C. Liang,

D. Luong-Van, G. Marsden, J. J. McMahon, J. Mehl, S. S. Meyer, L. Mocanu, T. E. Montroy, T. Natoli, J. P. Nibarger, V. Novosad, S. Padin, C. Pryke, C. L. Reichardt, J. E. Ruhl, B. R. Saliwanchik, J. T. Sayre, K. K. Schaffer, B. Schulz, G. Smecher, A. A. Stark, K. T. Story, C. Tucker, K. Vanderlinde, J. D. Vieira, M. P. Viero, G. Wang, V. Yefremenko, O. Zahn, and M. Zemcov. Detection of B-Mode Polarization in the Cosmic Microwave Background with Data from the South Pole Telescope. *Physical Review Letters*, 111(14):141301, October 2013.

[33] M. Hasselfield. *Galaxy cluster cosmology with the Atacama Cosmology Telescope*. Ph.D. thesis, University of British Columbia, 2013.

[34] J. R. Hinderks, P. Ade, J. Bock, M. Bowden, M. L. Brown, G. Cahill, J. E. Carlstrom, P. G. Castro, S. Church, T. Culverhouse, R. Friedman, K. Ganga, W. K. Gear, S. Gupta, J. Harris, V. Haynes, B. G. Keating, J. Kovac, E. Kirby, A. E. Lange, E. Leitch, O. E. Mallie, S. Melhuish, Y. Memari, A. Murphy, A. Orlando, R. Schwarz, C. O. Sullivan, L. Piccirillo, C. Pryke, N. Rajguru, B. Rusholme, A. N. Taylor, K. L. Thompson, C. Tucker, A. H. Turner, E. Y. S. Wu, and M. Zemcov. QUaD: A High-Resolution Cosmic Microwave Background Polarimeter. *Astrophys. J.*, 692:1221–1246, February 2009.

[35] E. Hivon, K. M. Górski, C. B. Netterfield, B. P. Crill, S. Prunet, and F. Hansen. MASTER of the Cosmic Microwave Background Anisotropy Power Spectrum: A Fast Method for Statistical Analysis of Large and Complex Cosmic Microwave Background Data Sets. *Astrophys. J.*, 567:2–17, March 2002.

[36] K.D. Irwin and G.C. Hilton. Transition-edge sensors. In Christian Enss, editor, *Cryogenic Particle Detection*, volume 99 of *Topics in Applied Physics*, pages 63–150. Springer Berlin Heidelberg, 2005.

[37] M. Kamionkowski, A. Kosowsky, and A. Stebbins. A Probe of Primordial Gravity Waves and Vorticity. *Physical Review Letters*, 78:2058–2061, March 1997.

[38] M. Kamionkowski, A. Kosowsky, and A. Stebbins. Statistics of cosmic microwave background polarization. *Phys. Rev. D*, 55:7368–7388, June 1997.

[39] K. S. Karkare, P. A. R. Ade, Z. Ahmed, R. W. Aikin, K. D. Alexander, M. Amiri, D. Barkats, S. J. Benton, C. A. Bischoff, J. J. Bock, J. A. Bonetti, J. A. Brevik, I. Buder, E. W. Bullock, B. Burger, J. Connors, B. P. Crill, G. Davis, C. D. Dowell, L. Duband, J. P. Filippini, S. T. Fliescher, S. R. Golwala, M. S. Gordon, J. A. Grayson, M. Halpern, M. Hasselfield, S. R. Hildebrandt, G. C. Hilton, V. V. Hristov, H. Hui, K. D. Irwin, J. H. Kang, E. Karpel, S. Kefeli, S. A. Kernasovskiy, J. M. Kovac, C. L. Kuo, E. M. Leitch, M. Lueker, P. Mason, K. G. Megerian, C. B. Netterfield, H. T. Nguyen, R. O'Brient, R. W. Ogburn, C. L. Pryke, C. D. Reintsema, S. Richter, R. Schwarz, C. D. Sheehy, Z. K. Staniszewski, R. V. Sudiwala, G. P. Teply, K. L. Thompson, J. E. Tolan, A. D. Turner, A. Vieregg, A. Weber, C. L. Wong, W. L. K. Wu, and K. W. Yoon. *Keck Array* and BICEP3: spectral characterization of 5000+ detectors. In *Society of Photo-Optical Instrumentation Engineers (SPIE) Conference Series*, volume 9153 of *Society of Photo-Optical Instrumentation Engineers (SPIE) Conference Series*, page 3, August 2014.

[40] J. P. Kaufman. *Detection of degree-scale B-mode polarization and studying cosmic polarization rotation with the* BICEP1 *and* BICEP2 *telescopes*. Ph.D. thesis, University of California, San Diego, 2014.

[41] B. G. Keating, C. W. O'Dell, J. O. Gundersen, L. Piccirillo, N. C. Stebor, and P. T. Timbie. An Instrument for Investigating the Large Angular Scale Polarization of the Cosmic Microwave Background. *Astrophys. J. Suppl.*, 144:1–20, January 2003.

[42] R. Keisler, S. Hoover, N. Harrington, J. W. Henning, P. A. R. Ade, K. A. Aird, J. E. Austermann, J. A. Beall, A. N. Bender, B. A. Benson, L. E. Bleem, J. E. Carlstrom, C. L. Chang, H. C. Chiang, H. Cho, R. Citron, T. M. Crawford, A. T. Crites, T. de Haan, M. A. Dobbs, W. Everett, J. Gallicchio, J. Gao, E. M. George, A. Gilbert, N. W. Halverson, D. Hanson, G. C. Hilton, G. P. Holder, W. L. Holzapfel, Z. Hou, J. D. Hrubes, N. Huang, J. Hubmayr, K. D. Irwin, L. Knox, A. T. Lee, E. M. Leitch, D. Li, D. Luong-Van, D. P. Marrone, J. J. McMahon, J. Mehl, S. S. Meyer, L. Mocanu, T. Natoli, J. P. Nibarger, V. Novosad, S. Padin, C. Pryke, C. L. Reichardt, J. E. Ruhl, B. R. Saliwanchik, J. T. Sayre, K. K. Schaffer, E. Shirokoff, G. Smecher, A. A. Stark, K. T. Story, C. Tucker, K. Vanderlinde, J. D.

Vieira, G. Wang, N. Whitehorn, V. Yefremenko, and O. Zahn. Measurements of Sub-degree B-mode Polarization in the Cosmic Microwave Background from 100 Square Degrees of SPTpol Data. *ArXiv e-prints*, March 2015.

[43] S. A. Kernasovskiy. *Measuring the polarization of the cosmic microwave background with the Keck Array and* BICEP2. Ph.D. thesis, Stanford University, 2014.

[44] J. M. Kovac, E. M. Leitch, C. Pryke, J. E. Carlstrom, N. W. Halverson, and W. L. Holzapfel. Detection of polarization in the cosmic microwave background using DASI. *Nature*, 420:772, December 2002.

[45] E. M. Leitch, J. M. Kovac, C. Pryke, J. E. Carlstrom, N. W. Halverson, W. L. Holzapfel, M. Dragovan, B. Reddall, and E. S. Sandberg. Measurement of polarization with the Degree Angular Scale Interferometer. *Nature*, 420:763–771, December 2002.

[46] A. Lewis. LensPix: Fast MPI full sky transforms for HEALPix, February 2011. Astrophysics Source Code Library.

[47] A. Lewis and S. Bridle. Cosmological parameters from CMB and other data: A Monte Carlo approach. *Phys. Rev. D*, 66(10):103511, November 2002.

[48] D. H. Martin and E. Puplett. Polarised interferometric spectrometry for the millimeter and submillimeter spectrum. *Infrared Physics*, 10:105–109, 1970.

[49] J. Martin, C. Ringeval, and V. Vennin. Encyclopædia Inflationaris. *Physics of the Dark Universe*, 5:75–235, December 2014.

[50] P. G. Martin. On Predicting the Polarization of Low Frequency Emission by Diffuse Interstellar Dust. In M.-A. Miville-Deschênes and F. Boulanger, editors, *EAS Publications Series*, volume 23 of *EAS Publications Series*, pages 165–188, 2007.

[51] J. C. Mather. Bolometer noise: nonequilibrium theory. *Appl. Opt.*, 21:1125–1129, March 1982.

[52] T. E. Montroy, P. A. R. Ade, J. J. Bock, J. R. Bond, J. Borrill, A. Boscaleri, P. Cabella, C. R. Contaldi, B. P. Crill, P. de Bernardis, G. De Gasperis, A. de Oliveira-Costa, G. De Troia, G. di Stefano, E. Hivon, A. H. Jaffe, T. S. Kisner, W. C. Jones, A. E. Lange, S. Masi, P. D. Mauskopf, C. J. MacTavish, A. Melchiorri, P. Natoli, C. B. Netterfield, E. Pascale, F. Piacentini, D. Pogosyan, G. Polenta, S. Prunet, S. Ricciardi, G. Romeo, J. E. Ruhl, P. Santini, M. Tegmark, M. Veneziani, and N. Vittorio. A Measurement of the CMB $\langle EE \rangle$ Spectrum from the 2003 Flight of BOOMERANG. *Astrophys. J.*, 647:813–822, August 2006.

[53] S. Naess, M. Hasselfield, J. McMahon, M. D. Niemack, G. E. Addison, P. A. R. Ade, R. Allison, M. Amiri, A. Baker, N. Battaglia, J. A. Beall, F. de Bernardis, J. Bond, J. Britton, E. Calabrese, H.-m. Cho, K. Coughlin, D. Crichton, S. Das, R. Datta, M. J. Devlin, S. R. Dicker, J. Dunkley, R. Dünner, J. W. Fowler, A. E. Fox, P. Gallardo, E. Grace, M. Gralla, A. Hajian, M. Halpern, S. Henderson, J. C. Hill, G. C. Hilton, M. Hilton, A. D. Hincks, R. Hlozek, P. Ho, J. Hubmayr, K. M. Huffenberger, J. P. Hughes, L. Infante, K. Irwin, R. Jackson, J. Klein, B. Koopman, A. Kosowsky, D. Li, T. Louis, M. Lungu, M. Madhavacheril, T. A. Marriage, L. Maurin, F. Menanteau, K. Moodley, C. Munson, L. Newburgh, J. Nibarger, M. R. Nolta, L. A. Page, C. Pappas, B. Partridge, F. Rojas, B. Schmitt, N. Sehgal, B. D. Sherwin, J. Sievers, S. Simon, D. N. Spergel, S. T. Staggs, E. R. Switzer, R. Thornton, H. Trac, C. Tucker, A. Van Engelen, J. Ward, and E. J. Wollack. The Atacama Cosmology Telescope: CMB polarization at $200 < \ell < 9000$. *J. Cosmol. Astropart. Phys.*, 10:7, October 2014.

[54] K. A. Olive et al. Review of Particle Physics. *Chin.Phys.*, C38:090001, 2014.

[55] L. Page, G. Hinshaw, E. Komatsu, M. R. Nolta, D. N. Spergel, C. L. Bennett, C. Barnes, R. Bean, O. Doré, J. Dunkley, M. Halpern, R. S. Hill, N. Jarosik, A. Kogut, M. Limon, S. S. Meyer, N. Odegard, H. V. Peiris, G. S. Tucker, L. Verde, J. L. Weiland, E. Wollack, and E. L. Wright. Three-Year Wilkinson Microwave Anisotropy Probe (WMAP) Observations: Polarization Analysis. *Astrophys. J. Suppl.*, 170:335–376, June 2007.

[56] A. A. Penzias and R. W. Wilson. A Measurement of Excess Antenna Temperature at 4080 Mc/s. *Astrophys. J.*, 142:419–421, July 1965.

[57] M. Piat, J. P. Torre, J. M. Lamarre, J. W. Beeman, R. S. Bhatia, B. Leriche, J. P. Crussaire, and F. Langlet. Design and tests of high sensitivity NTD Ge thermometers for the Planck-High Frequency Instrument. *Low Temperature Detectors*, 605:79–82, February 2002.

[58] *Planck* Collaboration. *Planck* 2013 results. XVI. Cosmological parameters. *Astr. & Astroph.*, 571:A16, November 2014.

[59] *Planck* Collaboration. *Planck* intermediate results. XVII. Emission of dust in the diffuse interstellar medium from the far-infrared to microwave frequencies. *Astr. & Astroph.*, 566:A55, June 2014.

[60] *Planck* Collaboration. *Planck* intermediate results. XXII. Frequency dependence of thermal emission from Galactic dust in intensity and polarization. *ArXiv e-prints*, May 2014.

[61] *Planck* Collaboration. *Planck* intermediate results. XXX. The angular power spectrum of polarized dust emission at intermediate and high Galactic latitudes. *Astr. & Astroph.*, September 2014.

[62] *Planck* Collaboration. *Planck* 2015 results. XIII. Cosmological parameters. *ArXiv e-prints*, February 2015.

[63] *Planck* Collaboration. *Planck* 2015 results. XV. Gravitational lensing. *ArXiv e-prints*, February 2015.

[64] *Planck* Collaboration. *Planck* 2015 results. XVII. Constraints on primordial non-Gaussianity. *ArXiv e-prints*, February 2015.

[65] *Planck* Collaboration. *Planck* 2015 results. XX. Constraints on inflation. *ArXiv e-prints*, February 2015.

[66] Polarbear Collaboration, P. A. R. Ade, Y. Akiba, A. E. Anthony, K. Arnold, M. Atlas, D. Barron, D. Boettger, J. Borrill, S. Chapman, Y. Chinone, M. Dobbs, T. Elleflot, J. Errard, G. Fabbian, C. Feng, D. Flanigan, A. Gilbert, W. Grainger, N. W. Halverson, M. Hasegawa, K. Hattori, M. Hazumi, W. L.

Holzapfel, Y. Hori, J. Howard, P. Hyland, Y. Inoue, G. C. Jaehnig, A. H. Jaffe, B. Keating, Z. Kermish, R. Keskitalo, T. Kisner, M. Le Jeune, A. T. Lee, E. M. Leitch, E. Linder, M. Lungu, F. Matsuda, T. Matsumura, X. Meng, N. J. Miller, H. Morii, S. Moyerman, M. J. Myers, M. Navaroli, H. Nishino, H. Paar, J. Peloton, D. Poletti, E. Quealy, G. Rebeiz, C. L. Reichardt, P. L. Richards, C. Ross, I. Schanning, D. E. Schenck, B. D. Sherwin, A. Shimizu, C. Shimmin, M. Shimon, P. Siritanasak, G. Smecher, H. Spieler, N. Stebor, B. Steinbach, R. Stompor, A. Suzuki, S. Takakura, T. Tomaru, B. Wilson, A. Yadav, and O. Zahn. A Measurement of the Cosmic Microwave Background B-Mode Polarization Power Spectrum at Sub-Degree Scales with POLARBEAR. *Astrophys. J.*, 794:171, October 2014.

[67] POLARBEAR Collaboration, P. A. R. Ade, Y. Akiba, A. E. Anthony, K. Arnold, D. Barron, D. Boettger, J. Borrill, C. Borys, S. Chapman, Y. Chinone, M. Dobbs, T. Elleflot, J. Errard, G. Fabbian, C. Feng, D. Flanigan, A. Gilbert, W. Grainger, N. W. Halverson, M. Hasegawa, K. Hattori, M. Hazumi, W. L. Holzapfel, Y. Hori, J. Howard, P. Hyland, Y. Inoue, G. C. Jaehnig, A. Jaffe, B. Keating, Z. Kermish, R. Keskitalo, T. Kisner, M. Le Jeune, A. T. Lee, E. Linder, M. Lungu, F. Matsuda, T. Matsumura, X. Meng, N. J. Miller, H. Morii, S. Moyerman, M. J. Myers, M. Navaroli, H. Nishino, H. Paar, J. Peloton, E. Quealy, G. Rebeiz, C. L. Reichardt, P. L. Richards, C. Ross, K. Rotermund, I. Schanning, D. E. Schenck, B. D. Sherwin, A. Shimizu, C. Shimmin, M. Shimon, P. Siritanasak, G. Smecher, H. Spieler, N. Stebor, B. Steinbach, R. Stompor, A. Suzuki, S. Takakura, A. Tikhomirov, T. Tomaru, B. Wilson, A. Yadav, and O. Zahn. Evidence for Gravitational Lensing of the Cosmic Microwave Background Polarization from Cross-Correlation with the Cosmic Infrared Background. *Physical Review Letters*, 112(13):131302, April 2014.

[68] POLARBEAR Collaboration, P. A. R. Ade, Y. Akiba, A. E. Anthony, K. Arnold, D. Barron, D. Boettger, J. Borrill, S. Chapman, Y. Chinone, M. Dobbs, T. Elleflot, J. Errard, G. Fabbian, C. Feng, D. Flanigan, A. Gilbert, W. Grainger, N. W. Halverson, M. Hasegawa, K. Hattori, M. Hazumi, W. L. Holzapfel, Y. Hori, J. Howard, P. Hyland, Y. Inoue, G. C. Jaehnig, A. Jaffe, B. Keating, Z. Kermish, R. Keskitalo,

T. Kisner, M. Le Jeune, A. T. Lee, E. Linder, M. Lungu, F. Matsuda, T. Matsumura, X. Meng, N. J. Miller, H. Morii, S. Moyerman, M. J. Myers, M. Navaroli, H. Nishino, H. Paar, J. Peloton, E. Quealy, G. Rebeiz, C. L. Reichardt, P. L. Richards, C. Ross, I. Schanning, D. E. Schenck, B. Sherwin, A. Shimizu, C. Shimmin, M. Shimon, P. Siritanasak, G. Smecher, H. Spieler, N. Stebor, B. Steinbach, R. Stompor, A. Suzuki, S. Takakura, T. Tomaru, B. Wilson, A. Yadav, and O. Zahn. Measurement of the cosmic microwave background polarization lensing power spectrum with the POLARBEAR experiment. *Physical Review Letters*, 113:021301, Jul 2014.

[69] A. G. Polnarev. Polarization and Anisotropy Induced in the Microwave Background by Cosmological Gravitational Waves. *Sov. Ast.*, 29:607–613, December 1985.

[70] C. Pryke, P. Ade, J. Bock, M. Bowden, M. L. Brown, G. Cahill, P. G. Castro, S. Church, T. Culverhouse, R. Friedman, K. Ganga, W. K. Gear, S. Gupta, J. Hinderks, J. Kovac, A. E. Lange, E. Leitch, S. J. Melhuish, Y. Memari, J. A. Murphy, A. Orlando, R. Schwarz, C. O. Sullivan, L. Piccirillo, N. Rajguru, B. Rusholme, A. N. Taylor, K. L. Thompson, A. H. Turner, E. Y. S. Wu, and M. Zemcov. Second and Third Season QUaD Cosmic Microwave Background Temperature and Polarization Power Spectra. *Astrophys. J.*, 692:1247–1270, February 2009.

[71] QUaD Collaboration, M. L. Brown, P. Ade, J. Bock, M. Bowden, G. Cahill, P. G. Castro, S. Church, T. Culverhouse, R. B. Friedman, K. Ganga, W. K. Gear, S. Gupta, J. Hinderks, J. Kovac, A. E. Lange, E. Leitch, S. J. Melhuish, Y. Memari, J. A. Murphy, A. Orlando, C. O'Sullivan, L. Piccirillo, C. Pryke, N. Rajguru, B. Rusholme, R. Schwarz, A. N. Taylor, K. L. Thompson, A. H. Turner, E. Y. S. Wu, and M. Zemcov. Improved Measurements of the Temperature and Polarization of the Cosmic Microwave Background from QUaD. *Astrophys. J.*, 705:978–999, November 2009.

[72] QUIET Collaboration, D. Araujo, C. Bischoff, A. Brizius, I. Buder, Y. Chinone, K. Cleary, R. N. Dumoulin, A. Kusaka, R. Monsalve, S. K. Næss, L. B. Newburgh, R. Reeves, I. K. Wehus, J. T. L. Zwart, L. Bronfman, R. Bustos, S. E. Church, C. Dickinson, H. K. Eriksen, T. Gaier, J. O. Gundersen, M. Hasegawa, M. Hazumi, K. M. Huffenberger, K. Ishidoshiro, M. E. Jones, P. Kangaslahti, D. J.

Kapner, D. Kubik, C. R. Lawrence, M. Limon, J. J. McMahon, A. D. Miller, M. Nagai, H. Nguyen, G. Nixon, T. J. Pearson, L. Piccirillo, S. J. E. Radford, A. C. S. Readhead, J. L. Richards, D. Samtleben, M. Seiffert, M. C. Shepherd, K. M. Smith, S. T. Staggs, O. Tajima, K. L. Thompson, K. Vanderlinde, and R. Williamson. Second Season QUIET Observations: Measurements of the Cosmic Microwave Background Polarization Power Spectrum at 95 GHz. *Astrophys. J.*, 760:145, December 2012.

[73] Quiet Collaboration, C. Bischoff, A. Brizius, I. Buder, Y. Chinone, K. Cleary, R. N. Dumoulin, A. Kusaka, R. Monsalve, S. K. Næss, L. B. Newburgh, R. Reeves, K. M. Smith, I. K. Wehus, J. A. Zuntz, J. T. L. Zwart, L. Bronfman, R. Bustos, S. E. Church, C. Dickinson, H. K. Eriksen, P. G. Ferreira, T. Gaier, J. O. Gundersen, M. Hasegawa, M. Hazumi, K. M. Huffenberger, M. E. Jones, P. Kangaslahti, D. J. Kapner, C. R. Lawrence, M. Limon, J. May, J. J. McMahon, A. D. Miller, H. Nguyen, G. W. Nixon, T. J. Pearson, L. Piccirillo, S. J. E. Radford, A. C. S. Readhead, J. L. Richards, D. Samtleben, M. Seiffert, M. C. Shepherd, S. T. Staggs, O. Tajima, K. L. Thompson, K. Vanderlinde, R. Williamson, and B. Winstein. First Season QUIET Observations: Measurements of Cosmic Microwave Background Polarization Power Spectra at 43 GHz in the Multipole Range $25 \leq \ell \leq 475$. *Astrophys. J.*, 741:111, November 2011.

[74] A. S. Rahlin, P. A. R. Ade, M. Amiri, S. J. Benton, J. J. Bock, J. R. Bond, S. A. Bryan, H. C. Chiang, C. R. Contaldi, B. P. Crill, O. Doré, M. Farhang, J. P. Filippini, L. M. Fissel, A. A. Fraisse, A. E. Gambrel, N. N. Gandilo, S. Golwala, J. E. Gudmundsson, M. Halpern, M. F. Hasselfield, G. Hilton, W. A. Holmes, V. V. Hristov, K. D. Irwin, W. C. Jones, Z. D. Kermish, C. L. Kuo, C. J. MacTavish, P. V. Mason, K. Megerian, L. Moncelsi, T. A. Morford, J. M. Nagy, C. B. Netterfield, R. O'Brient, C. Reintsema, J. E. Ruhl, M. C. Runyan, J. A. Shariff, J. D. Soler, A. Trangsrud, C. Tucker, R. S. Tucker, A. D. Turner, A. C. Weber, D. V. Wiebe, and E. Y. Young. Pre-flight integration and characterization of the Spider balloon-borne telescope. In *Society of Photo-Optical Instrumentation Engineers (SPIE) Conference Series*, volume 9153 of *Society of Photo-Optical Instrumentation Engineers (SPIE) Conference Series*, page 13, July 2014.

[75] A. C. S. Readhead, S. T. Myers, T. J. Pearson, J. L. Sievers, B. S. Mason, C. R. Contaldi, J. R. Bond, R. Bustos, P. Altamirano, C. Achermann, L. Bronfman, J. E. Carlstrom, J. K. Cartwright, S. Casassus, C. Dickinson, W. L. Holzapfel, J. M. Kovac, E. M. Leitch, J. May, S. Padin, D. Pogosyan, M. Pospieszalski, C. Pryke, R. Reeves, M. C. Shepherd, and S. Torres. Polarization Observations with the Cosmic Background Imager. *Science*, 306:836–844, October 2004.

[76] M. J. Rees. Polarization and Spectrum of the Primeval Radiation in an Anisotropic Universe. *Astrophys. J. Lett.*, 153:L1, July 1968.

[77] G. Rocha, R. Trotta, C. J. A. P. Martins, A. Melchiorri, P. P. Avelino, R. Bean, and P. T. P. Viana. Measuring $\alpha$ in the early Universe: cosmic microwave background polarization, re-ionization and the Fisher matrix analysis. *Mon. Not. Roy. Astron. Soc.*, 352:20–38, July 2004.

[78] U. Seljak. Measuring Polarization in the Cosmic Microwave Background. *Astrophys. J.*, 482:6, June 1997.

[79] U. Seljak and M. Zaldarriaga. Signature of Gravity Waves in the Polarization of the Microwave Background. *Physical Review Letters*, 78:2054–2057, March 1997.

[80] C. D. Sheehy. *Progress toward a detection of inflationary B-modes with the* BICEP2 *and Keck Array polarimeters.* Ph.D. thesis, The University of Chicago, 2013.

[81] J. L. Sievers, C. Achermann, J. R. Bond, L. Bronfman, R. Bustos, C. R. Contaldi, C. Dickinson, P. G. Ferreira, M. E. Jones, A. M. Lewis, B. S. Mason, J. May, S. T. Myers, N. Oyarce, S. Padin, T. J. Pearson, M. Pospieszalski, A. C. S. Readhead, R. Reeves, A. C. Taylor, and S. Torres. Implications of the Cosmic Background Imager Polarization Data. *Astrophys. J.*, 660:976–987, May 2007.

[82] D. N. Spergel and M. Zaldarriaga. Cosmic Microwave Background Polarization as a Direct Test of Inflation. *Physical Review Letters*, 79:2180–2183, September 1997.

[83] A. A. Stark. Millimeter and submillimeter observations from the south pole. *AIP Conference Proceedings*, 616(1):83–91, 2002.

[84] K. Story, E. Leitch, P. Ade, K. A. Aird, J. E. Austermann, J. A. Beall, D. Becker, A. N. Bender, B. A. Benson, L. E. Bleem, J. Britton, J. E. Carlstrom, C. L. Chang, H. C. Chiang, H.-M. Cho, T. M. Crawford, A. T. Crites, A. Datesman, T. de Haan, M. A. Dobbs, W. Everett, A. Ewall-Wice, E. M. George, N. W. Halverson, N. Harrington, J. W. Henning, G. C. Hilton, W. L. Holzapfel, S. Hoover, N. Huang, J. Hubmayr, K. D. Irwin, M. Karfunkle, R. Keisler, J. Kennedy, A. T. Lee, D. Li, M. Lueker, D. P. Marrone, J. J. McMahon, J. Mehl, S. S. Meyer, J. Montgomery, T. E. Montroy, J. Nagy, T. Natoli, J. P. Nibarger, M. D. Niemack, V. Novosad, S. Padin, C. Pryke, C. L. Reichardt, J. E. Ruhl, B. R. Saliwanchik, J. T. Sayre, K. K. Schaffer, E. Shirokoff, G. Smecher, B. Stalder, C. Tucker, K. Vanderlinde, J. D. Vieira, G. Wang, R. Williamson, V. Yefremenko, K. W. Yoon, and E. Young. South Pole Telescope software systems: control, monitoring, and data acquisition. In *Society of Photo-Optical Instrumentation Engineers (SPIE) Conference Series*, volume 8451 of *Society of Photo-Optical Instrumentation Engineers (SPIE) Conference Series*, page 0, September 2012.

[85] Y. D. Takahashi, P. A. R. Ade, D. Barkats, J. O. Battle, E. M. Bierman, J. J. Bock, H. C. Chiang, C. D. Dowell, L. Duband, E. F. Hivon, W. L. Holzapfel, V. V. Hristov, W. C. Jones, B. G. Keating, J. M. Kovac, C. L. Kuo, A. E. Lange, E. M. Leitch, P. V. Mason, T. Matsumura, H. T. Nguyen, N. Ponthieu, C. Pryke, S. Richter, G. Rocha, and K. W. Yoon. Characterization of the BICEP Telescope for High-precision Cosmic Microwave Background Polarimetry. *Astrophys. J.*, 711:1141–1156, March 2010.

[86] M. Tegmark and A. de Oliveira-Costa. How to measure CMB polarization power spectra without losing information. *Phys. Rev. D*, 64:063001, Aug 2001.

[87] J. E. Tolan. *Testing inflationary cosmology with* BICEP2 *and the Keck Array.* Ph.D. thesis, Stanford University, 2014.

[88] A. R. Trangsrud. *The* SPIDER *CMB polarimeter.* Ph.D. thesis, California Institute of Technology, 2012.

[89] R. S. Tucker. *Characterization of detectors and instrument systematics for the* SPIDER *CMB polarimeter.* Ph.D. thesis, California Institute of Technology, 2014.

[90] A. van Engelen, B. D. Sherwin, N. Sehgal, G. E. Addison, R. Allison, N. Battaglia, F. de Bernardis, E. Calabrese, K. Coughlin, D. Crichton, J. R. Bond, R. Datta, R. Dunner, J. Dunkley, E. Grace, M. Gralla, A. Hajian, M. Hasselfield, S. Henderson, J. C. Hill, M. Hilton, A. D. Hincks, R. Hlozek, K. M. Huffenberger, J. P. Hughes, B. Koopman, A. Kosowsky, T. Louis, M. Lungu, M. Madhavacheril, L. Maurin, J. McMahon, K. Moodley, C. Munson, S. Naess, F. Nati, L. Newburgh, M. D. Niemack, M. Nolta, L. A. Page, B. Partridge, C. Pappas, B. L. Schmitt, J. L. Sievers, S. Simon, D. N. Spergel, S. T. Staggs, E. R. Switzer, J. T. Ward, and E. J. Wollack. The Atacama Cosmology Telescope: Lensing of CMB Temperature and Polarization Derived from Cosmic Infrared Background Cross-Correlation. *ArXiv e-prints*, December 2014.

[91] C. L. Wong. *Beam Characterization and Systematics of the* BICEP2 *and Keck Array Cosmic Microwave Background Polarization Experiments*. Ph.D. thesis, Harvard University, 2014.

[92] J. H. P. Wu, J. Zuntz, M. E. Abroe, P. A. R. Ade, J. Bock, J. Borrill, J. Collins, S. Hanany, A. H. Jaffe, B. R. Johnson, T. Jones, A. T. Lee, T. Matsumura, B. Rabii, T. Renbarger, P. L. Richards, G. F. Smoot, R. Stompor, H. T. Tran, and C. D. Winant. MAXIPOL: Data Analysis and Results. *Astrophys. J.*, 665:55–66, August 2007.

[93] M. Zaldarriaga and U. Seljak. All-sky analysis of polarization in the microwave background. *Phys. Rev. D*, 55:1830–1840, February 1997.

[94] M. Zaldarriaga and U. Seljak. Gravitational lensing effect on cosmic microwave background polarization. *Phys. Rev. D*, 58(2):023003, July 1998.